Technische Universität München
Fakultät TUM School of Life Sciences Weihenstephan
Lehrstuhl Lebensmittelverpackungstechnik

Experimental and theoretical studies on the water vapor permeation in barrier structures

Sandra Kiese, M.Sc.

Vollständiger Abdruck der von der TUM School of Life Sciences Weihenstephan der Technischen Universität München zur Erlangung des akademischen Grades einer

Doktorin der Naturwissenschaften (Dr. rer. nat.)

genehmigten Dissertation.

Vorsitzender:		Prof. Dr.-Ing. Heiko Briesen
Prüfer der Dissertation:	1.	Prof. Dr. Horst-Christian Langowski
	2.	apl. Prof. Dr.-Ing. habil. Petra Först

Die Dissertation wurde am 21.07.2021 bei der Technischen Universität München eingereicht und durch die TUM School of Life Sciences Weihenstephan am 28.10.2021 angenommen.

Acknowledgements - Danksagung

Die vorliegende Arbeit entstand während meiner Tätigkeit als wissenschaftliche Mitarbeiterin am Fraunhofer-Institut für Verfahrenstechnik und Verpackung IVV in Freising. An dieser Stelle möchte ich meinen großen Dank an alle Beteiligten aussprechen, die mich bei der Bearbeitung meiner Dissertation unterstützt haben.

An erster Stelle möchte ich mich bei meinem Doktorvater Prof. Dr. Horst-Christian Langowski bedanken, der mich mit seinem beeindruckenden Wissen und seinen stets hilfreichen Kommentaren unterstützt hat und mir gleichzeitig die nötige Zeit und den Freiraum gegeben hat, meinen eigenen Weg zu finden.

Weiterhin danke ich Frau apl. Prof. Dr.-Ing. habil. Petra Först für die Bereitschaft, Zweitprüferin zu werden und Herrn Prof. Dr.-Ing. Heiko Briesen für die Übernahme des Prüfungsvorsitzes.

Besonders danke ich auch meiner Mentorin Dr. Esra Kücükpinar, die mich auf meinem Weg zur Wissenschaftlerin angeleitet hat. Ich danke Dir für die hervorragende Betreuung und die große Unterstützung bei der Durchführung der gesamten Arbeit. Durch Dich habe ich gelernt, dass Deadlines auch nur Richtlinien sind und was der Unterschied zwischen Sputtern und E-Beam ist.

Bei Dr. Cornelia Stramm und Dr. Klaus Noller möchte ich mich für ihr Vertrauen bedanken, dass sie mir die Möglichkeit gegeben haben, meine Doktorarbeit in ihrer Abteilung Materialentwicklung durchzuführen und mir die dafür benötigte Zeit zur Verfügung gestellt haben. Insbesondere danke ich Dir, Conny, zusätzlich für die Vermittlung in die Abteilung Verfahrensentwicklung pflanzliche Rohstoffe, die es mir ermöglicht, weiterhin am IVV zu bleiben.

Meinem Bürokollegen Dr. Oliver Miesbauer danke ich für die theoretische Validierung meiner experimentellen Ergebnisse für Mehrschichtstrukturen, ohne die meine Dissertation nicht möglich gewesen wäre. Vielen Dank, dass Du jederzeit

für produktive Diskussionen zur Verfügung gestanden und bestimmt über hundert Mal meine "letzte" Frage beantwortet hast.

Für die sehr kollegiale und freundschaftliche Atmosphäre sowie die informativen und anregenden Diskussionen möchte ich mich bei allen Kolleginnen und Kollegen der Abteilung Materialentwicklung bedanken. Insbesondere danke ich Norbert Rodler und seinem Techniker-Team für die Durchführung der Beschichtungen im Technikum. Ebenso möchte ich mich bei Zuzana Scheuerer, Marius Jesdinszki und der gesamten Prüfgruppe für die Durchführung und Unterstützung bei allen erforderlichen Messungen bedanken.

Ich danke auch Johann Ewender und meinem Studenten Tobias Schmidt, ohne deren technische Unterstützung die notwendigen Modifikationen an der UPA nicht möglich gewesen wären. Ich möchte mich auch bei allen Studenten bedanken, die mir einen Teil der Projektarbeit abgenommen haben und mir so die Zeit gaben, die ich für die Fertigstellung meiner Dissertation brauchte.

Außerdem möchte ich Christian Reischl und seinem gesamten Team danken, die mir bei allen IT-Problemen immer kompetent weitergeholfen haben, auch wenn die Lösung meist schwieriger war, als den PC neu zu starten.

Weiterhin danke ich Dr. Thomas Herfellner für sein Vertrauen, seine Ehrlichkeit und die nötige Zeit meine Dissertation neben meiner Tätigkeit in der Abteilung Verfahrensentwicklung pflanzliche Rohstoffe fertigzustellen. Die Einarbeitung in neue Themengebiete und Aufgaben unter Deiner Anleitung hat wesentlich zu meiner persönlichen und beruflichen Weiterentwicklung beigetragen.

Vielen Dank auch an alle meine Kolleginnen und Kollegen aus der Abteilung Verfahrensentwicklung pflanzliche Rohstoffe für die herzliche Aufnahme in euer Team. Vor allem danke ich meinen Mädels, Melanie Platzer und Veronika Wildgruber, für ihre Freundschaft und die psychologische Intensivbetreuung im letzten Drittel meiner Dissertation.

Nicht zuletzt danke ich von Herzen meinen Eltern und meiner Familie, die immer an meine Fähigkeiten geglaubt und mich in jeder Situation bedingungslos unterstützt haben.

Abstract

Sensitive food and technical products are often encapsulated with multilayer barrier films made of alternating inorganic barrier and polymer layers. Within this thesis, an ultra-permeation accumulation device was adapted to measure water vapor permeation as a function of time. A combination with theoretical quasi-stationary approximations for alternating structures enabled the reduction of measurement times and the prediction of permeation values and lag times for different climate conditions.

Kurzfassung

Empfindliche Lebensmittel und technische Produkte werden häufig mit Barrierefolien aus alternierenden anorganischen und polymeren Schichten verkapselt. Im Rahmen dieser Dissertation wurde ein Permeationsmessgerät zur zeitabhängigen Bestimmung der Wasserdampfpermeation angepasst. Eine Kombination mit theoretischen Modellen für alternierende Strukturen ermöglichte die Reduzierung der Messzeiten und die Vorhersage von Permeationswerten und Verzögerungszeiten für verschiedene Klimabedingungen.

Contents

List of Figures vii

Abbreviations and Physical Parameters ix

Scientific contributions relevant to this thesis xiii

1 Introduction 1

2 Aim and content of the thesis 5

3 Basic principles and state-of-the-art 9

3.1 Deposition of thin inorganic barrier layers 9

3.2 Deposition of polymeric coatings 13

3.3 Multilayer high-barrier films 14

3.4 Permeation, diffusion and sorption 16

3.4.1 Permeation in polymers 18

3.4.2 Sorption in polymers 18

3.4.3 Permeation in inorganic layers 20

3.4.4 Characteristics of combined inorganic-organic layers 23

3.5 Temperature dependency of permeation processes 25

3.6 Mathematical description of permeation through multilayer barrier films 28

3.7 Methods for water vapor permeation measurement 31

4 Results 35

4.1 A systematic approach for the accurate and rapid measurement of water vapor trans-mission through ultra-high barrier films 36

4.2 Time-dependent water vapor permeation through multilayer barrier films: Empirical versus theoretical results 45

4.3 The influence of temperature on the intrinsic transport properties of water in inorganic and polymeric coatings 54

5 Discussion, conclusion and outlook 65

6 Summary **71**

7 Zusammenfassung **75**

List of Figures

1.1 Barrier requirements of different technical products in comparison to sensitive food products. 2

3.1 Schematic of the basic PVD processes: (a) Vacuum evaporation, (b) and (c) Sputter deposition. 11
3.2 Schematic representation of coating methods: (a) gap coating, (b) slot die coating, (c) roll coating, (d) gravure coating. 13
3.3 Schematic of the coating unit of the pilot plant at the Fraunhofer Institute for Process Engineering and Packaging IVV, Freising. . . 14
3.4 Schematic of the four steps of the permeation process through a plane material seperating two compartments of different partial pressures. 17
3.5 Sorption isotherms according to Henry, Langmuir and the dual mode sorption model. 20
3.6 Schematic of permeation models through thin films: (a) Ideal laminate model, (b) Coverage model, (c) Pore model according to Prins and Hermans, (d) Extension of the pore model according to Beu and Mercea. 21
3.7 Permeation mechanisms as a function of defect size. 22
3.8 Schematic of synergy effect of inorganic SiO_x and hybrid polymer ORM layer. 24
3.9 Schematic of tortous-path-effect in an alternating structure, leading to an elongated permeation path. 24
3.10 Model explanation of defect or matrix dominated permeation. . . 27
3.11 Time-dependent partial pressure distribution within a **BPBPB** structure. 29
3.12 Schematic diagram (cross-sectional view) of the ultra-permeation accumulation (UPA) device. 33

Abbreviations and Physical Parameters

Abbreviations

Adh	adhesive
AFL	aluminum foil laminate
ALD	atomic layer deposition
B	inorganic barrier
B2F	back-to-face
CVD	chemical vapor deposition
F2F	face-to-face
FEM	finite element method
HBF	high barrier film
LCD	liquid crystal display
LED	light emitting diodes
OLED	organic light emitting diodes
OPV	organic photovoltaics
ORM	ORMOCER®, organically modified ceramic
OTFT	organic thin film transistors
P	polymer
PA	polyamide
PCTFE	polychlorotrifluoroethylene
PECVD	plasma enhanced chemical vapor deposition
PEN	polyethylene naphthalate
PET	polyethylene terephthalate
PID	proportional-integral-derivative
POLO	Fraunhofer Polymer Surfaces Alliance POLO®
PVD	physical vapor deposition
PVDC	polyvinylidene chloride
PVOH	polyvinyl alcohol
QSS	quasi-steady-state

RH	relative humidity
SiO$_x$	silicon oxide
UPA	ultra-permeation accumulation
VIP	vacuum insolation panels
WVTR	water vapor transmission rate

Physical Parameters

b	[ ]	vacancy affinity
c	[mol m^{-3}]	concentration
c_H^l	[mol m^{-3}]	vacancy saturation concentration
D	[m^2 s^{-1}]	diffusion coefficient
$D_{\mathbf{B}}$	[m^2 s^{-1}]	diffusion coefficient of the barrier layer
D_{eff}	[m^2 s^{-1}]	effective diffusion coefficient
$D_{\mathbf{P}}$	[m^2 s^{-1}]	diffusion coefficient of the polymeric layer
D_0	[m^2 s^{-1}]	limit value of the diffusion coefficient for $T \to \infty$
E_D	[kJ mol^{-1}]	activation energy of diffusion
E_P	[kJ mol^{-1}]	activation energy of permeation
$E_{P_{\mathbf{B}}}$	[kJ mol^{-1}]	activation energy of permeation of the barrier layer
h	[m]	layer thickness
$h_{\mathbf{B}}$	[m]	layer thickness of the barrier layer
h_i	[m]	thickness of individual layer
$h_{\mathbf{P}}$	[m]	layer thickness of the polymeric layer
ΔH_S	[kJ mol^{-1}]	heat of sorption
$\Delta H_{S_{\mathbf{P}}}$	[kJ mol^{-1}]	heat of sorption of the polymeric layer
ΔH_V	[kJ mol^{-1}]	enthalpy of evaporation
j	[mol m^{-2} s^{-1}]	(molar) flux density
$j(t)$	[mol m^{-2} s^{-1}]	(molar) flux density as a function of t
$j(T)$	[mol m^{-2} s^{-1}]	(molar) flux density as a function of T
N	[ ]	number of layers
$N_{\mathbf{B}}$	[ ]	number of barrier layers
$N_{\mathbf{P}}$	[ ]	number of polymeric layers
$n(t)$	[mol m^{-2}]	amount of permeate within time t
p	[Pa]	partial pressure
p_0	[Pa]	standard pressure

P	$[\mathrm{mol\,m^{-1}\,s^{-1}\,Pa^{-1}}]$	permeability coefficient
$P_{\mathbf{B}}$	$[\mathrm{mol\,m^{-1}\,s^{-1}\,Pa^{-1}}]$	permeability coefficient of the barrier layer
P_{eff}	$[\mathrm{mol\,m^{-1}\,s^{-1}\,Pa^{-1}}]$	effective permeability coefficient
$P_{\mathbf{P}}$	$[\mathrm{mol\,m^{-1}\,s^{-1}\,Pa^{-1}}]$	permeability coefficient of the polymeric layer
P_0	$[\mathrm{mol\,m^{-1}\,s^{-1}\,Pa^{-1}}]$	limit value of the permeability coefficient for $T \to \infty$
$P_{0_{\mathbf{B}}}$	$[\mathrm{mol\,m^{-1}\,s^{-1}\,Pa^{-1}}]$	limit value of $P_{\mathbf{B}}$ for $T \to \infty$
Q	$[\mathrm{mol\,m^{-2}\,s^{-1}\,Pa^{-1}}]$	permeability
$Q_{\mathbf{B}}$	$[\mathrm{mol\,m^{-2}\,s^{-1}\,Pa^{-1}}]$	permeability of barrier layer
Q_i	$[\mathrm{mol\,m^{-2}\,s^{-1}\,Pa^{-1}}]$	permeability of individual layer
$Q_{\mathbf{P}}$	$[\mathrm{mol\,m^{-2}\,s^{-1}\,Pa^{-1}}]$	permeability of polymeric layer
Q_{total}	$[\mathrm{mol\,m^{-2}\,s^{-1}\,Pa^{-1}}]$	total permeability of multilayer
R	$[\mathrm{Pa\,m^3\,mol^{-1}\,K^{-1}}]$	ideal gas constant
S	$[\mathrm{mol\,m^{-3}\,Pa^{-1}}]$	solubility coefficient
$S_{\mathbf{B}}$	$[\mathrm{mol\,m^{-3}\,Pa^{-1}}]$	solubility coefficient of the barrier layer
S_{eff}	$[\mathrm{mol\,m^{-3}\,Pa^{-1}}]$	effective solubility coefficient
$S_{\mathbf{P}}$	$[\mathrm{mol\,m^{-3}\,Pa^{-1}}]$	solubility coefficient of the polymeric layer
S_0	$[\mathrm{mol\,m^{-3}\,Pa^{-1}}]$	limit value of solubility coefficient for $T \to \infty$
$S_{0_{\mathbf{P}}}$	$[\mathrm{mol\,m^{-3}\,Pa^{-1}}]$	limit value of $S_{\mathbf{P}}$ for $T \to \infty$
T	[°C] or [K]	temperature
t	[s]	time
ϑ	[d]	lag time

Scientific contributions relevant to this thesis

Peer reviewed publications with first authorship, which are part of this thesis

- Kiese S., Kücükpinar E., Reinelt M., Miesbauer O., Ewender J., and Langowski H.-C., A systematic approach for the accurate and rapid measurement of water vapor transmission through ultra-high barrier films, *Review of Scientific Instruments* **88**, 025108 (2017)

- Kiese S., Kücükpinar E., Miesbauer O., and Langowski H.-C., Time-dependent water vapor permeation through multilayer barrier films: Empirical versus theoretical results, *Thin Solid Films* **672**, 199-205 (2019)

- Kiese S., Kücükpinar E., Miesbauer O., and Langowski H.-C., The influence of temperature on the intrinsic transport properties of water in inorganic and polymeric coatings, *Thin Solid Films* **717**, 138476 (2021)

Further peer reviewed publications with first authorship

- Kiese S., Kücükpinar E., Reinelt M., Wasserdampfpermeation durch Hochbarrierefolien - Ansätze für eine beschleunigte Messung, *Verpackungsrundschau - Technisch wissenschaftliche Beilage* **6**, 64-65 (2016)

Other peer reviewed publications

- Miesbauer O., Kücükpinar E., Kiese S., Carmi Y., Noller K., and Langowski H.-C., Studies on the barrier performance and adhesion strength of novel barrier films for vacuum insulation panels, *Energy and Buildings* **85**, 597-603 (2014)

Not peer reviewed publications

- Reinelt M., Kiese S., Kücükpinar E., Novel approaches to high-barrier WVTR measurement and data evaluation, *Converting Quarterly*, **4**, 66-70 (2016)

Conference contributions with first authorship

- Kiese S., Miesbauer O., Kücükpinar E., Time Dependent Water Vapor Permeation - Experimental and Theoretical Investigations, *LOPEC 2018*, Munich, 13.-15.03.2018

Other conference contributions

- Miesbauer O., Kiese S., Hellstern S., Sharma K., Sanahuja S., Kücükpinar E., Noller K., Kombination von Barrierelacken mit anorganischen Schichten zur Anwendung in flexiblen Verkapselungsmaterialien für Vakuumisolation-spaneele, *8. Thementage Grenz- und Oberflächentechnik: ThGOT 2012 und 3. Optik-Kolloquium Dünne Schichten in der Optik*, Leipzig, 04.-06.09.2012

- Miesbauer O., Kiese S., Kucukpinar E., Bröskamp S., Noller K., Langowski H.-C., Time dependent permeation of water vapor through multilayer barrier films used for the encapsulation of organic photovoltaic modules, *LOPE-C, 6th International Conference and Exhibition for the Organic and Printed Electronics Industry, Organic and Printed Electronics Association*, Munich, 26.-28.05.2014

- Miesbauer O., Kiese S., Kücükpinar E., Experimental and theoretical studies on the time-dependent permeation through multilayer encapsulation films for flexible organic electronics, *AIMCAL 2018 R2R Europe Conference*, Munich, 05.06.2018

1 Introduction

Sensitive food and technical products are encapsulated to protect them from environmental influences [1–3]. The gas and water vapor barrier properties of these materials must be adapted to the requirements of the respective products in order to protect them from degradation as long as possible. Flexible organic electronic devices are one example of a research effort aiming to replace energy and cost intensive silicon technology by flexible, light weight and cost-effective devices, produced by roll-to-roll processes [4, 5]. They have been the focus of a growing field of research in physics and chemistry for more than 60 years now [6, 7]. For a long time, organic materials could not be used in applications with conventional semiconductors because their stability and performance lagged far behind that of inorganic materials such as silicon [7]. This situation changed in the mid-1980s when Ching Tang and Steven van Slyke at Kodak succeeded in developing a low-voltage, thin-film organic light emitting diodes (OLED) [8]. Their first prototype, while unable to replace existing technologies due to its low power, nevertheless opened the door to organic thin-film technology as the basis for new optoelectronic devices. Since then, organic thin films have been used in an increasing number of applications. The most successful examples are OLED, which are currently already used in color displays, organic thin film transistors (OTFT) or organic photovoltaics (OPV). [9, 10]

Organic materials used in electronic and optoelectronic devices are generally divided into two groups. Small molecules are typically deposited by evaporation methods in low or high vacuum and have a precisely defined molecular weight. Polymers, on the other hand, are, with a few exceptions, processed from the solution and have a molecular weight distribution described by the polydispersity of the materials [7]. Unfortunately, the electrical properties of these materials degrade significantly over time in the presence of water and oxygen in ambient air due to the sensitivity of the organic materials to those substances [11–14]. According to Wong, Salleo and Ciesinski [15, 16], the biggest hurdle in the development of organic electronics is therefore the provision of an encapsulation material and suitable process parameters that ensure both the thermal stability of the substrates and the reduction of the brittleness of the device layers. This

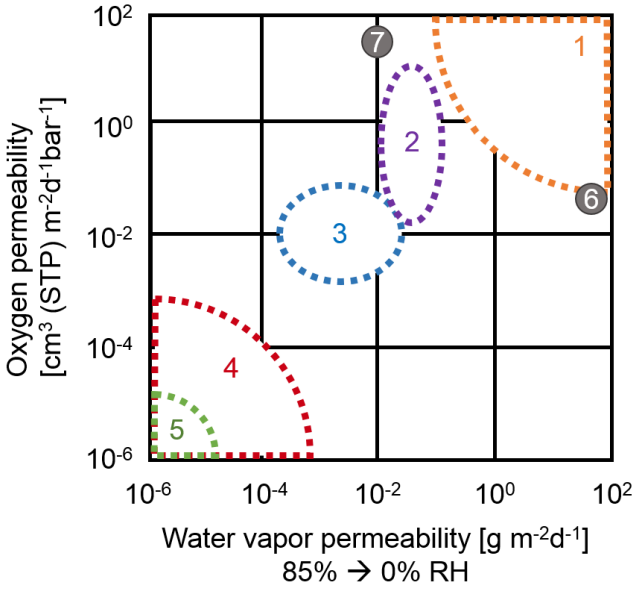

Figure 1.1: Barrier requirements of different technical products in comparison to sensitive food products. 1: Sensitive food; 2: LCD/LED displays and PV modules; 3: vacuum insulation panels (VIP); 4: OPV; 5: OLED displays; 6: barrier property of 100 µm thick PVOH; 7: barrier property of 100 µm thick PCTFE. Reference temperature 23 °C. Reproduced and modified with permission [2].

encapsulation material should protect against environmental influences for as long as possible and at the same time have the mechanical flexibility to enable mass production in a roll-to-roll process and bendability of the products [5, 15–17].

Figure 1.1 shows an overview of the barrier requirements of different technical products compared to sensitive foods. Especially for an application in OPV or even OLED, conventional food packaging lacks several orders of magnitude in barrier performance. For example, films for OPV must not allow more than $1 \times 10^{-3}\,\mathrm{g\,m^{-2}\,d^{-1}}$ of water vapor or $1 \times 10^{-3}\,\mathrm{cm^3}$ (STP) $\mathrm{m^{-2}\,d^{-1}\,bar^{-1}}$ of oxygen to pass through to the sensitive electronic components [18]. For OLED the requirements are even higher. It was generally found that a water vapor transmission rate (WVTR) in the $1 \times 10^{-6}\,\mathrm{g\,m^{-2}\,d^{-1}}$ range is required to produce OLED with sufficient lifetimes above 10 000 h [17, 19–21].

Such low permeabilities cannot be achieved with polymer films or barrier films developed for sensitive food packaging [22]. The single material-based technical polymer films with the lowest permeability for oxygen are made of polyvinyl alcohol (PVOH) and for water vapor of polychlorotrifluoroethylene (PCTFE), which are also shown in Figure 1.1. At present, there are various approaches to reduce the permeability of polymer films by application of inorganic barrier

layers. Methods commonly used to protect sensitive organic layers and electrode materials use encapsulation with high-barrier films consisting of alternating dyads of inorganic barrier (e.g. SiO_x, Si_3N_4 or Al_2O_3) and polymeric intermediate layers deposited on polymeric substrate films [2, 17, 19, 23–30]. By building multilayer structures, an attempt is made to minimize the amount of permeating gases and water vapor and thus maximize the time to the degradation of the devices.

Although great progress has been made in the last decades, especially with regard to barrier improvement and measurement technology, the following scientific gaps still existed at the beginning and during this thesis:

Measurement of barrier properties

- Comparability of measurement results obtained by different measurement methods and under different climate conditions.
- Reduction of the measurement time by increasing the temperature and conversion of measurement results to other climate conditions.
- Reduction of measurement time by modelling and prediction of steady-state values.
- Clarification of the actual permeabilities required to ensure stability of the electronic components, also taking into account the lag times.

Confirmation and evaluation of existing theories

- Experimental validation of previous theoretical approaches for multilayer materials.

Permeation mechanisms

- Clarification of permeation mechanisms of different gases and vapors through multilayer barrier structures.
- Contribution of different defect types to permeation mechanisms of different gases and vapors through multilayer barrier structures.
- Influence of inorganic and polymeric layers on permeability, lag time and temperature behaviour of permeation in multilayer barrier structures.
- Influence of solubility and diffusion coefficients of inorganic and polymeric layers on permeability, lag time and temperature behaviour of permeation in multilayer barrier structures.

2 Aim and content of the thesis

Due to the continuous improvement of encapsulation materials, the demands on measurement technology to be able to detect these low permeabilities within acceptable periods of time also increased. The aim of this thesis was to develop an approach using a combination of optimized measurement technology and a theoretical model that simplifies or even enables the calculation of the stationary water vapor permeation rate (often also called water vapor transmission rate (WVTR)) of multilayer structures at different climate conditions. This method should lead to a reduction of measurement times and allow a prediction of time-permeation curves for multilayer structures as a function of temperature.

For this purpose, the ultrapermeation accumulation (UPA) measurement device developed at Fraunhofer IVV had to be modified first in order to be able to determine water vapor permeation $<5 \times 10^{-5}\,\mathrm{g\,m^{-2}\,d^{-1}}$ through high barrier films as a function of time. By using a large permeation area, the amount of water vapor transported to the detector was to be increased, which should improve the measurement accuracy and lower the measurement limit. In addition, it should be possible to determine the permeation rates over a wide range of temperature and humidity in order to be able to investigate the influence of these parameters on the permeabilities more precisely. Above all, an increase in temperature leads to a shortening of the lag times and thus to a faster achievement of the stationary permeation values. After verification of the applicability of Arrhenius' law, the generated empirical parameters should also allow the extrapolation of the transmission rates to any temperature and humidity. In this way, the influence of ambient conditions on the barrier performance could be estimated. Subsequently, this measurement device should be used to measure water vapor permeation through single and multilayer barrier films under different measurement conditions in order to investigate the influence of layer structures, temperature and relative humidity on transient and steady-state permeation.

With these experimental results, the theoretical approximations on quasi-steady-state (QSS) permeation through multilayer structures previously established by Miesbauer [31, 32] had then to be validated with respect to their applicability to real layer systems and thus material-specific solubility and diffusion parameters

were to be determined for each layer. This should then allow statements to be made about which properties of the individual layers (layer thickness, solubility and diffusion coefficients) dominate the steady-state WVTR and the lag time of the multilayer barrier films. Furthermore, WVTRs and lag times of multilayer structures should be predicted using parameters obtained from sorption measurements, which should significantly reduce the time required for experiments. In order to take advantage of the increased permeation rate through the films at higher temperatures, approximate equations from a combination of QSS and Arrhenius' equations should be developed, which allow to predict the transient water vapor permeation for relevant temperature and humidity conditions.

The aim of this thesis was therefore to fill the following scientific gaps mentioned above:

Measurement of barrier properties

- Comparability of measurement results obtained by different measurement methods and under different climate conditions.
- Reduction of the measurement time by increasing the temperature.
- Conversion of measurement results to other climate conditions.
- Reduction of measurement time by modelling and prediction of steady-state values using theoretical approaches.

Confirmation and evaluation of existing theories

- Experimental validation of previous theoretical approaches for multilayer materials, especially the theoretical approach derived by Miesbauer [32].

Permeation mechanisms

- Clarification of permeation mechanisms of water vapor through multilayer barrier structures, especially the contribution of nano-defects in inorganic layers.
- Influence of inorganic and polymeric layers on permeability, lag time and temperature behaviour of permeation in multilayer barrier structures.
- Influence of solubility and diffusion coefficients of inorganic and polymeric layers on permeability, lag time and temperature behaviour of permeation in multilayer barrier structures.

The results of this work should enable the design of multilayer barrier films according to the lifetime requirements of sensitive components. With the help of the theoretical approximations and the experimentally determined parameters it should be possible to predict the barrier performance of multilayer barrier structures, which allows a significant reduction of the experimental measurement times.

3 Basic principles and state-of-the-art

The following chapter gives a short introduction to existing technologies for the production of high barrier materials and films. Furthermore, the basic principles of permeation, diffusion and sorption mechanisms of gases and vapors in solid polymeric and inorganic layer materials are described, as well as their experimental measurement methods and determination by theoretical approaches.

3.1 Deposition of thin inorganic barrier layers

As described above, thin inorganic layers are applied to substrate films to reduce the permeability of polymers to gases and vapors. In order to deposit those layers onto substrate films different coating technologies can be used. These are generally differentiated according to the thickness of the coating. Coatings of up to 10 µm thickness are usually referred to as thin-film technology, with significantly different properties compared to thicker layers, which can partly be explained by the changed microstructure [33].

In the field of thin-film technology, physical or chemical vapor deposition (PVD or CVD) technologies as well as electrochemical deposition techniques have become established as common processes in recent years [34, 35]. A shared characteristic of almost all vapor based thin-film processes is that the coating material is deposited on an atomic scale, as single atoms, ions, clusters or molecules via their vapor phase [34–36].

In the chemical vapor deposition (CVD) processes, the layer deposition is carried out by chemical reactions of gaseous precursors directly on the substrate surface. This reaction is activated by applying heat or electron collisions in a plasma (plasma enhanced chemical vapor deposition (PECVD)) [35, 37–39]. Recently, the CVD-method of atomic layer deposition (ALD) is gaining more and more importance for the production of nm-thin inorganic layers. In this process, individual atomic layers are deposited on the surfaces by alternating pressure pulses of the precursor gases and vapors on the substrate surface and

the subsequent chemisorption and surface reaction. The self-limiting growth mechanism facilitates the growth of conformal thin films of precise thickness over large areas. Due to the step-by-step formation, the individual atomic layers are created conforming to the surface and even with existing substrate roughness, closed layers without defects can be produced. [35, 40, 41]

In this thesis the inorganic barrier layers were deposited by electron beam evaporation, therefore this and other PVD methods are compared in more detail below. The results of the dissertation can also be transferred to layers that were produced with one of the other PVD or CVD methods.

Physical vapor deposition

This technology offers the possibility to deposit a variety of metallic and ceramic materials in thin form on practically all technically relevant substrate materials. In addition to substrates such as metals, alloys, ceramics and glasses, nowadays also polymeric substrate materials, which require low process temperatures, are coated. The term physical vapor deposition (PVD) processes covers a variety of methods for depositing thin solid films by condensing an evaporated form of the coating material on various surfaces. PVD involves the physical ejection of material in the form of atoms or molecules and the condensation and nucleation of these atoms on a substrate. In reactive deposition processes, the evaporated material chemically reacts with gases introduced into the vapor (e.g. nitrogen to form nitrides) or with another depositing material to create new compounds on the surface. PVD processes are usually high vacuum processes which can be divided into the process variants: thermal evaporation by electron beam, sputtering or pulsed laser beams, reactive evaporation, cathodic arc deposition and ion plating. In addition, there are hybrid processes, e.g. magnetron sputtering and thermal evaporation by electron beam heated crucibles, magnetron sputtering and filtered cathodic arc deposition or thermal evaporation and filtered cathodic arc deposition, that combine the properties of the individual PVD and/or CVD processes. [35, 36, 42]

The basic PVD processes are the thermal evaporation methods by electron beam or sputtering [36] (see Figure 3.1). In principle, these procedures can be described by the following three steps [36]. First, the so-called target material is converted into a **vapor phase** species which is then **transported** to the substrate under thermal scattering or molecular flow conditions (i.e. without collisions between atoms and molecules). Alternatively, if the partial pressure of the metal vapor and/or residual gas species in the vapor state is high enough, some of these

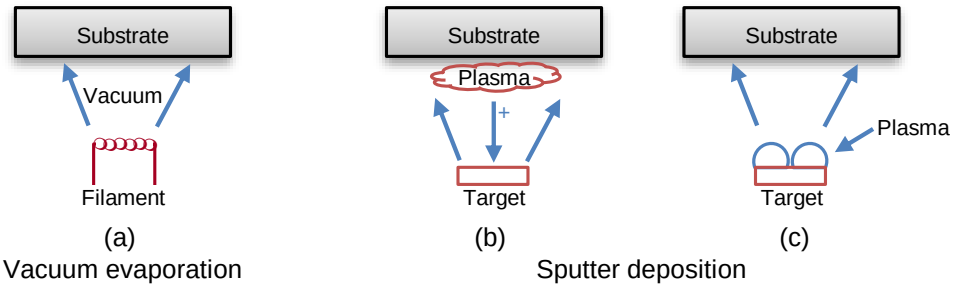

Figure 3.1: Schematic of the basic PVD processes: (a) Vacuum deposition, (b) Sputter deposition by direct-current plasma, filling the area between the source and the substrate, (c) Sputter deposition with a magnetron assisted plasma confined near the sputter target surface via magnetic fields.

species can be ionised (by generating a plasma, predominantly via the impact of electrons), resulting in a large number of collisions in the vapor phase during transport to the substrate. Once the atoms or molecules are deposited, a **growing film** is formed on the substrate. By bombarding this film with ions from the vapor phase, microstructure and composition can be additionally modified [36]. The resulting microstructure is strongly dependent on the deposition conditions, substrate temperature and layer thickness [43–45]. The most frequently observed microstructure seen in scanning electron [46, 47] or atomic force [46, 48–52] microscopic investigations of broken thin film layers is that of columns or grains. It is assumed that these are not completely densely packed and possibly enclose cavities that are also columnar [43–45, 47, 51]. Based on this, Roberts et al. [47] proposed the transport of gas and water vapor in barrier films by three different processes: unhindered transport through macro-defects (>1 nm) in the layer, hindered transport through nano-defects (<1 nm), and hindered transport through a probably existing amorphous matrix (gaps <0.3 nm), whereby the relative contribution of the individual components depends on the size of the permeate atom or molecule as well as the size and number of the defects.

Deposition via thermal evaporation

During vacuum evaporation, sometimes also called vacuum deposition, the material from a thermal evaporation source reaches the substrate with little or no collision with gas molecules in the space between the source and substrate (Figure 3.1(a)) [36]. The vacuum environment also reduces gaseous contamination in the coating system to a low level. Typically, coating takes place in the gas pressure range of 1×10^{-3} to 1×10^{-7} Pa. The thermal evaporation rate can be very high

compared to other evaporation methods, making this method more cost effective than others. [35, 53]

Partial pressures in the vapor phase correspond to the relative vapor pressures of the heated, liquid or solid components of the target material. Thermal evaporation is generally achieved by thermally heated crucibles or boats, or by high energy electron beam (e-beam) exposure heating of the feedstock itself. To reduce the radiant heating of the substrate by the evaporation and to remove the enthalpy of condensation of the layer material, the substrates are mounted at some distance from the evaporation source and are often cooled. [42]

In this thesis the inorganic barrier layer was transparent silicon oxide (SiO_x), which was deposited by Amcor Flexibles Kreuzlingen AG using physical vapor deposition by electron beam evaporation of a target material consisting of a mixture of Si, SiO and SiO_2. This method is in contrast to its main competing technology, the aluminum oxide deposition, where the oxide is reactively formed after aluminum is vaporized and oxygen is injected. [45, 54]

Sputter deposition

In sputter deposition, particles are deposited, which are released from a target by energetic ion bombardment in a vacuum, i.e. by physical sputtering. In general, the distance between source and substrate is short compared to electron beam evaporation. In contrast to evaporation in a high vacuum, sputtering requires an inert process gas such as argon and a high-voltage source to produce a discharge for the geneartion of ions. For reactive sputtering processes, a reactive gas, e.g. oxygen or nitrogen, is required additionally. Sputtering deposition can be performed by bombardment of a solid sputtering target in vacuum with an ion gun or a low-pressure plasma (0.6 Pa), whereby only few or no gas phase collisions happen in the space between target and substrate. Furthermore, sputtering can also be performed at higher plasma pressure (0.7 Pa to 4.0 Pa), where the sputtered or reflected energetic particles are thermalized by gas phase collisions before reaching the substrate surface. The plasma can be located in the area between the source and the substrate (Figure 3.1(b)) or near the sputtering surface due to a magnetron (Figure 3.1(c)). The sputter source can be an element, alloy, mixture or compound, and the material is vaporized with the bulk composition of the target. [37, 42, 55]

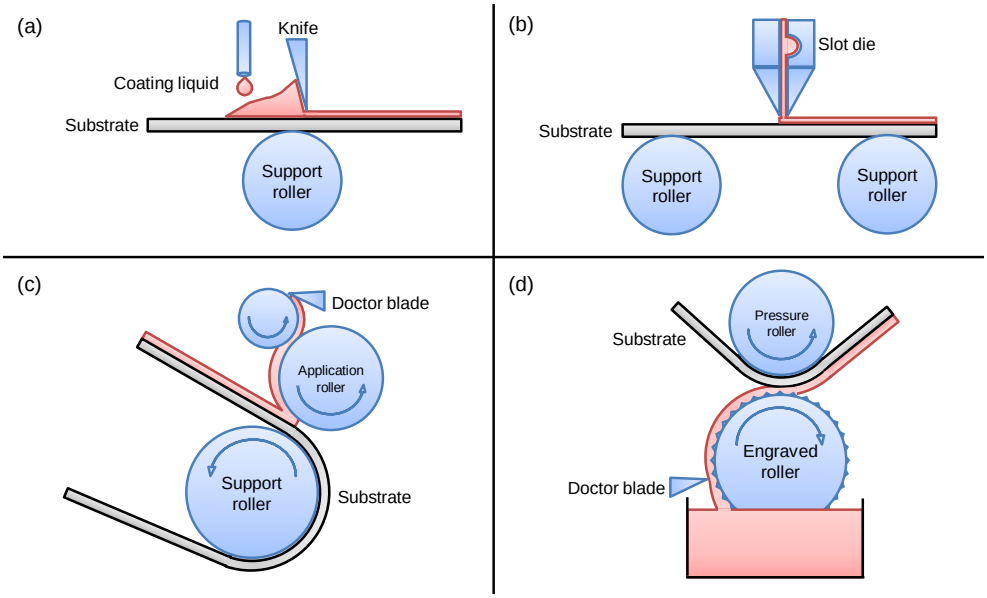

Figure 3.2: Schematic representation of coating methods: (a) gap coating, (b) slot die coating, (c) roll coating, (d) gravure coating.

3.2 Deposition of polymeric coatings

For the deposition of polymeric coatings, often one of the following methods is used: extrusion coating, deposition from solution with thermal, UV or electron beam cross-linking, and deposition from the gas phase (plasma process, PVD or CVD process) [56]. The polymeric coatings in this thesis were applied by deposition from solution with thermal curing, which is why this method will be described in more detail in the following.

The application of wet-chemical coatings on web-shaped materials is commonly done on lacquering machines. In contrast to vacuum evaporation, this process works under atmospheric pressure and the lacquer or adhesive is usually in a liquid state before application. There are several types of applicators, whereby the choice depends on the viscosity, the layer thickness and the solid content of the lacquer/adhesive. Figure 3.2 shows a schematic illustration of different coating methods. [57, 58]

In the **gap coating** process, the coating is first applied to the substrate and then stripped off through a gap between a 'knife' and a back-up roll, as shown in Figure 3.2(a). In the **slot die** coating process, on the other hand, the coating is pressed under pressure through a slot onto the substrate, as shown in Figure 3.2(b). In **roll coating** processes, the coating is transferred from the application roller to the substrate as it passes around the support roller on the bottom side. Figure 3.2(c) shows a 3-roll reverse roll coating process. A variation of this

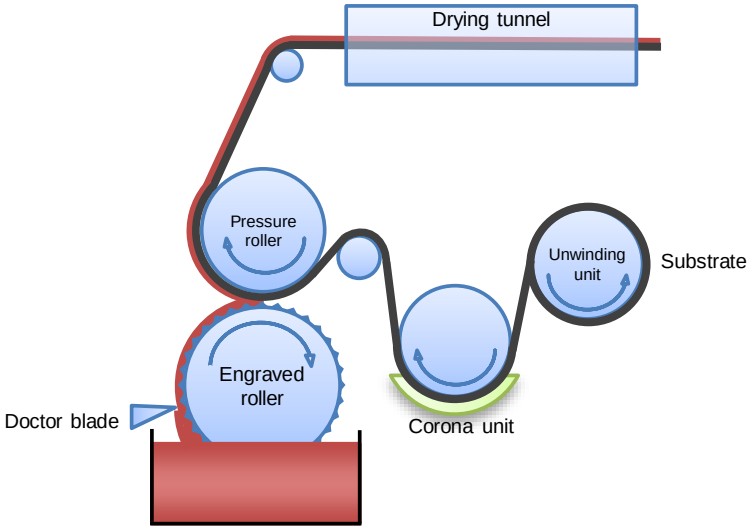

Figure 3.3: Schematic of the coating unit of the pilot plant at the Fraunhofer Institute for Process Engineering and Packaging IVV, Freising.

method is a so-called **gravure** process (Figure 3.2(d)), where the application roller is engraved and takes up a solvent-based coating by dipping into the coating trough. A doctor blade scrapes off the excess coating, which flows back into the trough. The film is guided above the application roller, in the same or opposite (reverse gravure) direction to the running direction of the film. The gap between the application roller and the pressure roller is regulated in such a way that the coating is transferred to the substrate as a coherent film (depending on the cohesion forces) with the aid of the adhesive forces. [58, 59]

In this thesis, the coating and laminating plant of the Fraunhofer Institute for Process Engineering and Packaging IVV, Freising (see Figure 3.3) was used for the application of the lacquer and adhesive layers by a reverse gravure process. In order to increase the surface tension of the substrate film and thus the wetting by the coating or adhesive, corona pretreatments can be performed. After coating, the film passes through a convection heat drying tunnel to evaporate the solvent and dry the coating. Chemical reactions triggered by heat, infrared or ultraviolet radiation lead to cross-linking of the coating. [59]

3.3 Multilayer high-barrier films

As already mentioned in Chapter 1, the barrier properties of polymeric single-layer encapsulation materials are often not sufficient for technical applications. For non-flexible transparent applications, the use of glass encapsulation is the method

of choice. Also for flexible applications there are approaches to use very thin glass, which is also roll-to-roll processable and flexible, but only to a certain degree [5, 17, 60, 61]. Therefore, further flexible encapsulation approaches such as metal foils or inorganic barrier-coated flexible substrate films have been developed. Although metal foils have an excellent barrier effect against water vapor and oxygen and are mechanically very flexible, their use in organic electronics is limited due to their lack of transparency [17, 60, 61].

Accordingly, barrier films based on coated polymer substrates have great potential for use as encapsulation materials due to their flexibility and optical transparency, which can be up to 90 % [61]. To achieve the required barrier effects, alternating layers of inorganic barrier layers and polymeric intermediate layers are often used [2, 17, 19, 23–30]. There are different theories on the mechanism of how the multilayer structures improve the barrier effect. One possible explanation is the filling of the defects in the inorganic layer by the applied polymer layer leading to a reduced permeation within the defects [35, 62, 63]. Furthermore, the polymeric layers have a smoothing effect, which leads to a reduction of defects in the subsequent inorganic layer [62–64]. In addition, the defects in adjacent inorganic layers are separated by the intermediate layers and the diffusion path length increases, especially if very thin intermediate layers are used (tortuous path effect) [32, 65–68].

Graff et al. [64] demonstrated theoretically that multiple barrier layers should not reduce the steady-state permeation rate to the extent that they actually seem to do. Instead, the calculations showed that the lag time (see Chapter 3.4) could be increased to several years. This means that permeation can be significantly delayed by using multilayer structures with alternating layers of different solubility coefficients, which may be sufficient for many applications. These results have also been confirmed several times experimentally for water vapor permeation [64, 69–73].

The following is a brief overview of existing high-barrier film technologies using multilayer deposition on polymeric substrates. One of the first companies to use alternating layers as a barrier structure was Vitex Corp., which offers an encapsulation film for OLEDs under the brand name Barix®. They use pairs of layers consisting of sputtered AlO_x alternating with electron beam evaporized and UV crosslinked acrylate layers, applied on a polyethylene naphthalate (PEN) substrate. Water vapor permeation rate measurements of these films achieved values of $2 \times 10^{-6}\,\mathrm{g\,m^{-2}\,d^{-1}}$ (at 20 °C, 50 % RH) in the calcium corrosion test (see section 3.7). [20, 25, 26, 74–76]

General Electric (GE) developed a graded barrier layer that enables a continuous

transition between the inorganic and organic layer. A water vapor permeation rate value of $5 \times 10^{-6}\,\mathrm{g\,m^{-2}\,d^{-1}}$ is reported here [19, 77].

Tera-Barrier Films (TBF) has patented a barrier film, which combines alternating layers of metal oxide and metal oxynitride or metal nitride layers. This allows to prevent that the molecules penetrate to the active device components. Water vapor permeation rate values of $1 \times 10^{-2}\,\mathrm{g\,m^{-2}\,d^{-1}}$ to $1 \times 10^{-3}\,\mathrm{g\,m^{-2}\,d^{-1}}$ (at 60 °C, 90 % RH) are reached using this layer system. [78]

The Fraunhofer Polymer Surfaces Alliance (POLO®), consisting of seven Fraunhofer Institutes, was able to produce high barrier films by based on the layer structure polymer substrate/inorganic layer/ORMOCER® (ORM)/inorganic layer in a roll-to-roll process suitable for large scale production [79]. Using reactive sputtered barrier layers and the layer structure PET/$ZnSn_xO_y$/ORM/$ZnSn_xO_y$, the lowest WVTR value of $2 \times 10^{-4}\,\mathrm{g\,m^{-2}\,d^{-1}}$ (at 38 °C, 90 % RH, Ca-test) was measured [73]. This thesis also involves the investigation of barrier films that are based on the principle of Fraunhofer POLO®, using alternating inorganic and ORM layers.

3.4 Permeation, diffusion and sorption

The permeation process describes the mass transport of single molecules of a substance through a macroscopically defect-free solid that has at least two surfaces that serve as boundaries to the substance in its environment. The driving force for this is a concentration gradient of the permeating molecules between two surfaces of the solid, whereby it permeates from the surface with the higher concentration to the surface with the lower concentration. [2, 80, 81]

In general, the permeation process in solids is described by Graham's solution-diffusion model from 1866 [82] and can be characterized on the molecular level by four sub-steps, which are schematically shown in Figure 3.4 [1, 83, 84]. Here, the left side of the material is the side with high partial pressure of permeating molecules and the right side is accordingly defined as the side with low partial pressure. First, the **adsorption**, i.e. the deposition of molecules on the surface of the film corresponding to the higher partial pressure, takes place. Physical adsorption by Van-der-Waals forces, chemical adsorption and adsorption by electrostatic forces between the adsorbed molecules and the material lead to an **absorption** of the permeate by the solid [34, 85]. During the **diffusion** step, the molecules are transported through the film due the concentration gradient. Adolf Fick [86] was the first who described the diffusion quantitatively with the

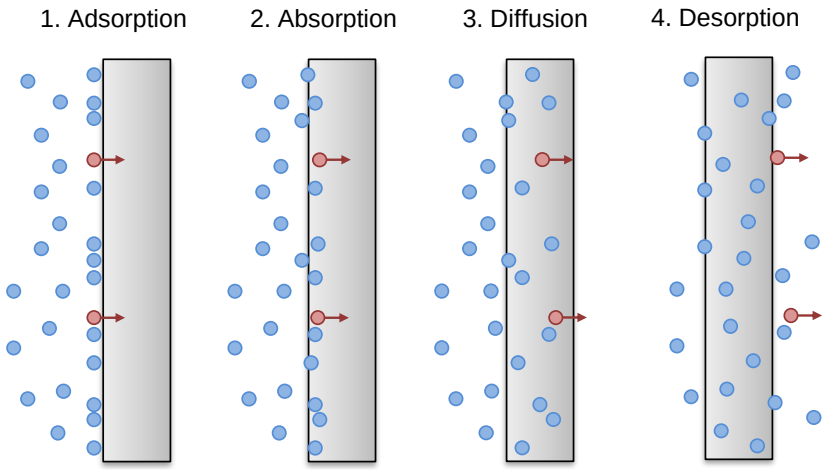

Figure 3.4: Schematic of the four steps of the permeation process through a plane material seperating two compartments of different partial pressures.

diffusion coefficient D and the locally varying concentration c of the permeating substance. This resulted in Fick's First Law for the (molar) flux density j of a permeating substance [85, 87–89], which relates j of the permeating substance with D and the concentration c of the diffusing substance, shown here in its one-dimensional form,

$$j = -D\frac{\partial c}{\partial x}. \tag{3.1}$$

The time dependence of c is given by Fick's Second Law, which is also represented in its one-dimensional form [85, 88, 89],

$$\frac{\partial c}{\partial t} = D\frac{\partial^2 c}{\partial x^2}. \tag{3.2}$$

Finally, the gas molecules emerge from the solid on the opposite side and desorb into the surrounding atmosphere. This process (**desorption**) is the counterpart to the adsorption step [90].

When the permeation process has reached its stationary state, i.e.

$$\frac{\partial c}{\partial t} = 0, \tag{3.3}$$

the concentration c of the diffusing substance remains constant over time at any point in the material. Consequently, the concentration of the permeating substance shows a linear spatial distribution.

The amount $n\,(t)$ of permeating molecules that has permeated through a film sample of unit area within a sufficiently long time period t has a linear asymptote,

which is given by a part of the solution of Fick's Second Law,

$$n\,(t) \approx j_{\text{steady}} \times (t - \vartheta)\,. \tag{3.4}$$

This defines the lag time ϑ, but is only valid if the partial pressure on the dry side is sufficiently small so that it has no influence on the partial pressure gradient. [31, 89]

The permeation of a gas through a homogeneous solid material is defined by the general permeation coefficient P of the respective diffusing substance, which is given by the product of the diffusion coefficient D and the solubility coefficient S [83, 90–92],

$$P = D \cdot S. \tag{3.5}$$

These coefficients can in many cases be assumed to be constant over time, position and concentration and are therefore considered as material-specific parameters of the respective layer in combination with the substance under study [85, 90]. In the following sections, the processes of diffusion, sorption and permeation and related models from the literature for the respective layer materials are described in detail.

3.4.1 Permeation in polymers

The permeation mechanisms through polymeric materials have long been described in the literature [80]. Due to the relatively low density of their molecular structure, basically all polymeric materials are permeable to gases, vapors or liquids. Most of the permeation occurs through amorphous areas and less through crystalline ones, as these are much more densely arranged and therefore have a better barrier effect. Nevertheless, it is assumed that the permeation mechanism of polymers is homogeneous, since the phases represent only small statistically distributed volumes compared to the size of the whole sample and do not have to be considered as location-dependent. [69, 84, 93]

3.4.2 Sorption in polymers

The so-called 'free volume' models for glass-like polymers assume that the total free volume, which is created by microcavities within a polymer structure, is composed of a part that is created by molecular motions of the polymer chains and a part that consists of defect structures like voids, microcracks and other

discontinuous variations in the morphology. Due to the limited number of such local defect structures, a non-linear relationship between concentration and partial pressure is obtained. In contrast, the molecular models for temperatures above the glass transition temperature only assume that fluctuations in the macromolecule chains in the amorphous areas create microcavities where the molecules can be dissolved. In this case the concentration of the dissolved substance is linearly dependent on the partial pressure. The solubility in highly crystalline polymers is considerably lower than that of amorphous polymers due to the low amorphous volume fraction and the associated small number of microcavities. [90]

At sufficiently low partial pressures of penetrating gas molecules and temperatures T above the glass transition point of polymers, the amount of absorbed gas per volume of film can be described by Henry's law [3, 85, 90, 94],

$$c = S \times p \tag{3.6}$$

or

$$S = \text{const.} \tag{3.7}$$

Accordingly, the concentration c of the gas sorbed in the solid is proportional to its partial pressure p prevailing in the environment and the solubility coefficient S is a measure of the solubility of molecules in the solid, which depends on the properties of both the solid and the permeating substance. [90]

Therefore, further models, like the dual sorption or the Langmuir isotherm, have been developed, which describe the permeation of condensable gases in glassy polymers. Figure 3.5 shows the schematic of the sorption isotherms, which are briefly described below.

A common model to describe the solution behaviour of polymers below glass transition temperature is the 'dual sorption' model [90, 92, 96]. Here, the dissolved substance is divided into two different groups. One part dissolves according to a mechanism that occurs in the amorphous regions of the polymer also at temperatures above glass transition temperature, following Henry's law. The other part absorbs exothermically in solid pre-existing microcavities, which are only present in limited numbers in the amorphous polymer matrix and only in the glassy state. This limitation in adsorption sites leads to a saturation (Langmuir capacity) of the concentration on the inner surface of the microcavities. In the case of the Langmuir isotherm, these limited sorption capacities with increasing partial pressure lead to a flattening of the increase in concentration. Accordingly, this isotherm results from the sum of the two components Henry's law and the concentration course during adsorption according to Langmuir (Eq.

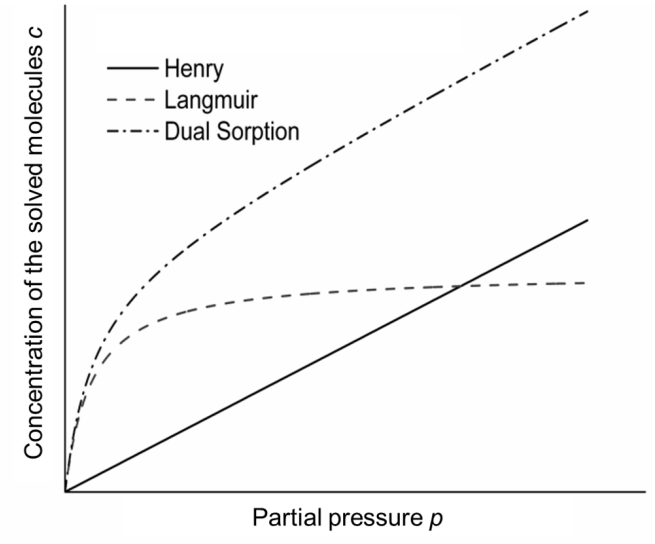

Figure 3.5: Sorption isotherms according to Henry, Langmuir and the dual mode sorption model [95].

3.8):

$$c = S \times p + \frac{c_H^l b}{1 + bp} \times p, \tag{3.8}$$

where c_H^l represents the vacancy saturation constant to be determined experimentally and b is the vacancy affinity. [90]

3.4.3 Permeation in inorganic layers

In order to increase the gas and water vapor barrier properties of polymeric films, they are coated with nanoscale inorganic layers. Depending on the inorganic material and the permeating substance, the permeability values achieved by thin coated layers are often several orders of magnitude higher than those of the corresponding inorganic bulk material. This fact is explained by nano- to macroscopic defects, which are present in the thin inorganic layers and enable the permeation of vapors and gases through the inorganic layer. For the permeation of water vapor, for example, permeation through nanodefects is assumed to be the dominant factor, whereas oxygen is expected to permeate predominantly through macrodefects. [37, 67, 90, 95]

In the literature there are various models for describing the permeation of different vapors and gases through different layer systems, which are shown schematically in Figure 3.6 [97–99].

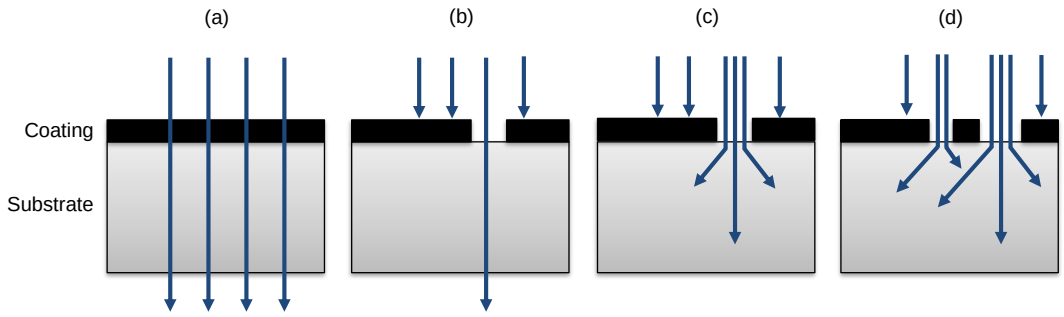

Figure 3.6: Schematic of permeation models through thin films: (a) Ideal laminate model, (b) Coverage model, (c) Pore model according to Prins and Hermans [97], (d) Extension of the pore model according to Beu and Mercea [98].

(a) The **ideal laminate model** assumes that a significant amount of permeate is dissolved in the inorganic material and penetrates through quasi-homogeneous nanodefects, while permeation through macrodefects (larger than 1 nm) is negligible [47, 63, 64, 99–103].

(b) The **coverage model** considers the defects, but shows only the permeation dependence on the degree of coverage of the substrate with the inorganic layer. The coverage model conveys that permeation through the composite occurs only at uncoated areas in a directed way [63, 99, 103].

(c) The **pore model** illustrates the influence of a propagation of the permeation without a preferred direction but in all directions behind a defect in the barrier layer. In comparison to the ideal laminate model, which assumes a homogeneous transport through the whole area of the layer, the pore model treats the mass transfer as mainly located in the areas of the defects. The concentration gradient is largest in the immediate surroundings of the defect, and becomes smaller with increasing distance. [2, 63, 95, 97, 99, 104]

(d) The **extended pore model** by Beu and Mercea [98] additionally takes into account that defects influence each other and can not be considered independently.

Depending on the sizes of the defects, different permeation mechanisms can be assumed [37, 47, 105] (see Figure 3.7). In these models, the transport rate of a gas is determined by the molecular size of the permeating gas and the number

and size of defects [101].

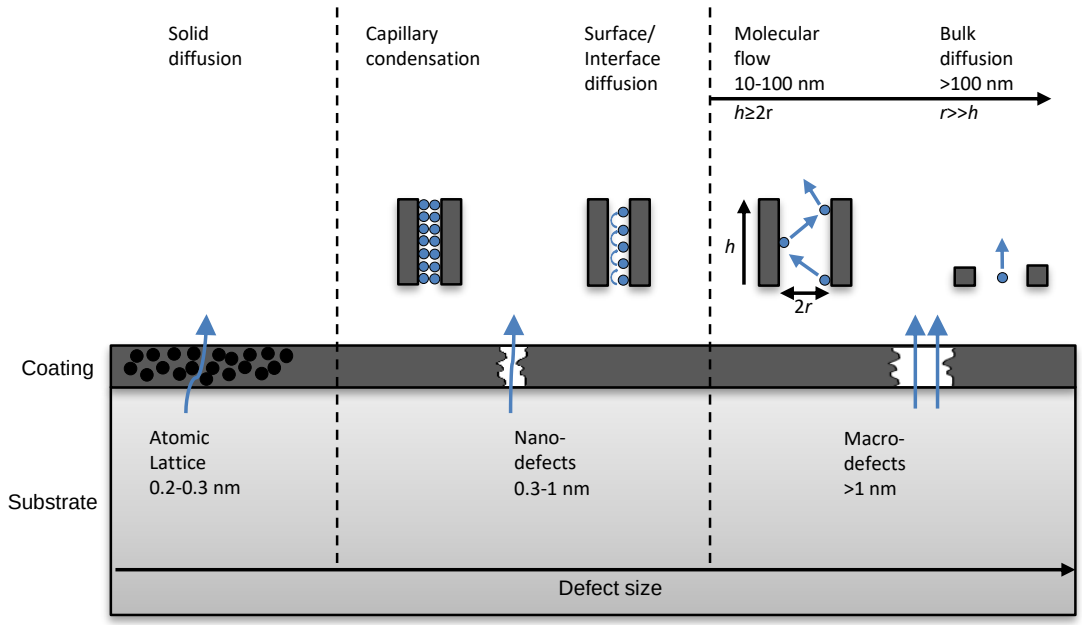

Figure 3.7: Permeation mechanisms as a function of defect size. Figure reproduced from [47, 105].

1. **Solid diffusion:** Permeation of the gas through the atomic lattice of the solid. This process occurs only at higher temperatures and in selected systems and is negligible compared to diffusion through defects. [45, 47, 63, 95, 96, 106]

2. **Capillary condensation:** Here the permeating gas condenses above its normal condensation temperature in defects with a very small diameter. The now liquid substance is then drawn into the gap by the capillary effect and desorbs on the opposite side of the layer. In this case the permeation process no longer takes place in defects filled with gas, but according to the model, the the self-diffusion coefficient of the condensed substance or viscous flow of the liquid have to be taken into account. [2, 95, 105]

3. **Surface/interface diffusion:** This is a transitional process between capillary condensation and molecular flow. A diffusion process takes place along the defect wall perpendicular to the substrate surface [45, 95, 96, 107].

4. **Molecular flow:** This process occurs, when the defects in the barrier layer are so large that the molecules can move freely, but are still smaller than

the mean free path length of the molecules inside the defect [45, 87, 95, 96, 105].

5. **Bulk diffusion:** When the defects reach a macroscopic defect size, the molecules can diffuse freely through the gas-filled space, without interaction with the coating, but with interaction with other gas molecules [35, 45, 87, 95].

It is known that the water vapor permeability in contrast to oxygen permeability of polymer films with inorganic barrier layers is much higher than theoretically calculated by the pore model. The exact reason for this is not yet known, but it is assumed that additional transport mechanisms take place during the permeation of water vapor. Most investigations indicate a capillary condensation of the water vapour. This means that the water vapor condenses in nano-defects, collects there and permeates through the layer in the liquid phase by the capillary effect. Compared to oxygen, which can only penetrate through macrodefects ($\geq$ 1 nm) due to its larger molecule diameter (0.35 nm), water vapor with a gas-kinetic molecule diameter of 0.26 nm can thus additionally permeate through nano-defects (0.35 - 1 nm). [37, 67, 90, 95]

3.4.4 Characteristics of combined inorganic-organic layers

As described above, a common approach today is to create alternating structures of inorganic polymeric layers to achieve the highest possible barrier effect. There are several models for explaining why such structures can achieve a particularly good barrier effect, which are summaried briefly below.

First, the application of a polymeric layer smoothens the surface morphology of the substrate. Due to this so-called planarization effect, inorganic layers with a lower number of macro-defects can be produced subsequently, which increases their barrier effect. [17, 18, 59, 62–64]

In addition, the polymer layers can also increase the barrier effect of an underlying inorganic layer, in some cases of layer combinations even more than theoretically expected. These synergistic effects are explained by the penetration of the liquid polymeric material into the defects of the underlying inorganic layer. After crosslinking of the polymer, the defects are thus filled and permeability is reduced. [15, 35, 62–64, 108, 109]

Chemical interactions between the polymer and the inorganic material, which are assumed to occur mainly for oxide layers in combination with hybrid polymers

(ORM), additionally lead to the formation of covalent bonds and thus to an increased network density in the polymer layer as shown in Figure 3.8. [62, 66]

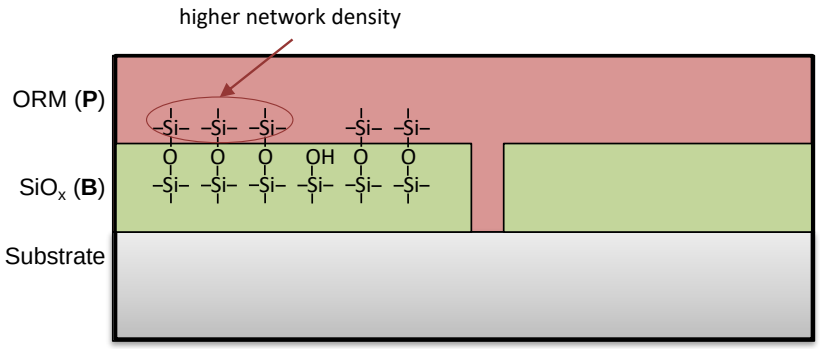

Figure 3.8: Schematic of synergy effect of inorganic SiO_x and hybrid polymer ORM layer. Formation of covalent bonds leads to an increase in network density in the polymer layer, after [62].

Due to the structure of alternating layers, the positions of the defects in the inorganic layers are also decoupled by the intermediate layer. The permeation path within the polymer layer is then extended due to the mutual displacement of the defects (tortous-path-effect, Figure 3.9), which leads to significantly reduced permeability if permeation is dominated by macrodefects, e.g. oxygen. [2, 15, 17, 18, 59, 63, 64, 95, 100, 110]

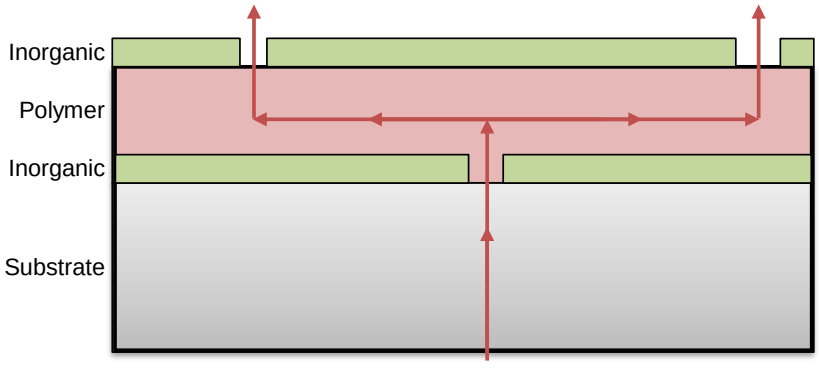

Figure 3.9: Schematic of tortous-path-effect in an alternating structure, leading to an elongated permeation path.

3.5 Temperature dependency of permeation processes

Diffusion generally refers to the transport of particles within a solid or resting fluid, which is caused solely by the concentration gradient. From a microscopic point of view, diffusion in polymeric solids can be described by space exchange processes. Fluctuations of the molecular chains create free spaces in the amorphous matrix of the polymer. The higher the temperature, the greater and more frequent are these density fluctuations. Thus the probability of a change of location or the diffusion rate is rising with increasing temperature. The amount of energy required per mole of gas particles to jump between free spaces of the polymer structure is described by an activation energy E_D. [90, 111]

Therefore, diffusion is a thermally activated process that can be described by an Arrhenius' law [112]:

$$D(T) = D_0 \cdot exp\left(\frac{-E_D}{RT}\right), \tag{3.9}$$

where D_0 represents the limit values for $T \to \infty$ and E_D is the activation energy of the diffusion process.

Dushman and Langmuir were apparently the first to suggest in 1922 that diffusivity in solids should obey this law. In solids, E_D is usually positive, which leads to an increase of D with increasing T. [113, 114]
According to Barrer [115], sorption is as well a thermally activated process and several authors proposed that Van´t Hoff's law applies to the temperature dependency of the solubility coefficient [51, 101, 116, 117]:

$$S(T) = S_0 \cdot exp\left(\frac{-\Delta H_S}{RT}\right), \tag{3.10}$$

where ΔH_S indicates the molar heat of solution, S_0 is the pre-exponential factor representing the limit value for $T \to \infty$, R is the general gas constant and T the temperature. ΔH_S can be both negative and positive in solids, which is why the behavior of S can be different with increasing temperature [114].
Accordingly, also the permeation process, which is the product of diffusion and sorption, can be described by a thermally activated process, following Arrhenius' law [90, 112]:

$$P(T) = P_0 \cdot exp\left(\frac{-E_P}{RT}\right), \tag{3.11}$$

with $E_P = E_D + \Delta H_S$, where E_P is the activation energy of the permeation

process and P_0 represents the limit values for $T \to \infty$.

However, when determining the activation energies by measuring the WVTRs at a given difference of the relative humidity instead at a given partial pressure difference, the additional contribution of the enthalpy of evaporation ΔH_V must be considered, which reflects the dependence of the partial pressure on the temperature. In a sufficiently small temperature range, where ΔH_V can be regarded as a constant, the water vapor pressure p is given by the van't-Hoff equation [85] and consequently, j as a function of the temperature can be expressed as

$$j(T) = \frac{P \cdot p}{h} = \frac{P_0 p_0}{h} \cdot exp\left(\frac{-(E_P + \Delta H_V)}{RT}\right). \tag{3.12}$$

When permeation through a polymeric film coated by an inorganic barrier layer is compared to permeation through the uncoated substrate, there are, according to the literature, different cases how the activation energy can change (Figure 3.10) [51, 100, 118]:

- If permeation through barrier films is dominated by permeation through the defects in the barrier layer and there is no chemical or physical interaction between the permeate and the barrier layer material:
  - matrix dominated, homogeneous layers, with intrinsic barrier properties: E_P corresponds to the activation energy of the permeation through the barrier layer ($E_P = E_{P_\mathbf{B}}$).
  - barrier layer has macro-defects, permeation takes place only within these macro-defects and is therefore determined by E_P of the polymer substrate: E_P approximately corresponds to that of the polymer ($E_P = E_{P_\mathbf{P}}$) (see Fig. 3.10 (b)).

- If there is chemical or physical interaction between the permeating substance and the barrier layers, the activation energy of the multilayer structure is different from that of the polymer: E_P has a value that lies between these two extreme values ($E_{P_\mathbf{P}} < E_P < E_{P_\mathbf{B}}$) (if $E_{P_\mathbf{P}} < E_{P_\mathbf{B}}$).

The determination of the activation energies of substrate and coated film can thus provide an indication of the underlying permeation mechanisms.

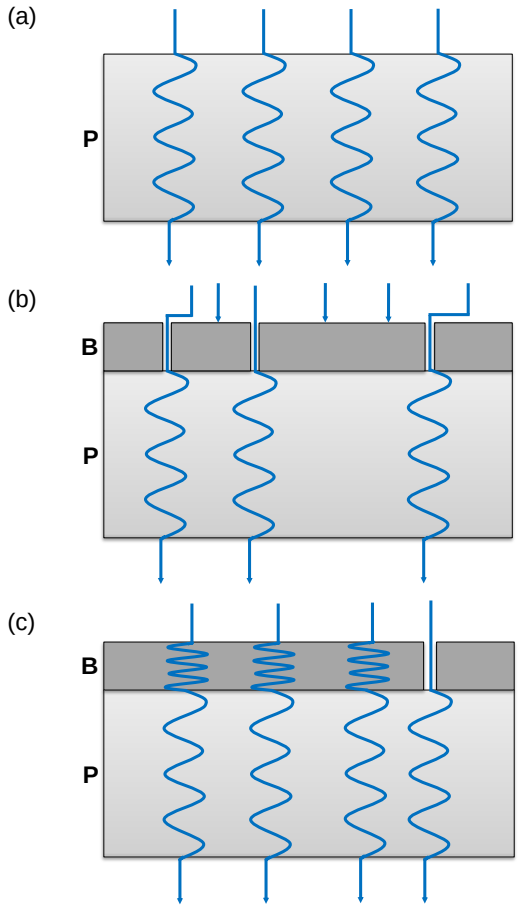

Figure 3.10: Model explanation of defect or matrix dominated permeation following [100], (a) permeation through an uncoated polymer ($E_P = E_{P_\mathbf{P}}$), (b) defect dominated permeation behaviour by a coated polymer ($E_P = E_{P_\mathbf{P}}$) and (c) matrix dominated permeation behavior ($E_{P_\mathbf{P}} < E_P < E_{P_\mathbf{B}}$).

3.6 Mathematical description of permeation through multilayer barrier films

The presented PhD thesis deals with water vapor permeation through multilayer films with alternating inorganic and polymeric layers. Therefore, only selected relevant results on the mathematical description of permeation from the extensive literature are briefly summarized here. A comprehensive overview of the mathematical models that exist for the calculation of non-steady and steady-state permeation through solids can be found in the literature [32, 89].

Water vapor is assumed to permeate mainly through nano-defects of evaporated inorganic layers and permeation through macro-defects is neglected due to their small number in relation to nano-defects [47, 101]. Therefore, in this thesis the inorganic and polymeric layers are assumed to be homogeneous regarding their material properties and nano-defect distribution, and the ideal laminate model is used to calculate the stationary and transient permeation through multilayer barrier films. In stationary case, the multilayer structure is considered in analogy to series connections of electrical resistors of the individual layers [47, 63, 64, 99, 101–103]. Each of the layers is characterized by its individual diffusion D_i and solubility S_i coefficients, and its layer thickness h_i. The steady-state water vapor permeation Q_{total}, can be calculated as

$$\frac{1}{Q_{\text{total}}} = \sum_{i=1}^{n} \frac{1}{Q_i} = \sum_{i=1}^{n} \frac{h_i}{D_i \times S_i}, \tag{3.13}$$

based on the permeability values (Q_i) of the individual layers [2, 89, 90].

Due to the simplified geometry of the multilayer structures in the ideal laminate model, at least the asymptotic behaviour of transient permeation, i.e. the steady-state value, and the lag time can be calculated analytically. However, the exact solutions of the transient diffusion equations are very complex for multilayer structures, which is why numerical solutions are often used. For exact analytical solutions, reference is made here only to the literature [119–127].

In his thesis, Miesbauer [32] compared the permeation processes through multilayer films using numerical and analytical methods using the ideal laminate and the pore model. He investigated the influences of layer thicknesses and sequences of layer structures with at least one triplet of alternating layers as well as different ratios of permeability, diffusion and solubility coefficients on the transient and stationary permeation and the lag time. Since the state-of-the-art high barrier structures with such layer sequences mostly consist of combinations of

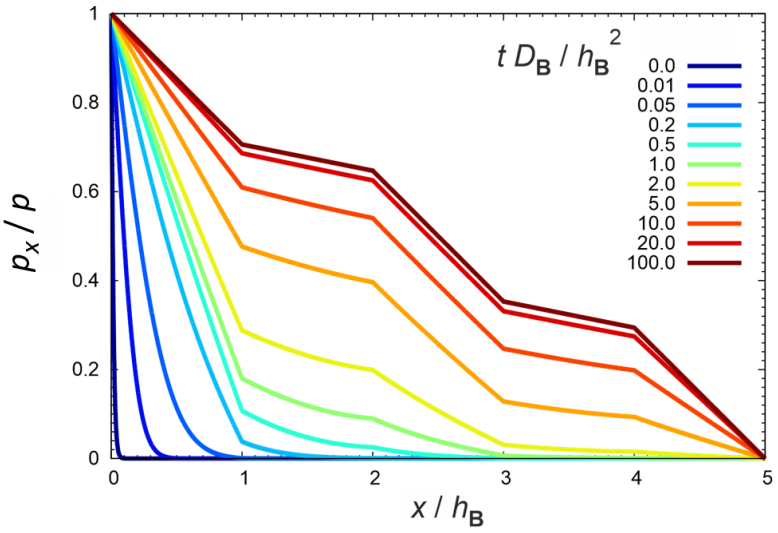

Figure 3.11: Time-dependent partial pressure distribution within a **BPBPB** structure: normalized partial pressure p_x/p as a function of $tD_{\mathbf{B}}/h_{\mathbf{B}}^2$ and $x/h_{\mathbf{B}}$. The **B**-layers meet in the intervals $x/h_{\mathbf{B}} \in [0,1]$, $[2,3]$ and $[4,5]$, the **P**-layers in the intervals $x/h_{\mathbf{B}} \in [1,2]$ and $[3,4]$. Reproduced with permission from [32].

inorganic barrier layers with polymeric interlayers, the layers have been designated as "barrier" **B** and "polymer" **P**. The results of the numerical calculations for transient permeation through multilayer structures consisting of at least one **BPB** triplet revealed an almost linear partial pressure profile within each layer over the duration of measurement and the permeation can be considered quasi-stationary. Figure 3.11 shows this behaviour for a **BPBPB** type structure. [32]

According to Miesbauer [32], the ratios of the permeabilities of the **P** and **B** layers $P_{\mathbf{P}}/P_{\mathbf{B}}$ and the ratios of solubility coefficients of the **P** and **B** layers $S_{\mathbf{P}}/S_{\mathbf{B}}$ have to be sufficiently high to be able to apply the so-called quasi-steady-state (QSS) approximations. As long as these conditions are fulfilled, **P** layers do not necessarily have to be polymers and **B** layers do not necessarily have to be inorganic materials. Thus, the flux density and the concentration in each **P** layer is nearly independent of the position within the layer. At the interfaces between the first **B** and **P** or **P** and the second **B**, the partial pressures are in coincidence. Using Henry's law and Fick's law gives the mass balance for **P**, which after elementary integration gives the time-dependent partial pressure for a **BPB** structure

$$p\,(t) = \frac{p}{2}\left(1 - \exp\left(-\frac{2\,P_{\mathbf{B}}}{h_{\mathbf{B}} h_{\mathbf{P}} S_{\mathbf{P}}} t\right)\right). \tag{3.14}$$

The flux density $j\,(t)$ at the boundary $x = h$ can be calculated by $j\,(t) = (P_{\mathbf{B}}/h_{\mathbf{B}}) \times p\,(t)$ as [32, 128]

$$j\,(t) = \frac{P_{\mathbf{B}} p}{2\,h_{\mathbf{B}}} \left(1 - \exp\left(-\frac{2\,P_{\mathbf{B}}}{h_{\mathbf{B}} h_{\mathbf{P}} S_{\mathbf{P}}} t\right)\right), \tag{3.15}$$

where $P_{\mathbf{B}}$ is the permeability coefficient and $h_{\mathbf{B}}$ the thickness of the **B** layers and where $S_{\mathbf{P}}$ is the solubility coefficient and $h_{\mathbf{P}}$ the thickness of the **P** layer, and p is the boundary partial pressure. A detailed derivation of the QSS approximation equations can be found in [32].

The time-dependent flux density of **BPBPBPB** type structures can be approximated as follows [32, 128]:

$$\begin{aligned} j(t) = \frac{P_{\mathbf{B}} p}{4\,h_{\mathbf{B}}} \Bigg(& 1 - \left(\frac{1}{\sqrt{2}} + 1\right) \exp\left(\left(\sqrt{2} - 2\right) \frac{P_{\mathbf{B}}}{h_{\mathbf{B}} h_{\mathbf{P}} S_{\mathbf{P}}} t\right) \\ & + \exp\left(-2 \frac{P_{\mathbf{B}}}{h_{\mathbf{B}} h_{\mathbf{P}} S_{\mathbf{P}}} t\right) \\ & + \left(\frac{1}{\sqrt{2}} - 1\right) \exp\left(\left(-\sqrt{2} - 2\right) \frac{P_{\mathbf{B}}}{h_{\mathbf{B}} h_{\mathbf{P}} S_{\mathbf{P}}} t\right)\Bigg). \end{aligned} \tag{3.16}$$

The steady-state WVTR values are the asymptotic values of Eqs. 3.15 and 3.16 for large t, i.e.

$$j_{\text{steady}} = \frac{P_{\mathbf{B}} p}{N_{\mathbf{B}} h_{\mathbf{B}}}, \tag{3.17}$$

with $N_{\mathbf{B}}$ being the number of barrier layers.

Using the two parameters $P_{\mathbf{B}}$ and $S_{\mathbf{P}}$, the lag times are calculated as

$$\vartheta = \frac{h_{\mathbf{B}} h_{\mathbf{P}} S_{\mathbf{P}}}{2\,P_{\mathbf{B}}} \tag{3.18}$$

for simple **BPB** type structures and

$$\vartheta = \frac{5\,h_{\mathbf{B}} h_{\mathbf{P}} S_{\mathbf{P}}}{2\,P_{\mathbf{B}}} \tag{3.19}$$

for all **BPBPBPB** type structures with more than one **BPB** triplet and $S_{\mathbf{P}} \gg S_{\mathbf{B}}$, derived from Eqs. 3.15 and 3.16, according to [32].

The QSS approximation equations for other layer systems with **BPB**-type structures (e.g. **BPBPB**) are also available in [32], but are not shown here since they are not relevant for the multilayer structures studied in this thesis.

3.7 Methods for water vapor permeation measurement

Together with the continuous improvement of barrier properties and the lag times of barrier films, the measurement methods must, of course, also be further developed. In the literature, there are various approaches for measuring water vapor permeation through barrier films. Most of these methods have in common a chamber, which is divided into two parts by the film to be measured. On one side gas with a certain relative humidity flows through and on the other side, the dry gas. On this dry side, the amount of permeated water vapor per time and permeation area is detected. Historically, the results of water vapor permeation measurements have often been referred to as water vapor transmission rates (WVTR), although these are actually converted into water vapor flux densities. In most cases, information about the temperature set during the measurement and the difference in relative humidity is also given. The most frequently used measurement techniques are coulometric method, calcium tests, radioactive method and infrared spectroscopy, which differ mainly in the way the permeated water vapor is detected and whether the partial pressure difference remains constant or changes during the measurement.

The most widely used commercial permeation meter is the Aquatran® from MOCON® Inc., which uses an absolute coulometric sensor to measure water vapor permeate and complies with ASTM F3299 [129]. The manufacturer specifies the measuring range from 5×10^{-5} to $5\,\mathrm{g\,m^{-2}\,d^{-1}}$. In this measurement system the sensor is coated with a phosphorus pentoxide layer. This layer absorbs the water molecules, which are then electrolyzed at the electrodes. The resulting electrical current can be measured and converted into a corresponding WVTR. [130, 131]

The first methods for measuring water vapor by means of a calcium test were developed in 2002 by Kumar et al. [132] and achieved an accuracy down to $\sim 1 \times 10^{-2}\,\mathrm{g\,m^{-2}\,d^{-1}}$. This method is divided into an optical and an electrical evaluation procedure. The principle of the optical calcium test is based on the fact that calcium is corroded by water contact and that these optical changes can be determined quantitatively, from which the WVTR can be calculated. The degree of calcium corrosion can also be determined by the change of the electrical conductivity of the calcium, which Paetzold et al. [133] used to characterize water vapor permeation through barrier films with a limit of $1 \times 10^{-6}\,\mathrm{g\,m^{-2}\,d^{-1}}$. Reese et al. [134] compared different calcium methods and developed a method

to measure WVTRs with an accuracy of $<1 \times 10^{-6}\,\mathrm{g\,m^{-2}\,d^{-1}}$ by measuring the change in electrical resistance of calcium layers.

Another commercially available permeation measurement device called HiBarSens® was developed by SEMPA SYSTEMS GmbH in cooperation with the Fraunhofer Institute for Material and Beam Technology (IWS). It uses a laser diode spectroscopic gas sensor which also allows to measure permeation rates of the order of $1 \times 10^{-6}\,\mathrm{g\,m^{-2}\,d^{-1}}$. [135, 136]

A measuring method with radioactive tritium is described by Choi et al [61, 137], Dunkel et al [4] and Bujas et al [138, 139]. A sensor measures the radioactivity of tritium-containing water vapor, which is used as permeating substance and should have permeation values comparable to those of normal water vapor. The WVTR can then be calculated from this. Dunkel et al. [4] estimated the lowest detection limit also in the order of $1 \times 10^{-6}\,\mathrm{g\,m^{-2}\,d^{-1}}$.

Brewer et al. [140, 141] developed a novel system to trace water with a less sensitive detection limit of $1 \times 10^{-4}\,\mathrm{g\,m^{-2}\,d^{-1}}$ using cavity ring down infrared spectroscopy. This method detects water vapor by tuning a pulsed laser source to an absorption line of water. The absorption is calculated from the time required for the laser light to decay in a highly reflective cavity. The conversion of this time period, with and without permeate, allows the calculation of the concentration of the permeate. A validation of the measurement results with established methods, such as the MOCON Aquatran®, confirmed the reliability of the measurement results. Nakano et al. [142] reached a lower detection limit in the $1 \times 10^{-6}\,\mathrm{g\,m^{-2}\,d^{-1}}$ range using a mass spectroscopy detector.

Using a round robin test of the same POLO®-barrier film, Nisato et al. [73] investigated the comparability of different WVTR measurement methods under the same measurement conditions, including optical and electrical calcium tests, Aquatran®, HiBarSens® and Cavity Ring-Down Spectroscopy. However, they also observed differences between the methods, which could be minimised by using common guidelines on standardised measurement conditions.

Notwithstanding the methods presented here for measuring water vapor permeation, an ultra-permeation accumulation (UPA) measurement device was developed at Fraunhofer IVV [68, 143]. Before that, Franz [144] described a method for measuring the permeation of volatile organic compounds through polymer films by means of gas chromatography in 1993, in which a measurement sensitivity in the order of $1 \times 10^{-6}\,\mathrm{g\,m^{-2}\,d^{-1}}$ could be determined. A schematic diagram of the UPA measurement unit developed at Fraunhofer IVV is shown in Figure 3.12 [145]. A previous version of this unit was already described in an earlier publication [143].

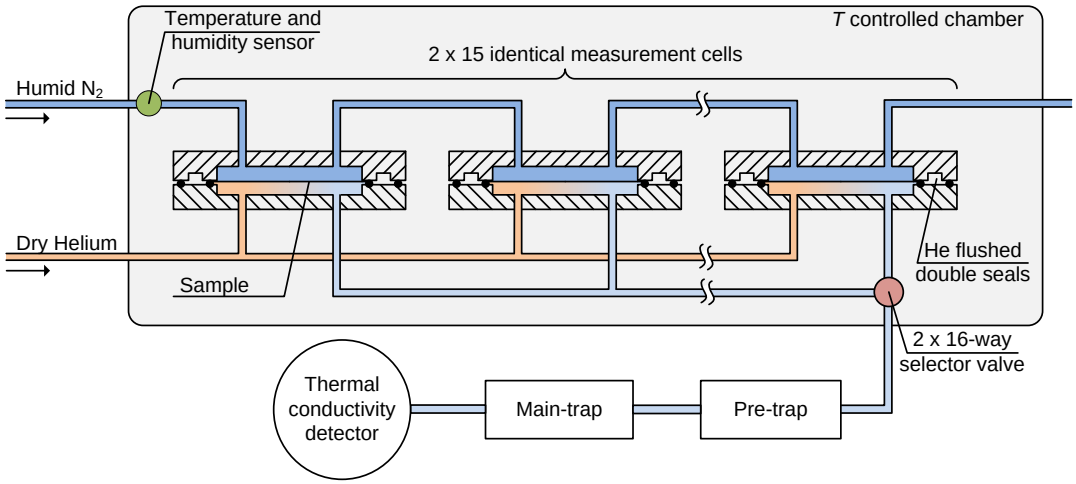

Figure 3.12: Schematic diagram (cross-sectional view) of the UPA device. Reproduced with permission from [145].

The tailor-made unit has some features to offer new possibilities for the transient and steady-state water permeation rate measurement of barrier films at different conditions. The increased sample size of 155 mm diameter enhanced the measurement sensitivity, by increasing the amount of permeating water vapor going to the sensor, and enables the measurement of an average permeation value over a large sample area. By freezing out residual water from the Helium with liquid nitrogen, the measuring accuracy is additionally increased. The relative humidity (RH) and temperature can be controlled between 15 % to 90 % and 23 °C to 80 °C, respectively. A more detailed description of the UPA device can be found in [145] and Chapter 4.1.

What all these methods have in common, however, are the unavoidable long conditioning and measurement times for ultra-high barrier films. Depending on the barrier performance and layer structure of a multilayer barrier material, WVTR measurements can take up to several months to achieve steady-state transmission. In addition, with such a slow increase of the measured time-dependent permeation rate, it is often difficult to tell when the stationary region is reached. Therefore, some WVTR values given in literature were taken in transient region, underestimating the permeation rate of the barrier. Accordingly, it is important to have mathematical models (Chapter 3.6), which represent the actual process of the measurement and allow to calculate the steady-state value of the permeation from measured values of the transient region.

4 Results

The results chapter consists of the following peer-reviewed publications:

- Kiese S., Kücükpinar E., Reinelt M., Miesbauer O., Ewender J., and Langowski H.-C., A systematic approach for the accurate and rapid measurement of water vapor transmission through ultra-high barrier films, *Review of Scientific Instruments* **88**, 025108 (2017).
- Kiese S., Kücükpinar E., Miesbauer O., and Langowski H.-C., Time-dependent water vapor permeation through multilayer barrier films: Empirical versus theoretical results, *Thin Solid Films* **672**, 199-205 (2019).
- Kiese S., Kücükpinar E., Miesbauer O., and Langowski H.-C., The influence of temperature on the intrinsic transport properties of water in inorganic and polymeric coatings, *Thin Solid Films* **717**, 138476 (2021).

4.1 A systematic approach for the accurate and rapid measurement of water vapor transmission through ultra-high barrier films [1]

Summary

The measurement of multilayer films and thus the reliable detection of low permeate amounts can be very challenging and time consuming. Therefore, the ultra-low permeation measurement device was further developed within this dissertation, which achieves a very low detection limit (down to $2 \times 10^{-5}\,\mathrm{g\,m^{-2}\,d^{-1}}$) by accumulation of the permeated water vapor before its transport to the detector. The tailor-made unit has some modifications to offer new possibilities for the transient and steady-state water permeation rate measurement of barrier films at different conditions. The sample films with a diameter of 155 mm are mounted inside 30 identical measurement cells with N_2-flushed double seals to reduce leakage, which are placed in a conditioned chamber. This allows the measurement of 30 different films at the same time. The large sample size allows for improved measurement sensitivity by increasing the area through which water vapor can permeate into the dry chamber. The carrier gas helium transports the permeated water vapor through the traps to a thermal conductivity detector with an individual detection limit of $1 \times 10^{-7}\,\mathrm{g\,m^{-2}\,d^{-1}}$. Due to small leakages, however, the measurement limit for the entire system is somewhat higher. By increasing the measurement temperature (up to 80 °C) and relative humidity (up to 90 %), the amount of permeate can be increased additionally, if necessary, and raised above the detection limit. The measured WVTR values of PCTFE, aluminum foil laminate (AFL) and a high barrier film agreed with those measured using a commercially available Aquatran® device. Additional numerical calculations allow the extrapolation of the time-dependent measurement results at an early stage. Thus, the steady-state value can be predicted and the required experimental time can be reduced.

[1] Kiese S., Kücükpinar E., Reinelt M., Miesbauer O., Ewender J., and Langowski H.-C., A systematic approach for the accurate and rapid measurement of water vapor transmission through ultra-high barrier films, *Review of Scientific Instruments* **88**, 025108 (2017).

Author contributions:

- Sandra Kiese: corresponding author, conceptualization, methodology, planning and execution of experiments and numerical simulations, data evaluation and interpretation, formal analysis, outline, writing original draft, editing, completion
- Esra Kücükpinar: outline, funding acquisition, revision, completion, editing
- Matthias Reinelt: feedback on methodology and manuscript
- Oliver Miesbauer: supervision, development of numerical models
- Johann Ewender: methodology, validation
- Horst-Christian Langowski: supervision, writing - review & editing

REVIEW OF SCIENTIFIC INSTRUMENTS **88**, 025108 (2017)

A systematic approach for the accurate and rapid measurement of water vapor transmission through ultra-high barrier films

Sandra Kiese,[1,2] Esra Kücükpinar,[1] Matthias Reinelt,[1] Oliver Miesbauer,[1,2] Johann Ewender,[1] and Horst-Christian Langowski[1,2]
[1]*Fraunhofer Institute for Process Engineering and Packaging IVV, Giggenhauser St. 35, Freising 85354, Germany*
[2]*Chair of Food Packaging Technology, Technische Universitaet Muenchen, Weihenstephaner Steig 22, Freising 85354, Germany*

(Received 21 October 2016; accepted 12 January 2017; published online 10 February 2017)

Flexible organic electronic devices are often protected from degradation by encapsulation in multilayered films with very high barrier properties against moisture and oxygen. However, metrology must be improved to detect such low quantities of permeants. We therefore developed a modified ultra-low permeation measurement device based on a constant-flow carrier-gas-system to measure both the transient and stationary water vapor permeation through high-performance barrier films. The accumulation of permeated water vapor before its transport to the detector allows the measurement of very low water vapor transmission rates (WVTRs) down to 2×10^{-5} g m^{-2} d^{-1}. The measurement cells are stored in a temperature-controlled chamber, allowing WVTR measurements within the temperature range 23–80 °C. Differences in relative humidity can be controlled within the range 15%–90%. The WVTR values determined using the novel measurement device agree with those measured using a commercially available carrier-gas device from MOCON®. Depending on the structure and quality of the barrier film, it may take a long time for the WVTR to reach a steady-state value. However, by using a combination of the time-dependent measurement and the finite element method, we were able to estimate the steady-state WVTR accurately with significantly shorter measurement times.
[http://dx.doi.org/10.1063/1.4974952]

I. INTRODUCTION

Recent developments in flexible organic electronic devices require equally flexible encapsulation materials with extremely high barrier properties against moisture and oxygen to protect the sensitive active and electrode materials. A current approach for the production of such encapsulation films is to coat polymeric substrate films such as polyethylene terephthalate (PET) or polyethylene naphthalate (PEN) with alternating inorganic and organic layers.[1,2] These materials have a long lag time before water penetration, in addition to a low steady-state water vapor transmission rate (WVTR), to ensure the long-term protection of the sensitive device layers. The WVTR requirements for the encapsulation material of state-of-the-art organic solar cells and organic light emitting diode structures are ~10^{-3} g m^{-2} d^{-1} and ~10^{-6} g m^{-2} d^{-1}, respectively, at 38 °C and 90% relative humidity (RH), to maintain reliable performance for more than 10 000 h.[3]

In order to detect such low quantities of permeants, and to improve the barrier properties of such materials, the metrology must also evolve. Several approaches can be used for the measurement of water vapor permeation through films, including calcium corrosion tests, coulometric electrochemical devices, radioactive methods, mass spectrometry, and infrared light spectroscopy.[4–14]

Two isostatic carrier gas systems are commercially available for the measurement of moisture permeation: the Aquatran® devices from MOCON®, Inc., with a detection limit of ($5 \times 10^{-5} \pm 5 \times 10^{-5}$) g m^{-2} d^{-1} and the HiBarSens® from SEMPA Systems GmbH, with a detection limit of 1×10^{-6} g m^{-2} d^{-1}.[15,16]

The measurement of ultra-high barrier materials is challenging because of the long conditioning and measurement times. Depending on the barrier performance and the layer structure of a multilayer barrier material, WVTR measurements may take several months to reach steady-state transmission rates, and it can be difficult to determine the onset of steady-state conditions. In some cases, the WVTR values recorded before the water vapor permeation process reaches its steady-state are too low, thus producing inaccurate data that overestimate the performance of barrier materials.

We therefore developed an efficient and systematic approach for the measurement of water vapor permeation based on the accumulation of water vapor and an appropriate evaluation method. This approach has the following benefits:

(a) Larger measurement areas may be used (188 cm^2) compared to the commercially available measurement devices.
(b) Precise temperature control is possible within broad ranges of temperature (23–80 °C) and RH (15%–90%).
(c) The steady-state WVTR values can be determined more rapidly because measurements can be taken at high temperatures, with 30 measurement cells operating at the

same time independent of the barrier performance of the samples.

(d) The combination of measurements and advanced theoretical calculations based on the finite element method (FEM) allows us to predict steady-state WVTR values accurately, long before steady-state conditions have been reached.

II. THEORETICAL BACKGROUND

A. Basic principles of permeation

The permeation process involves mass transport over a certain time period through a solid, which has at least two surfaces acting as boundaries to the surrounding gas. It is characterized by four stages.

The adsorption of gas molecules on the surface of the solid (polymeric) sample is followed by the absorption in the near-surface volume area. At sufficiently low partial pressures of permeating gas molecules, the amount of gas absorbed per volume of the solid sample can be described by Henry's law (1), which is applicable if the substance sorbed in the polymer does not dissociate. Here, c is the equilibrium concentration in the polymer, S is the solubility coefficient, and p is the partial pressure of the gas,[17]

$$c = S \times p. \tag{1}$$

The third step is the diffusion of the gas molecules through the solid. Diffusion was described quantitatively for the first time by Adolf Fick[18] using the diffusion coefficient D and the locally varying concentration c of the permeating substance. This yields Fick's first law (2) for the (molar) flux density j of a permeating substance (shown here in its one-dimensional form),[19,20]

$$j = -D\frac{\partial c}{\partial x}. \tag{2}$$

The concentration c of the diffusing substance remains constant over time at every point in the material, when the permeation process has reached its steady state. The time dependence of c is given by Fick's second law (3a), also shown in its one-dimensional form,

$$\frac{\partial \mathrm{c}}{\partial t} = D\frac{\partial^2 \mathrm{c}}{\partial x^2}. \tag{3a}$$

Finally, the gas molecules escape from the solid on the opposite film surface and desorb into the surrounding atmosphere. This process is the counterpart to the absorption step and usually also follows Henry's law.

Typically, WVTRs are recorded as a function of time as shown in Fig. 1 (In this paper, the term transmission rate is used for the (mass) flux density). After the start of water vapor absorption in the sample, the WVTR value approaches asymptotically to a stationary permeation value (dotted line).

B. Numerical simulation of water vapor permeation

We used the simulation program COMSOL Multiphysics Version 4.4, which is based on FEM and can solve physical problems described by partial differential equations.[21,22]

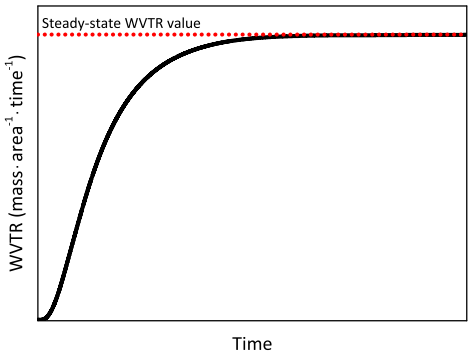

FIG. 1. Schematic representation of the time-dependent permeation starting with dry film.

The time-dependent change of the concentration c of water vapor in a multilayer structure (Fig. 2) can be described within each layer L_i of thickness h_i by Fick's second law,

$$\frac{\partial c_i}{\partial t} = D_i\frac{\partial^2 c_i}{\partial x^2}, \tag{3b}$$

assuming that the diffusion coefficients D_i and solubility coefficients S_i are concentration independent.

The solutions of the diffusion equation in two adjacent layers i and $i+1$ are coupled by the following conditions Eqs. (4) and (5), must be fulfilled at their interface on the x-axis $x = h_1 + \cdots + h_i$, and are implemented in COMSOL. The chemical potential and, therefore, the partial pressure $p = \frac{c}{S}$ of the water vapor are continuous at interfaces,

$$\frac{c_i\,(t, h_1 + \cdots + h_i)}{S_i} = \frac{c_{i+1}\,(t, h_1 + \cdots + h_i)}{S_{i+1}}. \tag{4}$$

The conservation of the amount of permeating water vapor results in the continuity of the normal component of its flux density $j = -D\frac{\partial c}{\partial x}$,

$$D_i\frac{\partial c_i}{\partial x}\,(t, h_1 + \cdots + h_i) = D_{i+1}\frac{\partial c_{i+1}}{\partial x}\,(t, h_1 + \cdots + h_i)\,. \tag{5}$$

During the drying period, the initial concentration of water vapor within each layer i at time $t = 0$ is defined as $c_i\,(0, x) = S_i\tilde{p}$ with $\tilde{p} = 1.4$ kPa, which is equal to the ambient water vapor partial pressure (23 °C and 50% RH). The concentrations at each boundary $x = 0$ and $x = h$ are set to zero. During the permeation period, the concentrations in the layered structure at the boundaries $x = 0$ and $x = h$ correspond to the partial pressures according to Henry's law (1), e.g., 2.4 kPa for the measurement condition of 38°C/36% RH, and 0 kPa, respectively.

III. MATERIALS

In order to find the lower detection limit and determine the accuracy of the ultra-permeation accumulation (UPA) measurement device, we selected laminate films from Toyo Seikan, Co., Ltd, consisting of polyamide, polyester, Al foil (6 μm thick), and polyethylene. These films are typically used for control measurements in the commercially available MOCON® Aquatran® devices. The structure of these Al foil laminate (AFL) films is shown in Table I.

TABLE I. Summary of permeation barrier films used for the study.

Code	Total thickness (μm)	Inorganic layer	Number/individual thickness of inorganic layers	Structure	Producer
AFL	91	Al	1/6 μm	PA/PET/Al/PE	Toyo Seikan, Co., Ltd.
PCTFE[25]	76		0		Honeywell International, Inc.
HBF	105	SiO_x	4/100 nm	PET/SiO_x/ ORM/SiO_x/ adh/SiO_x/ORM/ SiO_x/PET	Amcor Flexibles Kreuzlingen AG, Fraunhofer ISC/IVV

ACLAR® polychlorotrifluoroethylene (PCTFE) is a well-characterized material. We used ACLAR® 3000 films of 76 μm thickness from Honeywell International, Inc., to validate the repeatability of the measurement results.

Furthermore, a high-barrier film (HBF) was produced according to the Fraunhofer POLO® concept,[23] which is based on the coating of alternating inorganic and hybrid-organic barrier layers on the top of a polymeric substrate. The substrate was a polyethylene terephthalate (PET) film from DuPont Teijin Films (a newly developed version of PET Melinex®). This has greater outdoor stability than standard PET, without any effect on the final water vapor barrier performance of the multilayered structures.

The inorganic barrier layers (transparent silicon oxide, SiO_x) were deposited using physical vapor deposition by electron beam evaporation (Amcor Flexibles Kreuzlingen AG). An ORMOCER® (ORM) lacquer was applied as an intermediate hybrid-polymeric layer by a reverse-gravure process at Fraunhofer IVV, Freising. These lacquers are organically modified ceramics, which were synthesized in a sol-gel process from organo-alkoxysilane precursors, by Fraunhofer ISC, Würzburg.[24]

The HBF was produced by the face-to-face adhesive (adh) lamination of the two barrier films. Each of these films consisted of the new outdoor stable PET Melinex® substrate (50 μm thick) coated with SiO_x (100 nm), ORM (1 μm), and a second layer of SiO_x (100 nm). The final structure of the HBF is shown in Table I.

IV. ULTRA-PERMEATION ACCUMULATION MEASUREMENT DEVICE

Fig. 3 shows a schematic diagram of the ultra-permeation accumulation (UPA) measurement device developed at Fraunhofer IVV. A previous version of this unit has already been described.[26]

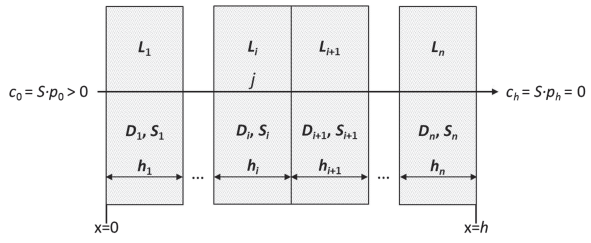

FIG. 2. Geometry of the multi-layered structure.

Compared to the original version, this tailor-made unit has been modified to include new options allowing the transient and steady-state WVTR to be measured in barrier films under different conditions. Sample films with a diameter of 155 mm are mounted inside 30 identical measurement cells, which are placed in a temperature-controlled chamber. This allows the measurement of 30 different films at the same time. The measurement cells include dry He-flushed elastomeric double seals to minimize the possible leakage of water vapor through the samples' edges or the inner seal. The large sample size improves the measurement sensitivity by increasing the area for water vapor to permeate into the dry chamber.

The system includes two 16-way selector valves each covering 15 measurement cells. The permeated water vapor from each of the measurement cells is transported via He gas through the valves to the pre-trap. One He pipe is not connected to a measurement cell but directly connects the gas-inlet and the pre-trap allowing water leakages to be detected and controlled during the measurement.

The RH of the nitrogen flow can be varied between 15% and 90%, by mixing dry and humid nitrogen. A sensor (HMP238 from Vaisala) placed within the temperature-controlled chamber measures the RH of the gas mixture with an accuracy of 0.5% and controls the flow ratio via proportional-integral-derivative (PID) controlled flow meters. Furthermore, the drying and measurement temperatures can be varied from 23 °C to 80 °C with an accuracy of ±0.1 °C.

The entire system, including the barrier films, is conditioned properly before measurement to ensure well-defined initial conditions. During this period, the whole unit is heated to 50 °C and flushed with nitrogen that has been dried in a cooling trap, to remove residual water within the samples and the apparatus. The zero value is measured individually for each measurement cell providing an intrinsic indicator for the leak rate of the system.

After this drying period (Fig. 4), humid nitrogen is admitted to the measurement cells and comes in contact with the upper side of the films within the measurement cells. Due to the partial-pressure difference, water vapor starts to permeate towards the dry side and is then carried to the pre-trap by He, where the water is adsorbed and accumulates for 10 min. The pre-trap is filled with Chromosorb® 104 (Imerys Minerals California, Inc., USA) material and operates at room

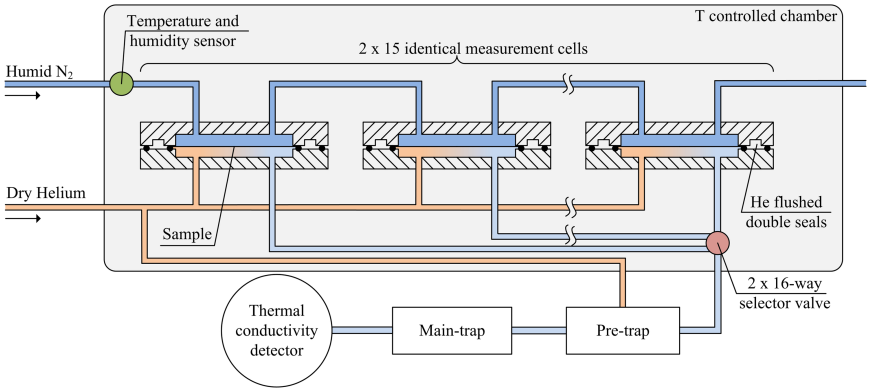

FIG. 3. Schematic diagram (cross-sectional view) of the UPA device based on the accumulation of water vapor on a pre- and main-trap of Chromosorb® 104 and Tenax®, respectively.

temperature. The accumulation of water vapor in the pre-trap allows us to detect very low WVTR values.

In the next step, the adsorbed water is thermally desorbed at 240 °C, transferred into the main-trap, which is filled with Tenax® polymer (Buchem B.V., Netherlands), and there, it is frozen at −50 °C. After the second thermal desorption step at 200 °C, the water is transferred to and quantified by a thermal conductivity detector with a detection limit of 5×10^{-7} g m^{-2} d^{-1}. This detector measures the thermal conductivity of the surrounding atmosphere, which can be related by a calibration factor to the mass of water that permeated per area and time (e.g., g m^{-2} d^{-1}). Calibration was carried out as previously described.[26] The measurement cycle of each cell took ~22 min, so each cell was measured every 12 h. The measurements were stopped as soon as a steady-state permeation value was reached.

The conventional approach to define steady-state conditions is strongly influenced by the resolution of the measurement device and the experimental methodology. Numerical simulation of the time-dependent initial phase of the measured permeation rate with the COMSOL simulation program allows us to calculate the steady-state WVTR. The measurement can be stopped as soon as the mean of the last five measurement values is within 1.5% of the calculated steady-state WVTR value. For barrier films with very long lag times, the measurement can be stopped earlier and the extrapolated steady-state value can be used. This enables us to reduce the measurement times for high-barrier films significantly.

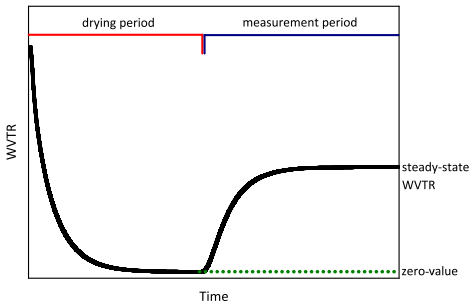

FIG. 4. Schematic representation of the time-dependent WVTR showing an initial drying period and the measurement period.

V. RESULTS

A. Limit of detection and repeatability

The AFL film described above was used to determine the detection limit of the UPA device. The initial measurements were taken under dry conditions of 38 °C and 0% RH for 7 days (drying period). When the values were within a standard deviation of 1.5% within 3 days, a steady-state zero value was achieved. The mean of the last five measurement values was 2.5×10^{-5} g m^{-2} d^{-1} with a standard deviation $\sigma_{WVTR_{zero}}$ of 1.0×10^{-5} g m^{-2} d^{-1}. After this zeroing period, the relative humidity was set to 36%. The WVTR was measured as a function of time and is shown in Fig. 5. There was a slight increase in the values compared to the drying period due to the pinholes in the Al foil. The mean and standard deviation $\sigma_{WVTR_{steady}}$ of the last five values, calculated using the same procedure applied during the zeroing period, were 6×10^{-5} and 1.6×10^{-5} g m^{-2} d^{-1}, respectively. Therefore, the WVTR for this AFL sample, calculated by subtracting the mean of the zeroing period from the mean of the measurement period, was 3.1×10^{-5} g m^{-2} d^{-1} with a standard deviation $\sigma_{WVTR_{total}} = \sqrt{(\sigma_{WVTR_{zero}})^2 + (\sigma_{WVTR_{steady}})^2}$ of 1.9×10^{-5} g m^{-2} d^{-1}.

If the difference between the two mean values is significant, it is at least twice the standard deviation $\sigma_{WVTR_{zero}}$, i.e., 2×10^{-5} g m^{-2} d^{-1}. This value is the smallest significant

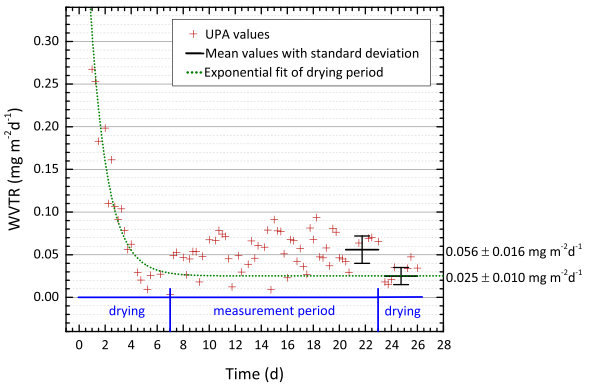

FIG. 5. Water permeation flux through Al foil laminate (AFL) film as a function of time.

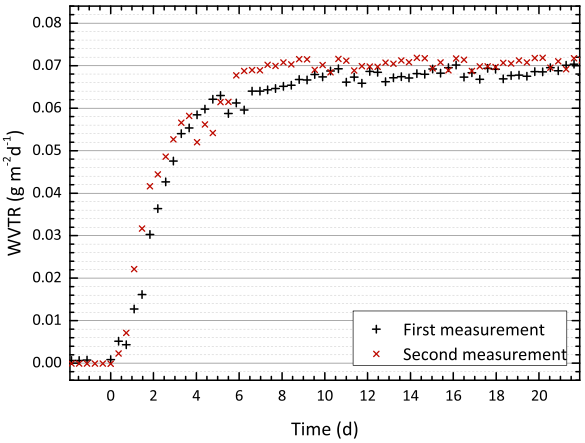

FIG. 6. Example of two consecutive measurements of the PCTFE film in one measurement cell at 40 °C and 75% RH.

amount of change that can be detected by the UPA device at an accumulation time of 10 min, which is the measurement sensitivity.

Fig. 6 provides one example of the two measurements of a PCTFE film in one measurement cell to determine whether the results are reproducible. Therefore the film was measured twice consecutively at 40 °C and 75% RH.

The WVTR curves showed close agreement, with calculated mean values of 69.5 mg m^{-2} d^{-1} for the first measurement and 70.5 mg m^{-2} d^{-1} for the second. The deviation between consecutive measurements in one measurement cell was 1.5%, which is similar to the changes in the atmospheric pressure observed during the measurement.

It is important to ensure that the barrier film does not undergo any structural changes due to water during measurement because this would influence the permeation rate.

B. Validation of measurement results with well-characterized materials

Table II shows the average WVTR values and 95% confidence intervals $\Delta\bar{x}$ obtained for PCTFE films in g m^{-2} d^{-1}. Fifteen samples were measured simultaneously in individual measurement cells. To validate the results, the WVTRs were also measured using the commercially available coulometric method (MOCON® Aquatran®) in accordance with DIN EN ISO 15106-3 for plastic films. The specified measurement limit of the MOCON® Aquatran® Model 2 is 5×10^{-5} g m^{-2} d^{-1}.[15,27,28] These measurements were taken twice so both values are presented rather than the mean. One of the advantages of the UPA device is its ability to measure up to 30 samples simultaneously, providing more reliable data more rapidly.

TABLE III. WVTR values of the high-barrier film (HBF) at different conditions measured with the UPA device as well as with MOCON® Aquatran® devices.

38 °C/36% RH (g m^{-2} d^{-1})		38 °C/90% RH (g m^{-2} d^{-1})	
UPA	Aquatran	UPA	Aquatran
6.0×10^{-4}	6.8×10^{-4}	3.5×10^{-3}	2.6×10^{-3}
6.4×10^{-4}	5.2×10^{-4}	3.2×10^{-3}	3.9×10^{-3}
7.0×10^{-4}	7.0×10^{-4}	3.6×10^{-3}	4.2×10^{-3}
7.3×10^{-4}	4.8×10^{-4}	3.3×10^{-3}	

The WVTR values obtained by the UPA device agree closely with those obtained using the MOCON® Aquatran® and with the manufacturers' data sheets. The largest deviation was detected at 40 °C and 75% RH. Here, the UPA values lie between the Aquatran® values and those provided by the manufacturer.

The WVTR values of the HBF (structure as shown in Table I) measured with the UPA and the Aquatran® devices at 38 °C and two different RH (36% and 90%) are shown in Table III.

The WVTR values determined using the UPA device agreed again closely with the values determined using the Aquatran® device. The small deviations in the measurements mainly reflect the processing and handling of the multilayered films.

C. Rapid determination of steady-state WVTRs

The simulation tools described in Section II B were used to predict the steady-state WVTR based on the values measured as a function of time before the steady state was achieved. This helps to reduce the experimental measurement times from several months to a few weeks. Fig. 7 shows the mean WVTRs and standard deviations of four specimens, calculated at each measurement time, through the HBF as a function of time. The WVTR values at the steady state are shown in Table III.

TABLE II. WVTR values of Honeywell ACLAR® PCTFE films at various measurement conditions measured using 15 measurement cells of the UPA device in comparison to MOCON® Aquatran® measurements and the WVTR values given by the producer.[25] Confidence intervals $\Delta\bar{x}$ have been calculated with a confidence level of 95%.

	25 °C/60% RH (g m^{-2} d^{-1})			30 °C/65% RH (g m^{-2} d^{-1})			40 °C/75% RH (g m^{-2} d^{-1})		
	WVTR	$\Delta\bar{x}$	n	WVTR	$\Delta\bar{x}$	n	WVTR	$\Delta\bar{x}$	n
UPA	9.8×10^{-3}	1.6×10^{-4}	15	2.8×10^{-2}	2.5×10^{-4}	15	6.7×10^{-2}	7.0×10^{-4}	15
Aquatran®	1.3×10^{-2}						8.1×10^{-2}		
	1.2×10^{-2}						7.9×10^{-2}		
Data sheet[25]	1.2×10^{-2}			2.3×10^{-2}			6.2×10^{-2}		

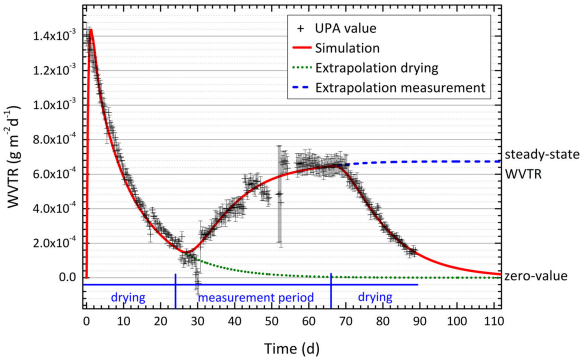

FIG. 7. WVTR of the HBF as a function of time (UPA value) with the standard deviations of four measurements. The solid, dotted, and broken lines are calculated curves from COMSOL.

During this measurement, the film was initially dried for 24 days at 38 °C, then humidified for 42 d at 36% RH, and finally (starting at day 66) dried again. The solid line in Fig. 7 is the calculated water permeation flux curve for the structure shown in Fig. 8. The thickness of each layer is shown in Table IV. By varying the simulation parameters until there was a close match between the numerical and experimental data, we were able to determine the D and S values of SiO_x, ORM, and adhesive (adh) layers. The values for PET were taken from the literature.[29] The variation of the measurement conditions in the simulation allows the zero value (dotted line) and the steady-state value (broken line) to be calculated.

There may be several combinations of all D and S values, all of which give water vapor permeation flux density curves similar to the one shown in Fig. 7. Nevertheless, the D and S values are physically reasonable because the D and S values of PET, ORM, and adhesive are in the same order of magnitude. The main parameters affecting the water vapor permeation flux density and the time lag are the diffusion (D) and the solubility (S) of SiO_x because their values are much lower than those of the polymeric and hybrid-polymeric materials involved. The calculated curve using the D and S values in Table IV represents the average measurement curve with high precision and allows us to calculate the mean steady-state WVTR. In this paper, the D and S values we determined are called as effective diffusion (D_{eff}) and solubility coefficients (S_{eff}).

In the second measurement (Fig. 9), the measurement time was reduced from 42 d to 7 d. Nevertheless, the calculated solid curve can still be adapted to the experimental data, leading to the same steady-state WVTR of 6.7×10^{-4} g m^{-2} d^{-1}. Importantly, the simulation was performed using the same parameters as described above. This indicates that the

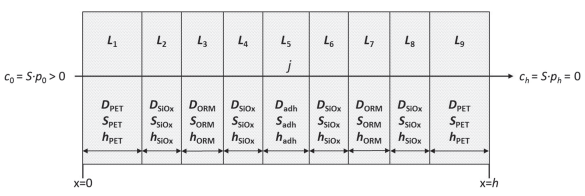

FIG. 8. Structure of the HBF as given in Table I.

TABLE IV. Diffusion (D_{eff}) and solubility coefficients (S_{eff}) used to calculate the water permeation flux curves of the HBF (solid lines in Figs. 7 and 9).

	D_{eff} (m^2 s^{-1})	S_{eff} (mol m^{-3} Pa^{-1})	h (μm)
PET[29]	4×10^{-14}	2	5×10^{1}
SiO_x	2.5×10^{-15}	2.9×10^{-5}	1×10^{-1}
ORM	1×10^{-14}	3.5×10^{-1}	1
adh	1×10^{-14}	2.5×10^{-1}	2

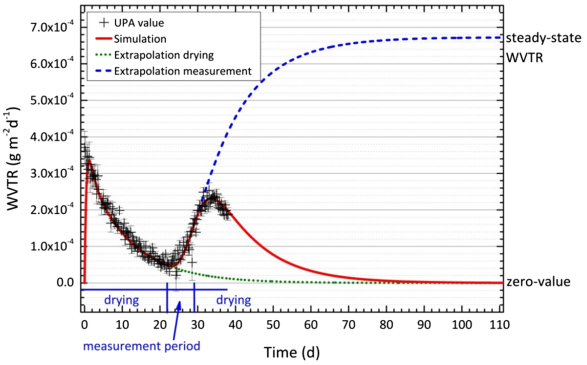

FIG. 9. WVTR of the HBF as a function of time with reduced measurement time (UPA value) with the standard deviations of four measurements. The solid, dotted, and broken lines are calculated curves from COMSOL.

characteristic time constants of the system, which are mainly a function of the materials D and S, are well reproduced by the model under changing boundary conditions. Although it is difficult at this stage to determine if the parameters represent a global minimum for the least square fit, this test supports the determined effective values in Table IV. The whole measurement time, including both the drying and measurement periods, was reduced from ~90 d to ~40 d.

VI. CONCLUSIONS

The ultra-permeation accumulation (UPA) measurement device described herein makes it possible to measure the water vapor permeation time resolved at different temperatures (23 °C–80 °C) and relative humidities (15% RH–90% RH) for 30 samples simultaneously. The sensitivity of the measurement device is 2.0×10^{-5} g m^{-2} d^{-1}. The validation of WVTR values with PCTFE films under different conditions agreed well with values measured using the MOCON® Aquatran® devices and values reported by the manufacturer of the films. The WVTR values measured for a multilayer high-barrier film are in close agreement with the values measured using commercial devices. Numerical simulation of the diffusion equation allows us to calculate the D and S values of each layer of a multi-layered structure. This helps to predict the steady-state WVTR values of ultra-high barrier structures in a much shorter measurement time, i.e., before the steady-state value is reached. In this manner, it becomes possible to reduce the long permeation measurement times for multilayer high barrier structures from several months to a few weeks.

ACKNOWLEDGMENTS

The authors want to thank Tobias Schmidt for his support in the development of the adjustable gas humidification. Furthermore we thank DuPont Teijin Films, Amcor Flexibles Kreuzlingen AG, and Fraunhofer ISC for the supply of barrier materials and films. This work was partly financially supported by the European Union 7th Framework Program under Grant Agreement Nos. 260086 (NANOINSULATE project), 280581 (NANOMEND project), and 287594 (SUNFLOWER project).

[1] H.-C. Langowski, *Plastic Packaging* (Wiley-VCH Verlag GmbH & Co. KGaA,Weinheim, 2008), p. 297.
[2] J. S. Lewis and M. S. Weaver, IEEE J. Sel. Top. Quantum Electron. **10**, 45 (2004).
[3] L. Moro and R. J. Visser, *Organic Photovoltaics: Materials, Device Physics, and Manufacturing Technologies*, edited by C. Brabec, V. Dyakonov, and U. Scherf (Wiley-VCH Verlag GmbH & Co. KGaA, Weinheim, 2008), p. 491.
[4] T. Shimada, Y. Takahashi, and T. Kanno, Appl. Phys. Express **3**, 021701 (2010).
[5] B. I. Choi, H. S. Nham, S. B. Woo, and J. C. Kim, J. Korean Phys. Soc. **53**, 2179 (2008).
[6] R. Dunkel, R. Bujas, A. Klein, and V. Horndt, Proc. IEEE **93**, 1478 (2005).
[7] G. Nisato, P. C. P. Bouten, P. J. Slikkerveer, W. D. Bennett, G. L. Graff, N. Rutherford, and L. Wiese, *21st Annual Asia Display, 8th International Display Workshop, Nagoya, Japan* (2001), p. 1435.
[8] R. Paetzold, A. Winnacker, D. Henseler, V. Cesari, and K. Heuser, Rev. Sci. Instrum. **74**, 5147 (2003).
[9] J. H. Choi, Y. M. Kim, Y. W. Park, J. W. Huh, B. K. Ju, I. S. Kim, and H. N. Hwang, Rev. Sci. Instrum. **78**, 064701 (2007).
[10] S. Schubert, H. Klumbies, L. Müller-Meskamp, and K. Leo, Rev. Sci. Instrum. **82**, 094101 (2011).
[11] G. L. Graff, R. E. Williford, and P. E. Burrows, J. Appl. Phys. **96**, 1840 (2004).
[12] P. J. Brewer, B. A. Goody, Y. Kumar, and M. J. T. Milton, Rev. Sci. Instrum. **83**, 075118 (2012).
[13] M. O. Reese, A. A. Dameron, and M. D. Kempe, Rev. Sci. Instrum. **82**, 085101 (2011).
[14] P. J. Brewer, B. A. Goody, P. T. Woods, and M. J. T. Milton, Rev. Sci. Instrum. **82**, 105102 (2011).
[15] MOCON, Inc., AQUATRAN Model 2: High Sensitivity Coulometric Water Vapor Transmission Rate Test System: Brochure, 2014.
[16] W. Grählert, H. Beese, J. Grübler, J. Koch, K. Pietsch, and S. Kaskel, LOPE-C, Munich, 2013.
[17] C. E. Rogers, *Polymer Permeability*, edited by J. Comyn (Chapman & Hall, London, 1985), p. 11.
[18] W. R. Vieth, *Diffusion in and through Polymers: Principles and Applications* (Hanser, New York, 1991).
[19] G. Menges, E. Haberstroh, W. Michaeli, and E. Schmachtenberg, *Werkstoffkunde Kunststoffe* (Carl Hanser Verlag, Munich, 2011), Vol. 6.
[20] J. Crank, *The Mathematics of Diffusion* (Oxford University Press, Ely House, London, 1975), Vol. 2.
[21] P. O. J. Scherer, *Computational Physics: Simulation of Classical and Quantum Systems* (Springer International, 2013).
[22] O. C. Zienkiewicz and R. L. Taylor, *The Finite Element Method: The Basis* (Butterworth-Heinemann, Oxford, 2000), Vol. 1.
[23] S. Amberg-Schwab, K. Noller, U. Weber, and O. Miesbauer, "Hochbarrierenverbunde und Verfahren zu ihrer Herstellung," EP patent 2,272,928 A1 (12 January 2011).
[24] S. Amberg-Schwab, M. Hoffmann, H. Bader, and M. Gessler, J. Sol-Gel Sci. Technol. **13**, 141 (1998).
[25] Honeywell International, Inc., Honeywell Aclar UltRx 3000, Data Sheet, 2010.
[26] H. Simmler, S. Brunner, U. Heinemann, H. Schwab, K. Kumaran, P. Mukhopadhyaya, D. Quénard, H. Sallée, K. Noller, E. Kücükpinar-Niarchos, C. Stramm, M. Tenpierik, H. Cauberg, and M. Erb, Annex 39 "HiPTI – High Performance Thermal Insulation" of IEA/ECBCS-Implementing Agreement, Report on Subtask A, (2005), p. 59.
[27] Z. Scheuerer and M. Jesdinszki, Verpack.-Rundsch. **4**, 48 (2013).
[28] DIN EN ISO 15106-3:2003, Kunststoffe - Folien und Flächengebilde - Bestimmung der Wasserdampfdurchlässigkeit - Teil 3, Elektrolytnachweis-Sensorverfahren, 2005.
[29] J. Brandrup, E. H. Immergut, and E. A. Grulke, *Polymer Handbook*, 4th ed. (Wiley Interscience Publication, 1999).

4.2 Time-dependent water vapor permeation through multilayer barrier films: Empirical versus theoretical results [2]

Summary

After the validation of the UPA measurement results as discussed in Chapter 4.1, the next step was to measure the water vapor permeability as a function of time for multilayer films with alternating inorganic barrier (**B**) and polymeric (**P**) layers. Films with up to 11 layers were characterized with respect to their water vapor permeability, solubility and diffusivity of each layer based on measurements of water absorption, transient water vapor permeation and lag times.

Based on these data and the calculations performed using the ideal laminate theory, the permeability $Q_{\mathbf{B}}$ of the SiO_x layers used in the experiments is up to five orders of magnitude lower than that of the polymeric layers, and has the greatest impact on the steady-state WVTRs. The lag times are longer for the structures incorporating **BPB** triplets. Laminate structures, which contain a thick **P** layer with a high solubility coefficient $S_{\mathbf{P}}$ embedded between barrier layers, showed the longest lag times in this study.

The D and S coefficients of the polymer layers in the multilayer structures were determined experimentally in free-standing test specimens by measuring the sorption of water vapor. The water vapor permeability coefficients **P** were calculated as the product of D and S. The polymeric layer, which was an organic modified ceramic (ORMOCER® (ORM)) had the lowest D and the highest S among the tested polymers.

The $Q_{\mathbf{B}}$ values for the first and second SiO_x layers of the multilayered structures were derived from ideal laminate theory calculations and indicate that in this case the first SiO_x layer may be 10 times more permeable than the second one. The reason for this is a planarization effect of the ORM layer, which creates a smoother surface on which the second SiO_x layer is applied and therefore has less defects. This effect was previously reported for fluoropolymer substrates as well [146].

[2] Kiese S., Kücükpinar E., Miesbauer O., and Langowski H.-C., Time-dependent water vapor permeation through multilayer barrier films: Empirical versus theoretical results, *Thin Solid Films* **672**, 199-205 (2019).

In addition to the experimental investigations, the transient WVTRs and lag times of the **BPB**-structures were estimated using the QSS approximation [32]. The predicted permeability values and lag times in multilayer structures were consistent with the values determined by WVTR measurements. Accordingly, the stationary WVTR of **BPB**-type and **BPBPBPB**-type barrier films is dominated by the permeability of the **B** layer, while the lag time is additionally determined by higher solubility coefficient and thickness of the tested polymer layers.

With these experiments the theoretical QSS approximations could therefore be validated for **BPB** or **BPBPBPB** sequences, allowing to predict the barrier performance and lag times of such multilayer structures and significantly reduce the time required for experiments.

Author contributions:

- Sandra Kiese: corresponding author, conceptualization, experimental and theoretical investigations, data evaluation and interpretation, formal analysis, outline, writing original draft, editing, completion
- Esra Kücükpinar: outline, writing - revision, editing and completion
- Oliver Miesbauer: advice on theoretical analysis, validation and revision
- Horst-Christian Langowski: supervision, writing - review & editing

Thin Solid Films 672 (2019) 199–205

Contents lists available at ScienceDirect

Thin Solid Films

journal homepage: www.elsevier.com/locate/tsf

Time-dependent water vapor permeation through multilayer barrier films: Empirical versus theoretical results

Sandra Kiese[a,b,*], Esra Kücükpinar[b], Oliver Miesbauer[a], Horst-Christian Langowski[a,b]

[a] Technical University of Munich, TUM School of Life Sciences Weihenstephan, Chair of Food Packaging Technology, Weihenstephaner Steig 22, Freising, 85354, Germany
[b] Fraunhofer Institute for Process Engineering and Packaging IVV, Giggenhauser Str. 35, Freising, 85354, Germany

ARTICLE INFO

Keywords:
Water vapor permeation
Diffusion
Sorption
Transient
Stationary
Time-dependent measurement

ABSTRACT

Multilayer films that comprise alternating inorganic barrier and polymer layers deposited on a flexible substrate are often used to protect organic electronic devices from degradation caused by oxygen and water vapor. We tested films consisting of up to 11 inorganic silicon oxide barrier and polymer layers to characterize the water vapor permeability, solubility and diffusivity of each layer based on measurements of water sorption, transient water vapor permeation and lag times. The time-dependency of transient water vapor transmission rates (WVTR) of the structures containing a barrier-polymer-barrier sequence was also estimated using a so-called quasi-steady-state (QSS) approximation. The permeability values and lag times in multilayer structures predicted by QSS approximation agreed with the values determined empirically based on time-dependent WVTR measurements. The steady-state WVTR of the multilayer barrier films was dominated by the permeability of the inorganic barrier layers, whereas the solubility coefficient and thickness of the interleaved polymer layers determined the lag times. The barrier performance and lag time of multilayer structures can be predicted using the parameters obtained from sorption measurements, thus significantly reducing the time required for experiments. The results of this study will allow us to design multilayer barrier films according to the lifetime requirements of flexible organic electronic devices.

1. Introduction

Polymeric films such as polyethylene terephthalate (PET) and polyethylene naphthalate (PEN) can be coated with vacuum deposited inorganic layers and used as a packaging material for many food and technical products [1,2]. Although the oxygen and water vapor barrier performance of such films is sufficient for most food packaging applications, technical products such as sensitive organic electronic devices must be encapsulated using materials with more robust barrier properties [1]. The state-of-the-art approach for the production of such encapsulation films is the deposition of alternating inorganic barrier (**B**) layers (e.g. SiO_x, Si_3N_4 or Al_2O_3) and polymer (**P**) layers on a polymer substrate [1,3,4,5,6,7].

Several models can be used to describe permeation through a substrate film coated with a thin inorganic barrier layer. Water vapor permeation through barrier films composed of alternating polymer and high-quality (but still nanoporous) inorganic barrier layers can be described using the ideal laminate model [8,9,10,11,12,13]. This assumes that a significant quantity of water is dissolved in the inorganic material and it permeates through quasi-homogeneous nano-defects, whereas permeation through macro-defects (larger than 1 nm) is negligible [11,14]. The inorganic and polymeric layers are therefore considered as homogeneous and the multilayer structure represents the equivalent of an electrical serial resistance towards water vapor permeation.

The lag time is calculated according to an analytical relationship [15,16], based on combinatorial considerations for structures consisting of **B** and **P** layers. Accordingly, a long lag time can be achieved by embedding a thick **P** layer between two **B** layers (**BPB** sequence) when the ratios of the permeability and the solubility coefficients of the polymer layers (P_P and S_P) and the inorganic layers (P_B and S_B) are high, i.e. $P_P/P_B > S_P/S_B > 100$ (internal desiccant effect) [16,17,18].

In order to improve the barrier properties of multilayer high-barrier films, a systematic investigation of the permeation mechanisms is required, which also considers the effect of the layer order within the multilayer structure. Depending on the structure and quality of a multilayer barrier film, it may take a long time to approach a steady-state water vapor transmission rate (WVTR). Using a combination of time-dependent permeation measurements and theoretical approximations, the time-dependent

* Corresponding author at: Technical University of Munich, TUM School of Life Sciences Weihenstephan, Chair of Food Packaging Technology, Weihenstephaner Steig 22, Freising, 85354, Germany
E-mail address: Sandra.kiese@ivv.fraunhofer.de (S. Kiese).

https://doi.org/10.1016/j.tsf.2019.01.001
Received 25 June 2018; Received in revised form 27 November 2018; Accepted 2 January 2019
Available online 14 January 2019
0040-6090/

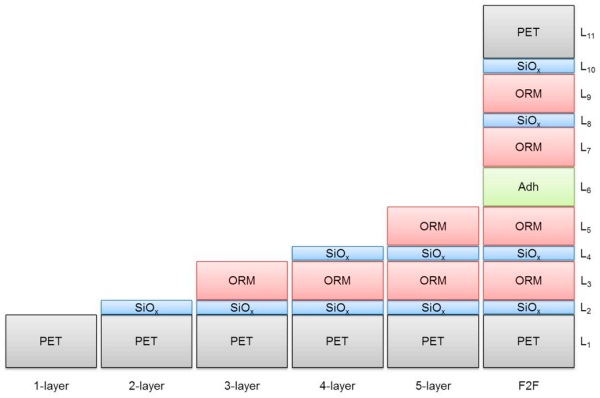

(a) Barrier film structures used in this study. L_i represents the layer number.

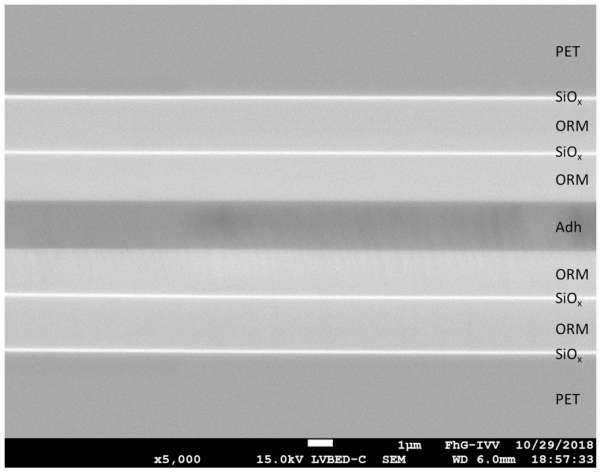

(b) Scanning electron microscope image of the barrier layers of the F2F laminate structure at 5000× magnification.

Fig. 1. Schematic view of barrier film structures (a) and cross-sectional scanning electron microscope image of the F2F laminate (b).

and steady-state WVTR values and the lag time of a multilayer barrier film can be estimated within significantly shorter experimental timeframes [19]. Here we focused on the measurement and theoretical calculation of time-dependent WVTRs and the interpretation of lag times, addressing the effects of water vapor solubility coefficients, the permeability of individual layers and of layer sequences on the WVTR values and lag times of multilayer structures.

2. Materials and methods

2.1. Production of multilayer barrier films and laminates

The barrier films for WVTR analysis were produced according to the Fraunhofer POLO® concept [20] by the deposition of alternating inorganic barrier and hybrid-polymer layers onto a polymer substrate film. The final structures of all barrier films are shown in Fig. 1a and were prepared as follows. A 50 µm (Melinex® 401) PET film (DuPont Teijin Films, UK) was coated with an inorganic layer consisting of transparent silicon oxide (SiO_x) applied at a thickness of 100 ± 10 nm by electron beam evaporation (AMCOR Flexibles Kreuzlingen AG, Switzerland). An ORMOCER® (ORM) lacquer was applied as an intermediate hybrid-polymer layer at a thickness of 1.8 ± 0.6 µm by reverse-gravure at Fraunhofer IVV (drying temperature 120 °C) before the deposition of a second inorganic SiO_x layer. A second layer of ORM was applied on top to protect the surface from mechanical damage. The lacquer was prepared by a sol-gel-method at Fraunhofer ISC, Germany. The sol, which was coated wet-chemically on the SiO_x layers, contained (3-glycidyloxypropyl)trimethoxysilane and aluminum-sec-butoxide complexated with ethyl acetoacetate. The so-called face-to-face (F2F) laminate was produced by the adhesive (Adh) lamination of two 5-layer structures. The lamination adhesive was a two-component polyurethane resin (Novacote Flexpack Division of Coim Deutschland GmbH, Germany) applied at a thickness of 1.6 ± 0.4 µm by reverse gravure at Fraunhofer IVV (drying temperature 60 °C). A scanning electron microskopic cross sectional image of the F2F laminate structure is shown in Fig. 1b.

2.2. Production of single-layer materials for sorption analysis

The solubility coefficients of water in the single-layer components of the multilayer barrier films PET, SiO_x, ORM and Adh were determined by water vapor sorption analysis. The ORM and Adh single-layer samples were produced by doctor blading on untreated polypropylene film using a CUF 5 semi-automatic coating unit (Sumet Messtechnik, Germany). Both coatings were applied using a K-bar (K-1.4) to achieve a dry coating thickness of ~55 µm. Hot air was used to dry the coatings at 120 °C (ORM) and 60 °C (Adh). Due to the weak adhesion of the coatings to the polypropylene substrate, they could be removed easily and were measured as free-standing samples.

The solubility coefficient of the SiO_x barrier layer was determined using samples prepared by deposition on a Teflon tape. A vacuum deposition pilot plant (Leybold AG, Germany) at Fraunhofer IVV, featuring an electron-beam evaporation source and microwave plasma generator, was used to deposit a layer of (26.0 ± 1.4) µm thickness. The Teflon tape was removed before the sorption measurements to avoid water sorption within the Teflon.

2.3. Layer thickness measurements

In order to determine the thicknesses of all layers, samples of each barrier film and the laminate structure were prepared by Ar^+-ion beam milling using a cross section polisher IB-19530CP (JEOL Ltd., Japan). All samples were coated with a gold layer using electron beam evaporation, to reduce electrical charging of the non-conducting samples. The cross-sectional images were taken with the scanning electron microscope JSM-7200F (JEOL Ltd., Japan).

2.4. Sorption measurements

Water vapor sorption behavior was measured gravimetrically (resolution: ± 20 µg) at 38 °C using a SPSx-1μ micro-balance (ProUmid GmbH & Co. KG, Germany). The samples were transferred to aluminum cups (area 20 cm^2, volume 12 ml) and three specimen from each sample type were analyzed. The ambient water activity was increased from 0% to 50% relative humidity (RH) in 10% increments, and the moisture uptake was recorded at each step as a function of time until a steady-state was attained (defined as < 0.01% weight change in 15 min). The effective solubility coefficient S was calculated according to Henry's law [21,22]

$$c = S \times p, \tag{1}$$

where p is the partial water vapor pressure and c is the equilibrium concentration of water in the polymer.

Starting at $p = 0$, the diffusion coefficient D of a plane sheet of a material can be estimated from the time-dependent sorption behavior [23]:

$$D = \frac{\pi h^2}{64 t_{1/2}}, \tag{2}$$

where h is the sample thickness and $t_{1/2}$ is the time needed during the sorption process to achieve half of the steady-state mass-uptake.

The product of the solubility and diffusion coefficient ($S \times D$) is the permeability coefficient P [1,22,24], which is related to the permeability Q as follows:

$$P = Q \times h. \tag{3}$$

2.5. WVTR measurements and lag time calculations

The WVTRs of PET and the films with up to five layers were measured for 35 d at 38 °C with a water vapor concentration gradient from 36% to 0% RH and the PET substrate facing the humid side of the test chambers. WVTRs were determined using an ultra-permeation accumulation (UPA) device built in-house by Fraunhofer IVV, with a detection limit of 2×10^{-5} gm^{-2}d^{-1} [19]. The WVTR of the F2F laminate structure was also measured for 100 d under the same conditions. Three samples of each film type were analyzed. To remove the residual water from the samples and the apparatus, both sides of the films were initially flushed with dry nitrogen at 50 °C. The zero value, an intrinsic indicator for the leak rate of the system, was then determined by measurement for 7 d at 38 °C under dry conditions. When the difference between the last five measured values fell below 1.5%, the RH on one side of the film was set to 36% (p = 2380 Pa) and WVTRs were measured as a function of time. A detailed description of the UPA device and the measurement procedure has been published elsewhere [19].

In this article, WVTR refers to the time-dependent (mass) flux density $j(t)$, which is related to the permeability and the boundary partial pressure p as follows:

$$j(t) = Q \times p. \tag{4}$$

According to the ideal laminate theory, the steady-state water vapor permeation of a multi-layer structure, Q_{total}, can be calculated as

$$\frac{1}{Q_{\text{total}}} = \sum_{i=1}^{n} \frac{1}{Q_i}, \tag{5}$$

based on the permeability values (Q_i) of the individual layers [1].

The lag time is used to characterize the manner in which $j(t)$ approaches the steady-state value j_{steady}. The amount $n(t)$ of water vapor that has permeated through a film sample of unit area within a sufficiently long time period t is given by

$$n(t) \approx j_{\text{steady}} \times (t - \vartheta), \tag{6}$$

which defines the lag time ϑ [15,23]. The value is determined graphically from permeation measurements as the intersection of the asymptote to the graph of $n(t)$ plottet against time.

2.6. Quasi-steady-state (QSS) approximation for *BPB* and *BPBPBPB* multilayer films

Numerical calculations for transient permeation through multilayer structures consisting of at least one **BPB** triplet showed that the partial pressure profile within each layer is almost linear over the duration of measurement when t is large compared to the lag time [16]. The permeation kinetics can be described using QSS [16]. Accordingly, the $j(t)$ for a **BPB** structure can be calculated as

$$j(t) = \frac{P_{\mathbf{B}} p}{2h_{\mathbf{B}}}\left(1 - \exp\left(-\frac{2P_{\mathbf{B}}}{h_{\mathbf{B}} h_{\mathbf{P}} S_{\mathbf{P}}} t\right)\right), \tag{7}$$

where $P_{\mathbf{B}}$ is the permeability coefficient and $h_{\mathbf{B}}$ the thickness of the **B** layers and where $S_{\mathbf{P}}$ is the solubility coefficient and $h_{\mathbf{P}}$ the thickness of the **P** layer, and p is the boundary partial pressure.

The time-dependent flux density of **BPBPBPB** type structures can be approximated as follows [16]:

$$\begin{aligned} j(t) = {} & \frac{P_{\mathbf{B}} p}{4h_{\mathbf{B}}}\left(1 - \left(\frac{1}{\sqrt{2}} + 1\right)\exp\left((\sqrt{2} - 2)\frac{P_{\mathbf{B}}}{h_{\mathbf{B}} h_{\mathbf{P}} S_{\mathbf{P}}} t\right)\right. \\ & + \exp\left(-2\frac{P_{\mathbf{B}}}{h_{\mathbf{B}} h_{\mathbf{P}} S_{\mathbf{P}}} t\right) \\ & \left. + \left(\frac{1}{\sqrt{2}} - 1\right)\exp\left((-\sqrt{2} - 2)\frac{P_{\mathbf{B}}}{h_{\mathbf{B}} h_{\mathbf{P}} S_{\mathbf{P}}} t\right)\right). \end{aligned} \tag{8}$$

The steady-state WVTR values are the asymptotic values of Eqs. (7) and (8) for large t, i.e.

$$j_{\text{steady}} = \frac{P_{\mathbf{B}} p}{N_{\mathbf{B}} h_{\mathbf{B}}}, \tag{9}$$

with $N_{\mathbf{B}}$ being the number of barrier layers.

Using the two fit parameters $P_{\mathbf{B}}$ and $S_{\mathbf{P}}$, the lag times are calculated as

$$\vartheta = \frac{h_{\mathbf{B}} h_{\mathbf{P}} S_{\mathbf{P}}}{2P_{\mathbf{B}}} \tag{10}$$

for **BPB** type structures and

$$\vartheta = \frac{5h_{\mathbf{B}} h_{\mathbf{P}} S_{\mathbf{P}}}{2P_{\mathbf{B}}} \tag{11}$$

for **BPBPBPB** type structures with more than one **BPB** triplet and $S_{\mathbf{P}} \gg S_{\mathbf{B}}$, derived from Eqs. (7) and (8), according to [16].

In this study, $P_{\mathbf{B}}$ and $S_{\mathbf{P}}$ are the effective permeability and solubility coefficients of the layers in a multilayer structure. They can differ from the coefficients determined for the free-standing test samples, especially for the SiO_x, due to the influences of the substrate material and potential synergistic effects of the adjacent layers in multilayer structures [25,26].

The laminate structure included different types of **P** layers. In order to apply the approximate QSS solution (Eq. (8)) to the laminate structure, they were simplified by assigning a mean $h_{\mathbf{P}} S_{\mathbf{P}}$ to each **P** layer as follows:

$$h_{\mathbf{P}} S_{\mathbf{P}} = \frac{\sum_{i=1}^{n} h_{\mathbf{i}} S_{\mathbf{i}}}{N_{\mathbf{P}}}. \tag{12}$$

For all QSS calculations, the remaining outer polymer layers (PET or ORM) were disregarded, because they are not enclosed in between **B** layers and therefore did not significantly contribute to the barrier performance of the multilayer film, as theoretical considerations have previously shown [16].

3. Results and discussion

3.1. Water vapor solubility coefficients from sorption isotherms

The sorption isotherms for all polymer materials (PET, ORM and Adh) showed a linear relationship when the water concentration was plotted against water vapor partial pressure (Fig. 2) and the solubility coefficients S were calculated according to Eq. (1). The diffusion coefficients (D) were calculated according to Eq. (2) based on the time-dependent sorption behavior of water in the polymer materials. The resulting values are shown in Table 1 and the S, D and P values for PET agree with earlier reports [27,28]. Despite the high layer thickness of ~55 µm of the ORM that we used for the sorption measurement, the values are consistent with the literature, which was measured with ~2 µm thick layers [29]. There were no previously published S and D values for the specific type of Adh used in this study.

The sorption isotherm of the free-standing SiO_x, which was removed from the Teflon tape, is shown in Fig. 3, revealing the non-linear relationship between water vapor concentration and water vapor pressure, and thus the absence of Henry behavior. Nevertheless, at low equilibrium partial pressures < 2380 Pa, corresponding to 36% RH at 38 °C, linear dependency was approximated and a suitable value of

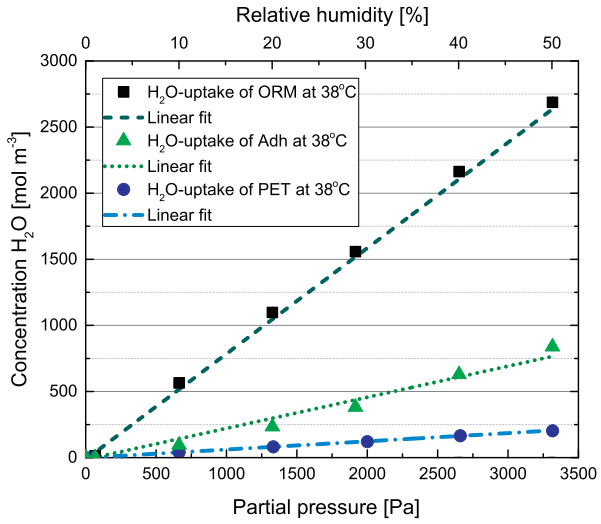

Fig. 2. Sorption isotherm plots of sorbed water as a function of water vapor partial pressure or % relative humidity for ORM, Adh and PET at 38 °C. Mean values of three measurements are plotted with standard deviations. Points represent the experimental data and lines are the linear fits applied using Eq. (1).

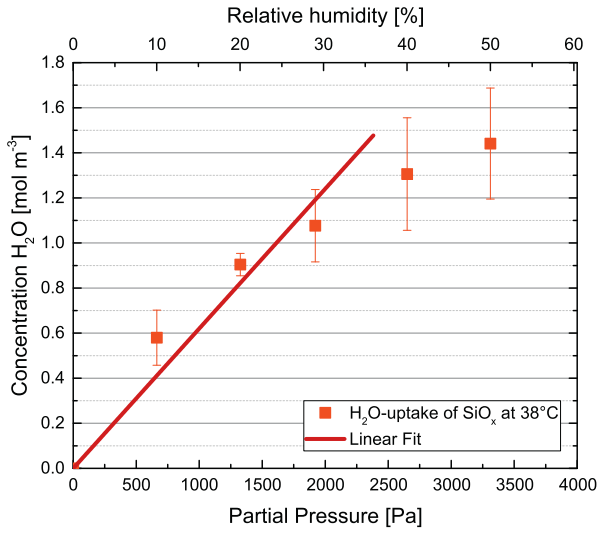

Fig. 3. Sorption isotherm plot of sorbed water at 38 °C as a function of partial pressure or % relative humidity for SiO_x. Mean values of three measurements are plotted with standard deviations. Points represent the experimental data and the line is the linear fit between 0 and 2380 Pa applied using Eq. (1), allowing us to calculate the effective S of SiO_x.

Table 1
Solubility S and diffusion D coefficients of PET, SiO_x, ORM and Adh at 38 °C from sorption measurements. Mean values of three samples are shown with confidence intervals $\Delta\bar{x}$ (confidence level of 95%). D values were calculated using Eq. (2).

	S (mol m^{-3}Pa^{-1})	D (m^{2}s^{-1})	P (mol m^{-1}s^{-1}Pa^{-1})
PET	$(6.2 \pm 0.2)\times10^{-2}$	$(9.2 \pm 0.3)\times10^{-13}$	$(5.7 \pm 0.4)\times10^{-14}$
SiO_x	$(6.1 \pm 1.0)\times10^{-4}$		
ORM	1.3 ± 0.1	$(2.1 \pm 0.4)\times10^{-13}$	$(2.6 \pm 0.4)\times10^{-13}$
Adh	$(2.9 \pm 0.1)\times10^{-1}$	$(8.0 \pm 0.6)\times10^{-12}$	$(2.3 \pm 0.6)\times10^{-12}$

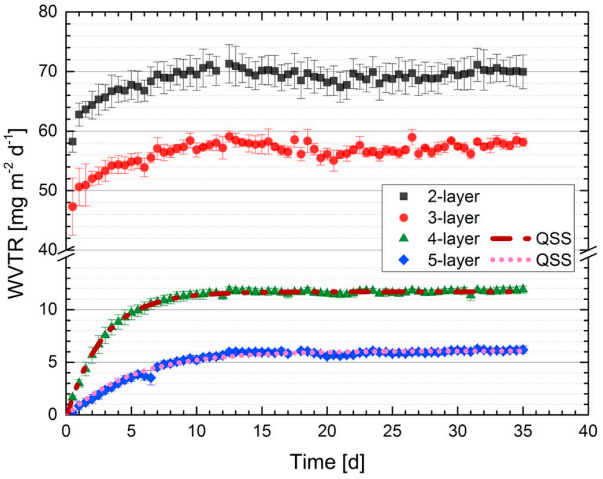

Fig. 4. Experimentally obtained WVTR values for barrier films at 38 °C and 36% RH. Data represent three measurements with standard deviations. For the **BPB**-type structures (4- and 5-layers) the QSS curves (Eq. (7)) are also shown.

$(6.1 \pm 1.0)\times10^{-4}$ mol m^{-3}Pa^{-1} was calculated using the Henry relationship (Eq. (1)). Compared to the polymer samples, the effective solubility coefficient of SiO_x was three orders of magnitude lower for ORM and Adh and two orders of magnitude lower for PET (Table 1). This S is an effective value for the thick SiO_x, which was coated on the Teflon tape and it can be different from the solubility coefficient of a thinner SiO_x in a multilayer structure, which was coated on PET or an ORM layer. Nevertheless, this value shows the order of magnitude of the S_{SiO_x} and justifies the use of the QSS approximation, where S_P/S_B has to be > 100.

The total weight change we measured for the SiO_x layer was only ~0.2 mg, which introduces some measurement uncertainties. Therefore, the effective diffusion coefficient of SiO_x could not be determined accurately using Eq. (2).

3.2. Transient WVTRs and lag times

The mean values of the experimentally measured WVTRs as a function of time are shown in Fig. 4 for multilayer films and in Fig. 5 for the F2F laminate. The steady-state WVTRs and confidence intervals $\Delta\bar{x}$ (confidence level of 95%) and the corresponding Q_{total} values are shown in Table 2.

The permeability coefficients (Q) of the polymer layers (PET, ORM and Adh) were calculated from the P of the sorption measurements (Eq. (3)). Q_{SiO_x1} for the first SiO_x layer (L_2 and L_{10}) was calculated using Eq. (5) for the structures with two and three layers. Although the ORM layer can not significantly reduce the Q_{total} of the 3-layer structure compared to the 2-layer structure, given that $Q_{ORM} \gg Q_{SiO_x}$, the Q_{total} of the 3-layer structure was nevertheless lower. This means that Q_{SiO_x1} in the 3-layer structure must be lower, which shows the synergistic effect of the ORM layer combined with SiO_x, resulting in the barrier improvement of the SiO_x layer [25,26,30].

Given this assumption, the Q_{SiO_x1} of the 3-layer structure was also used for the 4-layer, 5-layer and F2F structures. The Q_{SiO_x2} of the second SiO_x layer (L_4 and L_8) was therefore also calculated using Eq. (5) in these structures. The calculated permeability values for the first and second SiO_x layers were all within the range of values reported in previous studies [31,32].

In our multilayer structures, the permeability of the SiO_x layers coated onto ORM (L_4 and L_8) was about one order of magnitude lower than that of SiO_x coated onto a PET substrate. This difference may reflect the planarization effect of ORM [33] yielding a smooth substrate

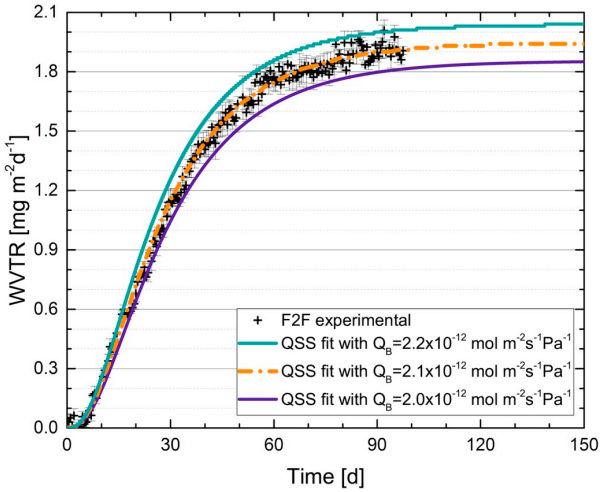

Fig. 5. Experimentally measured WVTR values for the F2F laminate at 38 °C and 36% RH. Data represent three measurements with standard deviations. Lines represent the results of the QSS calculations based on Eq. (8). To show the sensitivity of the steady-state WVTR and the lag time for $Q_{\mathbf{B}}$, this parameter was varied by 0.1 mol $m^{-2}s^{-1}Pa^{-1}$.

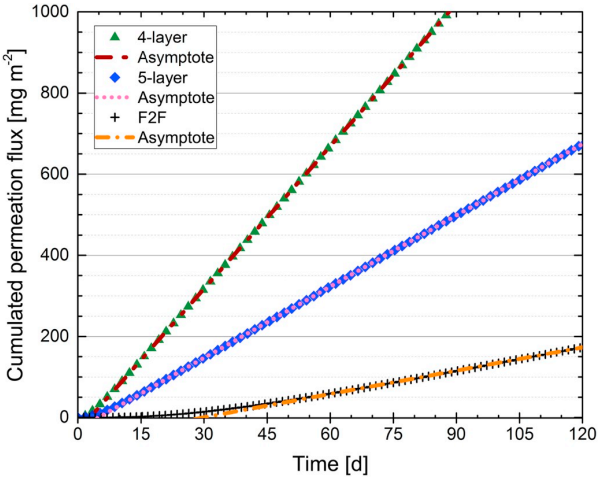

Fig. 6. Cumulative flux, i.e. total permeated mass per unit area, through barrier films as a function of time. The steady-state slope of the asymptote (lines) corresponds to the WVTR, and the intersection with the time axis shows the lag time.

for the second SiO_x layer and thus resulting in lower Q values (Q_{SiO_x2}). The Q_{SiO_x2} value in the 5-layer structure was lower than in the 4-layer structure again caused by the synergistic effect of the ORM layer an top of the second SiO_x coating [25,26,30].

The cumulative permeation fluxes, showing the amount of water vapor that permeated through the barrier films, with asymptotes to the steady-state regions and extrapolation to the time axis, are shown in Fig. 6. The lag times calculated from the experimental measurements using Eq. (6) for each type of multilayer structure are shown in Table 2. Neither a single inorganic SiO_x barrier layer deposited on a PET substrate (2-layer structure), nor a single polymer ORM layer coated onto the SiO_x layer on PET (3-layer structure) had a significant effect on the increase in the lag times. Only when a second SiO_x barrier layer was applied on top of the ORM layer, resulting in the so-called "**BPB**" sequence, did the lag time increase by a factor of five, from ~0.6 d to 3 d. Similarly, the lag time calculated for the F2F laminate structure was higher by a factor of 50, compared to PET, 2- and 3-layer structures (Fig. 1). The presence of the **BPB** sequence within a multilayer structure increases the lag time as predicted based on theory [16].

3.3. QSS approximation

Based on the sorption and WVTR measurements described above, the ratios $P_{\mathbf{P}}/P_{\mathbf{B}}$ and $S_{\mathbf{P}}/S_{\mathbf{B}}$ were found to be much higher than 100 for PET, ORM and Adh as **P**-layers and SiO_x as a **B**-layer. Therefore, the time-dependent behavior of the experimental WVTRs for **BPB**-type and **BPBPBPB**-type structures were calculated using Eq. (7) (4- and 5-layer) or Eq. (8) (F2F laminate).

The calculations included the layer thickness $h_{\mathbf{P}}$ and the solubility coefficient $S_{\mathbf{P}}$ from the sorption measurements (Table 1). A mean value of $h_{\mathbf{P}} \times S_{\mathbf{P}}$ was calculated using Eq. (12) for the polymer layers in the F2F laminate structure, consisting of ORM or ORM/Adh/ORM. The $Q_{\mathbf{B}}$ values were calculated from the steady-state WVTRs using Eq. (9). The results are presented in Table 3 and the calculated QSS curves are shown in Fig. 4 for 4- and 5-layer structures and Fig. 5 for the F2F laminate.

The reported $Q_{\mathbf{B}}$ values for SiO_x are representative values for the overall barrier performance of the first and second SiO_x layers in these structures. As discussed in Section 3.2, the barrier performance of a SiO_x layer can vary based on the roughness of the underlying substrate and also due to the synergistic effect of the additional ORM layer applied on top of the SiO_x [25,26,30]. The QSS approximation uses one characteristic value for all of the SiO_x layers in these multilayer structures.

The lag times of the structures were calculated using Eqs. (10) and (11), and agreed closely with the results obtained by measuring the WVTRs (Table 2), thus validating the QSS approximation approach.

We used the results from sorption measurements and the steady-state WVTRs to calculate the parameters for the QSS approximation. In the case of the F2F laminate structure, it takes a long time to measure a steady-state WVTR. Using the QSS approximation, it is also possible to

Table 2
Steady-state WVTR values (mean values of three measurements) at 38 °C and 36%RH. Confidence intervals $\Delta\bar{x}$ were calculated with a confidence level of 95%. Lag times ϑ were determined using Eq. (6) based on experimental WVTR measurements. The permeability values Q of the polymer layers (PET, ORM and Adh) were calculated from the P of the sorption measurements. Q_{SiO_x1} and Q_{SiO_x2}, for the first and second SiO_x layers, were calculated according to the ideal laminate theory, using Eq. (5).

	WVTR	Q_{total}	Q_{PET}	Q_{SiO_x1}	Q_{ORM}	Q_{SiO_x2}	Q_{Adh}	Lag-time ϑ
	(mg m^{-2} d^{-1})	(mol m^{-2} s^{-1} Pa^{-1})	(mol m^{-2} s^{-1} Pa^{-1})	(mol m^{-2} s^{-1} Pa^{-1})	(mol m^{-2} s^{-1} Pa^{-1})	(mol m^{-2} s^{-1} Pa^{-1})	(mol m^{-2} s^{-1} Pa^{-1})	(d)
PET	4460 ± 140	1.2×10^{-9}	1.2×10^{-9}					0.5 ± 0.4
2-layer	70 ± 6	1.9×10^{-11}	1.2×10^{-9}	1.9×10^{-11}				0.6 ± 0.1
3-layer	58 ± 2	1.6×10^{-11}	1.2×10^{-9}	1.6×10^{-11}	1.7×10^{-7}			0.7 ± 0.6
4-layer	11.7 ± 0.2	3.2×10^{-12}	1.2×10^{-9}	1.6×10^{-11}	1.7×10^{-7}	3.9×10^{-12}		2.9 ± 0.4
5-layer	5.8 ± 0.2	1.6×10^{-12}	1.2×10^{-9}	1.6×10^{-11}	1.7×10^{-7}	1.7×10^{-12}		4.7 ± 0.4
F2F	2.0 ± 0.1	5.4×10^{-13}	1.2×10^{-9}	1.6×10^{-11}	1.7×10^{-7}	1.2×10^{-12}	1.3×10^{-6}	30 ± 2

Table 3
Effective $h_P \times S_P$ of the polymer layers (**P**) in the **BPB** and **BPBPBPB** structures, effective permeability values Q_B (**B** layer) and lag times ϑ, used to calculate the QSS curves shown in Fig. 4.

BPB structure	**P** layer	$h_P \times S_P$ (mol m^{-2}Pa^{-1})	**B** layer	Q_B (mol m^{-2}s^{-1}Pa^{-1})	ϑ (d)
4-layer	ORM (L_3)	3.0×10^{-6}	SiO_x (L_2,L_4)	6.3×10^{-12}	2.8
5-layer	ORM (L_3)	2.8×10^{-6}	SiO_x (L_2,L_4)	3.2×10^{-12}	5.2
F2F	ORM (L_3,L_9) ORM/Adh/ORM (L_5/L_6/L_7)	2.3×10^{-6}	SiO_x (L_2,L_4,L_8,L_{10})	2.1×10^{-12}	32

$Q_B = P_B/h_B$

predict a steady-state permeation value by adjusting the calculated curve to the empirical data. In this case, Q_B is the only unknown parameter in Eqs. (7) and (8), and both the steady-state WVTR and the lag time are highly sensitive to changes in Q_B as shown in Fig. 5 for the F2F structure. Accordingly, the calculated QSS curve can be fitted to the empirical data long before steady-state permeation is reached, and therefore the experimental timeframe can be shortened significantly.

4. Conclusion

The WVTRs of the PET substrate, films with up to five layers, and the F2F laminate with 11 layers, were measured as a function of time using the UPA device at 38 °C and 36% RH to determine the lag times. Based on the empirical data and the calculations performed using the ideal laminate theory, the permeability Q_B of the SiO_x layer is up to five orders of magnitude lower than that of the polymer layers, and has the greatest impact on the steady-state WVTRs. The lag times were longer for the structures with alternating barrier **B** and polymer **P** layers for multilayers incorporating **BPB** triplets. The F2F laminate, which contains a thick polymer layer (ORM/Adh/ORM) with a high solubility coefficient S_P embedded between barrier layers with low permeability coefficients, showed the longest lag time in this study.

The D and S coefficients of the polymer layers in our multilayer structures were determined experimentally in free-standing test specimens by measuring the sorption at 38 °C, and the water vapor permeability coefficients P were calculated as the product of D and S. The permeability of these polymer matrices can be ranked highest to lowest as follows: $P_{Adh} > P_{ORM} > P_{PET}$. The diffusion coefficients can similarly be ranked as $D_{Adh} > D_{PET} > D_{ORM}$, and the solubility coefficients as $S_{ORM} > S_{Adh} > S_{PET}$. Accordingly, the ORM layer has the lowest D and the highest S among the three polymers. The Q_B values for the first and second SiO_x layers of the multilayered structures were calculated using the ideal laminate theory and indicate that the first SiO_x layer is 10 times more permeable than the second. Due to the planarization effect of ORM, providing a smoother surface for inorganic barrier layer deposition, the permeability of SiO_x was lower, when deposited on an ORM layer, as previously reported for fluoropolymer substrates [33].

The so-called QSS approximation equations [16] were used to calculate the transient WVTR curves and lag times of those structures including **BPB** or **BPBPBPB** layer sequences, and the results agreed closely with the experimentally determined values and reports.

Accordingly, the steady-state WVTR of **BPB**-type and **BPBPBPB**-type barrier films was dominated by the Q_B of the **B** layer, whereas the S_P and thickness of the intermediate **P** layers increased the lag time for permeation [17,18]. We have therefore validated the QSS approximation strategy by confirming the performance and lag time of multilayer structures consisting of **BPB** or **BPBPBPB** sequences can be predicted, helping to reduce the experimental timeframe required for permeation measurements without additional numerical simulations. It should now be possible to design multilayer structures according to the lifetime and barrier requirements of the final product.

Acknowledgements

The authors thank DuPont Teijin Films, Amcor Flexibles Kreuzlingen AG, and Fraunhofer ISC for supplying the barrier materials and films used in this study. This work was financially supported in part by the European Union 7th Framework Program under grant agreements 287594 (SUNFLOWER project) and 314068 (TREASORES project).

References

[1] H.-C. Langowski, Permeation of gases and condensable substances through monolayer and multilayer structures, in: O.G. Piringer, A.L. Baner (Eds.), Plastic Packaging - Interactions with Food and Pharmaceuticals, 2nd Edition, Wiley-VCH, Weinheim, 2008, pp. 297–347.
[2] G.L. Robertson, Food Packaging: Principles and Practice, 2nd Edition, CRC Press, Boca Raton, 2006.
[3] J.S. Lewis, M.S. Weaver, Thin-film permeation-barrier technology for flexible organic light-emitting devices, IEEE J. Sel. Top. Quantum Electron. 10 (1) (2004) 45–57, https://doi.org/10.1109/JSTQE.2004.824072.
[4] U. Soo Lee, J. Sik Choi, B. Seob Yang, S. Oh, Y. Jang Kim, M. Sook Oh, J. Heo, H. Joon Kim, Formation of a bilayer of ALD-SiO_2 and sputtered Al_2O_3/ZrO_2 films on polyethylene terephthalate substrates as a moisture barrier, ECS Solid State Lett. 2 (6) (2013) R13–R15, https://doi.org/10.1149/2.004306ssl.
[5] P.E. Burrows, G.L. Graff, M.E. Gross, P.M. Martin, M.K. Shi, M. Hall, E. Mast, C. Bonham, W. Bennett, M.B. Sullivan, Ultra barrier flexible substrates for flat panel displays, Displays 22 (2) (2001) 65–69, https://doi.org/10.1016/S0141-9382(00)00064-0.
[6] G. Nisato, M. Kuilder, P. Bouten, L. Moro, O. Philips, N. Rutherford, Thin film encapsulation for OLEDs: evaluation of multi-layer barriers using the Ca test, SID Symposium Digest of Technical Papers, 34 Wiley Online Library, 2003, pp. 550–553.
[7] D. Spee, J. Rath, R. Schropp, Using hot wire and initiated chemical vapor deposition for gas barrier thin film encapsulation, Thin Solid Films 575 (2015) 67–71, https://doi.org/10.1016/j.tsf.2014.10.029.
[8] J. Affinito, D. Hilliard, A new class of ultra-barrier materials, 47th Annual Technical Conference Proceedings, Society of Vacuum Coaters, 2004, pp. 563–593.
[9] G.L. Graff, R.E. Williford, P.E. Burrows, Mechanisms of vapor permeation through multilayer barrier films: lag time versus equilibrium permeation, J. Appl. Phys. 96 (4) (2004) 1840–1849.
[10] W. Decker, B. Henry, Basic principles of thin film barrier coatings, 45th Annual Technical Conference Proceedings, Society of Vacuum Coaters, 2002, pp. 492–502.
[11] B.M. Henry, A.G. Erlat, C.R.M. Grovenor, C.-S. Deng, G.A.D. Briggs, T. Miyamoto, N. Noguchi, T. Niijima, Y. Tsukahara, The permeation of water vapor through gas barrier films, 44th Annual Technical Conference Proceedings, Society of Vacuum Coaters, 2001, pp. 469–475.
[12] B.M. Henry, A.G. Erlat, C.R.M. Grovenor, G.A.D. Briggs, T. Miyamoto, Y. Tsukahara, Gas permeation studies of metal oxide/polymer composite films, 45th Annual Technical Conference Proceedings, Society of Vacuum Coaters, 2002, pp. 514–518.
[13] G. Garnier, S. Marouani, B. Yrieix, C. Pompeo, M. Chauvois, L. Flandin, Y. Brechet, Interest and durability of multilayers: from model films to complex films, Polym. Adv. Technol. 22 (6) (2011) 847–856.
[14] A. Roberts, B. Henry, A. Sutton, C. Grovenor, G. Briggs, T. Miyamoto, M. Kano, Y. Tsukahara, M. Yanaka, Gas permeation in silicon-oxide/polymer (SiO_x/PET) barrier films: role of the oxide lattice, nano-defects and macro-defects, J. Membr. Sci. 208 (1) (2002) 75–88, https://doi.org/10.1016/S0376-7388(02)00178-3.
[15] R. Ash, R.M. Barrer, D.G. Palmer, Diffusion in multiple laminates, Br. J. Appl. Phys. 16 (6) (1965) 873–884.
[16] O. Miesbauer, Analytische und numerische Berechnungen zur Barrierewirkung von Mehrschichtstrukturen, Ph.D. thesis Technische Universität München, 2017.
[17] B.D. Vogt, H.-J. Lee, V.M. Prabhu, D.M. DeLongchamp, E.K. Lin, W.-l. Wu, S.K. Satija, X-ray and neutron reflectivity measurements of moisture transport through model multilayered barrier films for flexible displays, J. Appl. Phys. 97 (11) (2005) 114509–1–114509–7.
[18] S.-W. Seo, E. Jung, C. Lim, H. Chae, S.M. Cho, Water permeation through organic-inorganic multilayer thin films, Thin Solid Films 520 (21) (2012) 6690–6694.
[19] S. Kiese, E. Kücükpinar, M. Reinelt, O. Miesbauer, J. Ewender, H.-C. Langowski, A systematic approach for the accurate and rapid measurement of water vapor transmission through ultra-high barrier films, Rev. Sci. Instrum. 88 (2) (2017) 025108.1–025108.7, https://doi.org/10.1063/1.4974952.
[20] S. Amberg-Schwab, K. Noller, U. Weber, O. Miesbauer, Hochbarrierenverbunde und Verfahren zu ihrer Herstellung, patent WO2010069958-A1, (2010).
[21] P.W. Atkins, J. de Paula, Physikalische Chemie, 5th Edition, Wiley-VCH, Weinheim,

2013.
[22] C.E. Rogers, Permeation of gases and vapours in polymers, in: J. Comyn (Ed.), Polymer Permeability, Chapman & Hall, London, 1985, pp. 11–73.
[23] J. Crank, The Mathematics of Diffusion, Oxford University Press, 1975.
[24] J.G. Wijmans, R.W. Baker, The solution-diffusion model: a review, J. Membr. Sci. 107 (1) (1995) 1–21.
[25] S. Amberg-Schwab, M. Hoffmann, H. Bader, M. Gessler, Inorganic-organic polymers with barrier properties for water vapor, oxygen and flavors, J. Sol-Gel Sci. Technol. 13 (1–3) (1998) 141–146, https://doi.org/10.1023/A:1008628029870.
[26] K.-H. Haas, S. Amberg-Schwab, K. Rose, G. Schottner, Functionalized coatings based on inorganicorganic polymers (ORMOCER®s) and their combination with vapor deposited inorganic thin films, Surf. Coat. Technol. 111 (1) (1999) 72–79, https://doi.org/10.1016/S0257-8972(98)00711-7.
[27] T. Shigetomi, H. Tsuzumi, K. Toi, T. Ito, Sorption and diffusion of water vapor in poly(ethylene terephthalate) film, J. Appl. Polym. Sci. 76 (1) (2000) 67–74.
[28] E. Pons, B. Yrieix, L. Heymans, F. Dubelley, E. Planes, Permeation of water vapor through high performance laminates for VIPs and physical characterization of sorption and diffusion phenomena, Energy and Buildings 85 (2014) 604–616, https://doi.org/10.1016/j.enbuild.2014.08.032.
[29] M.M. Schmidt, High Barrier Materials for Flexible and Transparent Encapsulation of Organic Electronics, Ph.D. thesis Technische Universität München, 2013.
[30] S. Amberg-Schwab, Inorganic-organic polymers with barrier properties against water vapor, oxygen and migrating monomers, in: S. Sakka (Ed.), Handbook of Sol-Gel Science and Technology - Volume III: Applications of Sol-Gel Technology, Kluwer, Dordrecht, 2005, pp. 455–478.
[31] K. Kessler, O_2- und H_2O-Permeation Durch SiO_x-Beschichtete PET-Folien, Ph.D. thesis ETH Zürich, 1994.
[32] Y.G. Tropsha, N.G. Harvey, Activated rate theory treatment of oxygen and water transport through silicon oxide/poly(ethylene terephthalate) composite barrier structures, J. Phys. Chem. B 101 (13) (1997) 2259–2266, https://doi.org/10.1021/jp9629856.
[33] J. Fahlteich, C. Steiner, N. Schiller, O. Miesbauer, K. Noller, K.-J. Deichmann, M. Mirza, S. Amberg-Schwab, Roll-to-roll thin film coating on fluoropolymer webs: status, challenges and applications, Surface and Coatings Technology 314 (Supplement C), 2017, pp. 160–168 selected papers from the Society of Vacuum Coaters 59th Annual Technical Conference. doi https://doi.org/10.1016/j.surfcoat.2016.11.106.

4.3 The influence of temperature on the intrinsic transport properties of water in inorganic and polymeric coatings [3]

Summary

One way to accelerate the experimental permeation measurements is to increase the measurement temperature. However, the use of different climate conditions makes it difficult to compare the results of different research groups. Therefore, approximations were developed for films with at least one **BPB**-triplet using a combination of QSS approximation and Arrhenius' laws, which allow the transient permeabilities to be calculated for any other climatic condition after measurement at one temperature and humidity. Again, films with up to 11 alternating inorganic SiO_x and polymeric layers were characterized. The water vapor permeability, solubility and diffusivity of each layer based on measurements of water absorption, transient water vapor permeation and lag times were measured at different temperatures and relative humidities.

The activation energy of water vapor permeation in PET/SiO_x films was $5.7\,\mathrm{kJ\,mol^{-1}}$, which is about twice as high as the value of the PET substrate. Accordingly, the interactions between water and SiO_x have an influence on the permeation mechanism of the two-layer structure. The ORM layer leads to a small reduction in WVTR, most likely by filling the nanoscale defects in the first SiO_x layer and providing a smooth surface for the second SiO_x layer in **BPB** and **BPBPBPB** structures. Furthermore, an ORM coating on top of the SiO_x layers in both of the multilayer structures (**BPB** and **BPBPBPB**) reduced the value of the pre-exponential factor for the permeation coefficient of the **B**-layer $P_{0_\mathbf{B}}$, which also gives an indication of the possible filling of the nanoscale defects. However, ORM did not change the activation energy and accordingly, its effect on the water vapor permeation mechanisms in the SiO_x structure itself seems to be negligible. The calculation under the assumption that the activation energy for the first and second SiO_x layers did not change due to coating with ORM, gave results which were in agreement with experimental values.

[3] Kiese S., Kücükpinar E., Miesbauer O., and Langowski H.-C., The influence of temperature on the intrinsic transport properties of water in inorganic and polymeric coatings, *Thin Solid Films* **717**, 138476 (2021).

The equations derived by combining the QSS approach and Arrhenius' law revealed the temperature and pressure dependencies of steady-state WVTR and lag time in multilayer structures comprising **BPB** triplets, and the results agreed closely with the experimentally determined values. Accordingly, the WVTR-increase with temperature is dominated by the increase of the total partial pressure difference, if the gradient of relative humidity is constant, whereas the lag time is mainly influenced by the heat of sorption of the polymeric layer.

Thus, the experimentally determined material-specific parameters allow to predict the influence of temperature and RH on the barrier performance of multilayered barrier structures. These results enable the design of multilayer barrier films according to the lifetime requirements of sensitive devices and the effect of environmental conditions on the barrier performance can be estimated more accurately.

Author contributions:

- Sandra Kiese: corresponding author, conceptualization, data curation, formal analysis, investigation, methodology, validation, visualization, writing original draft
- Esra Kücükpinar: conceptualization, funding acquisition, supervision, writing - review & editing
- Oliver Miesbauer: methodology, supervision, validation, writing - review & editing
- Horst-Christian Langowski: supervision, writing - review & editing

Thin Solid Films 717 (2021) 138476

Contents lists available at ScienceDirect

Thin Solid Films

journal homepage: www.elsevier.com/locate/tsf

The influence of temperature on the intrinsic transport properties of water in inorganic and polymeric coatings

Sandra Kiese [a,b,*], Esra Kücükpinar [b], Oliver Miesbauer [a], Horst-Christian Langowski [a,b]

[a] Technical University of Munich, TUM School of Life Sciences Weihenstephan, Chair of Food Packaging Technology, Weihenstephaner Steig 22, Freising, 85354, Germany

[b] Fraunhofer Institute for Process Engineering and Packaging IVV, Giggenhauser Str. 35, Freising, 85354, Germany

ARTICLE INFO

Keywords:
Water vapor permeation
Sorption
Diffusion
Temperature dependency
Theroretical approximations

ABSTRACT

Barrier layers are often used to protect sensitive organic devices from the detrimental effects of oxygen and water vapor. We investigated the effect of temperature on the time-dependent behavior of water vapor permeation in multilayer barrier films, focusing on the water vapor solubility, diffusion and permeability coefficients of individual layers and layer sequences. Activation energy measurements helped to explain the permeation mechanisms and showed the possible interactions between water and silicon oxide (SiO_x). The activation energy for permeation (E_P) through a two-layer film of polyethylene terephthalate (PET) coated with SiO_x was 5.7 $kJmol^{-1}$, about twice the E_P value of the uncoated PET substrate. An intermediate ORMOCER® layer, providing a smooth surface for a second SiO_x layer in an alternating structure, had only a negligible effect on the E_P. Temperature dependent quasi-stationary approximations were derived for permeation through films with at least one inorganic/polymer/inorganic triplet, and were validated according to experimentally determined values. These equations showed the temperature and pressure dependencies of steady-state permeation and lag time in multilayered structures. Accordingly, the temperature dependency of steady-state permeation is determined by the E_P of SiO_x, whereas the lag time was mainly influenced by the heat of sorption of the intermediate polymeric layer. Furthermore, the increase in water vapor transmission rate was dominated by the partial pressure change with increasing temperature. Using these equations and experimentally determined parameters, we can predict the influence of temperature and humidity on the barrier performance of multilayered barrier structures.

1. Introduction

Flexible organic electronic devices such as organic photovoltaics and organic light emitting diodes aim to replace energy-demanding and expensive silicon technology with flexible, lightweight and inexpensive devices produced by roll-to-roll processes [1,2]. However, the electrical properties of such devices degrade significantly over time due to the sensitivity of the organic materials to the presence of water and oxygen in ambient air [3,4]. Many research groups have attempted to overcome this limitation by developing flexible encapsulation films with high gas and vapor barrier properties, often involving the deposition of alternating dyads of inorganic barriers (**B**), such as silicon oxide (SiO_x), silicon nitride or aluminum oxide, and polymeric intermediate layers (**P**) on polymeric substrate films [5–17].

Permeation through vacuum-deposited thin inorganic barrier layers can be described using several mathematical models. For water vapor permeation through barrier films comprising alternating polymer and high-quality (but still nanoporous) inorganic barrier layers, the ideal laminate model is the method preferred in the literature [18–23]. This model assumes that a significant amount of the water is dissolved in the inorganic material and permeates through quasi-homogeneously distributed nanoscale defects (<1 nm), leading to a significant contribution of these defects to water vapor permeation [23–25]. The inorganic and polymeric layers are therefore considered to be homogeneous, and the barrier to water vapor permeation in a multilayered structure is similar to an electrical series resistance. According to the ideal laminate theory, the steady-state water vapor permeation of a multi-layer structure, Q_{total}, can be calculated as

$$\frac{1}{Q_{total}} = \sum_{i=1}^{n} \frac{1}{Q_i}, \quad (1)$$

* Corresponding author.
E-mail address: sandra.kiese@ivv.fraunhofer.de (S. Kiese).

https://doi.org/10.1016/j.tsf.2020.138476
Received 24 March 2020; Received in revised form 23 November 2020; Accepted 1 December 2020
Available online 6 December 2020
0040-6090/

based on the permeability values (Q_i) of the individual layers [5].

In this article, the water vapor transmission rate (WVTR) pertains to the time-dependent (mass) flux density $j(t)$, which is calculated from the permeability Q and the boundary partial pressure p as shown in Eq. 2:

$$j = Q \times p. \tag{2}$$

Q is related to the permeability coefficient P, which is the product of the solubility S and diffusion D coefficients [5,26,27], as shown in Eq. 3:

$$P = Q \times h, \tag{3}$$

where h is the layer thickness.

The water vapor P, S and D coefficients of each layer material in the barrier film depend on the temperature T. Several previous reports have proposed that the transport of water vapor through barrier films is a thermally activated process [28–31]. Accordingly, the activation energies for permeation E_P and diffusion E_D, and the heat of sorption ΔH_S, are obtained by applying Arrhenius' [26,32] and van't Hoff's [33] laws as shown in Eqs. 4,5,6:

$$P(T) = P_0 \cdot exp\left(\frac{-E_P}{RT}\right), \tag{4}$$

$$D(T) = D_0 \cdot exp\left(\frac{-E_D}{RT}\right) \tag{5}$$

and

$$S(T) = S_0 \cdot exp\left(\frac{-\Delta H_S}{RT}\right). \tag{6}$$

The factors P_0, D_0 and S_0 represent the limit values for $T \rightarrow \infty$ and R ist the ideal gas constant. The activation energy of the permeation process E_P is defined by the sum of the heat of ΔH_S and E_D, as shown in Eq. 7:

$$E_P = \Delta H_S + E_D. \tag{7}$$

If the WVTRs are measured at a constant relative humidity, but at various temperatures, as is often the case in the literature, the activation energy additionally includes a contribution of the enthalpy of vaporization ΔH_V, which reflects the dependence of the partial pressure on temperature. In a sufficiently small temperature range, where ΔH_V can be considered as a constant, the water vapor pressure p is given by the van't Hoff's equation [33] as

$$p = p_0 \cdot exp\left(\frac{-\Delta H_V}{RT}\right). \tag{8}$$

Consequently, $j(t)$ as a function of the temperature can be expressed as

$$j(t,T) = \frac{P \cdot p}{h} = \frac{P_0 p_0}{h} \cdot exp\left(\frac{-(E_P + \Delta H_V)}{RT}\right). \tag{9}$$

The contribution of ΔH_V can be removed to focus solely on the direct effect of temperature on the permeation process by measuring the WVTR at the same partial pressure, as we did during our measurements, or by normalizing the WVTR values to the different partial pressures applied. This leads to reported E_P values of 3.2 ± 1.0 kJmol^{-1} for water vapor in PET [28,34–36]. Our reported results on activation energies in this publication do not include the contribution of ΔH_V.

The deposition of an inorganic layer on top of a polymeric substrate film may cause the E_P value to increase significantly, providing an indication of the underlying permeation mechanism. According to literature, the temperature dependencies of a multilayered structure differ from those of the substrate film if there is a significant contribution of nanoscale defects (<1 nm) to permeation [25,29] and capillary condensation, Fick's diffusion and interfacial diffusion are the predominant mechanisms for water vapor transport through the layers. On the contrary, if there is no interaction between the layer material and the permeate, we have free diffusion or membrane flow, and consequently the temperature dependency of the permeation through the substrate does not change after coating. By measuring the temperature dependency of the permeation through a layered system, it is therefore possible to determine the permeation mechanisms [5,31,37,38]. For water vapor permeation in SiO_x layers deposited on PET, this result was confirmed by Roberts et al. [25].

Several different polymeric substrates coated with a SiO_x layer by plasma-enhanced chemical vapor deposition reached an E_P of 10.3 ± 8 kJmol^{-1} [29,34,39]. This value being a factor of at least three times higher than that of the polymeric substrates gives an indication that the permeation mechanism of water vapor within the inorganic barrier layer differs in comparison to its substrate. It has been already shown that the nanoscale defects of the inorganic layer have a significant contribution to permeation of water vapor, due to the chemical and physical interaction between water and the oxide [29,34,39]. The size and the number of the nanoscale defects affect the E_P depending on the substrate roughness, deposition process, and the type of the coating material.

The objective of this research was to determine and compare the theoretical and experimental time dependent WVTRs for polymeric substrates coated with inorganic and polymeric layers, as a function of temperature. We focused on the effects of the water vapor S and P of individual layers and layer sequences on both the WVTR values and lag times of multilayered structures.

2. Materials and methods

2.1. Production of film samples for WVTR measurements and sorption analysis

We measured the WVTR and solubility characteristics of the single-layer and multilayer films shown in Table 1. The polymeric substrate film was a PET Melinex® 401 CW (50 m thick) from DuPont Teijin Films (United Kingdom), coated by AMCOR Flexibles Kreuzlingen (Switzerland) according to the Fraunhofer POLO® concept [40] with electron beam evaporated SiO_x (100nm thick) using a stoichiometric factor x of 1.7 to 1.8 [41]. The organic-inorganic hybrid polymeric coating was an ORMOCER® (ORM) layer, which is synthesized by Fraunhofer ISC (Germany) using a sol-gel process, and is applied in the liquid phase with a thickness of 1.8 ± 0.6 m by a continuous roll-to-roll reverse gravure process at Fraunhofer IVV (Germany) before the deposition of a second inorganic SiO_x layer. A second layer of ORM was applied on top to protect the surface from mechanical damage during the lamination process. A so-called face-to-face laminate (**BPBPBPB**) was then produced by the adhesive lamination of two **BPB** structures. The lamination adhesive (Adh) was a two-component polyurethane resin (Novacote Flexpack Division, Coim Deutschland, Germany) applied at a thickness of 1.6 ± 0.4 m by reverse gravure at Fraunhofer IVV (drying temperature = 60 °C).

The ORM single-layer samples were produced by doctor blading on an untreated polypropylene film using a CUF 5 semi-automatic coating unit (Sumet Messtechnik, Germany). The coatings were applied using a K-bar (K-1.4) to achieve a dry coating thickness of ~55 m. Hot air was used to dry the ORM at 120 °C. Given the weak adhesion of the coatings to the polypropylene substrate, the ORM could be removed easily and its WVTR and sorption behavior was therefore measured as free-standing samples.

2.2. WVTR and sorption measurements

The WVTR of the PET and ORM samples was measured using the gravimetric method according to the standard DIN 53122-1. Samples with an area of 5 cm^2 were clamped in metal screw shells and stored under defined climatic conditions. The weight changes over time were fitted linearly and the slope represents the WVTR. The lower detection limit of this method is 0.5 gm^{-2}d^{-1} [42]. Films with lower WVTRs,

Table 1
Barrier film structures used in this study. L_i is the layer number.

Structure Code	L_1	L_2	L_3	L_4	L_5	L_6	L_7	L_8	L_9	L_{10}	L_{11}
PET	PET										
ORM	ORM										
Two-layer	PET	SiO_x									
Three-layer	PET	SiO_x	ORM								
BPB	PET	SiO_x	ORM	SiO_x							
BPBPBPB	PET	SiO_x	ORM	SiO_x	ORM	Adh	ORM	SiO_x	ORM	SiO_x	PET

which contain a SiO_x layer, were measured using the ultra-permeation accumulation (UPA) measurement device at Fraunhofer IVV, with a detection limit of 2×10^{-5} $gm^{-2}d^{-1}$. This device and the measurement procedure have been described in detail elsewhere [43]. The RH during the measurements was kept constant at 28 % and the temperature was set to 25, 30, 35 or 40 °C. Accordingly, the partial pressure of the water vapor varied with the temperature (885, 1185, 1572 or 2063 Pa, respectively).

The water vapor sorption behavior of the polymer samples was measured gravimetrically with a resolution of ± 20μg, using a SPSx-1μ micro balance (ProUmid, Germany). This test system automatically determines the sorption isotherms of the sample materials. For these measurements, three specimens from each sample type were placed in 12ml aluminum cups and exposed to temperatures of 25, 30, 35 or 40 °C in the sample chamber. The RH was increased from 0 % to 50 % in steps of 10 % and the moisture uptake was recorded until a weight change of 0.01 % within 15 min was observed at each stage, which we considered to represent steady-state conditions. Where we observed a linear dependency of the water concentration on the partial water vapor pressure within the experimental temperature and humidity ranges, the effective S were calculated according to Henry's law [26,33] as shown in Eq. 10:

$$c = S \times p, \tag{10}$$

where c is the equilibrium concentration of water in the layer material.

When the initial concentration of water in the sample is zero, D of a plane sheet of a material can be estimated from the time-dependent sorption behavior [44] as shown in Eq. 11:

$$D = \frac{\pi h^2}{64 t_{1/2}}, \tag{11}$$

where h is the sample thickness and $t_{1/2}$ is the time needed for the sorption process to achieve half of the steady-state mass uptake.

2.3. *Quasi-steady-state approximation for **BPB** and **BPBPBPB** multilayer films*

The numerical calculations for transient permeation through multilayered structures consisting of at least one **BPB** triplet (comparable to the structures studied in this article) have been reported elsewhere [45,46]. For the benefit of the reader, the most important results are summarized here briefly. The calculations are based on the ideal laminate model, assuming that Henry's (Eq. 10) and Fick's law (Eq. 12) apply in each layer:

$$j = -D\frac{\partial c}{\partial x}, \tag{12}$$

where x is the position within the layer [21,26,44].

In order to generate a partial pressure gradient, a constant partial pressure was applied on one surface of the structure, whereas the partial pressure on the other surface and the initial concentration within the structure were set to zero. The numerical simulations show that the partial pressure profile is almost linear within each layer during the whole permeation process, besides a small time period at the beginning. Furthermore, the position dependence of the partial pressure within the **P** layers can be neglected. Based on these observations, Miesbauer [45,46] developed a quasi-steady-state (QSS) approach for the time-dependent permeation through structures of alternating layers. A mass balance is established for each **P** layer in the structure, which relates the change of the partial pressure for this layer with time to the fluxes through the adjacent **B** layers. Based on the calculated linear partial pressure profiles, these fluxes were assumed to correspond to steady-state permeation at each time, caused by the current values of the partial pressures in the considered and the surrounding **P** layers. According to the general theory, the solution of the resulting system of linear differential equations can be represented in terms of eigenvalues and eigenvectors of its coefficient matrix [47,48]. The time-dependent flux density at that surface, where the partial pressure is zero, is derived from this solution. The most simple solution is obtained for a structure where each **B** layer is characterized by the same permeability coefficient $P_\mathbf{B}$ and thickness $h_\mathbf{B}$ and each **P** layer by the same solubility coefficient $S_\mathbf{P}$ and thickness $h_\mathbf{P}$. For a **BPB** structure the resulting flux density $j(t)$ is given as [45]:

$$j(t) = \frac{P_\mathbf{B} p}{2h_\mathbf{B}}\left(1 - \exp\left(-\frac{2P_\mathbf{B}}{h_\mathbf{B} h_\mathbf{P} S_\mathbf{P}} t\right)\right), \tag{13}$$

if $S_\mathbf{P} \gg S_\mathbf{B}$ [46,49,50], where $P_\mathbf{B}$ is the permeability coefficient, $S_\mathbf{B}$ is the solubility coefficient, and $h_\mathbf{B}$ is the thickness of each **B** layer, $S_\mathbf{P}$ is the solubility coefficient, and $h_\mathbf{P}$ is the thickness of the **P** layer.

For **BPBPBPB** structures, the time-dependent flux density can be approximated as shown in Eq. 14 [45]:

$$\begin{aligned} j(t) \quad = & \frac{P_\mathbf{B} p}{4h_\mathbf{B}}\left(1 - \left(\frac{1}{\sqrt{2}} + 1\right)\exp\left(\left(\sqrt{2} - 2\right)\frac{P_\mathbf{B}}{h_\mathbf{B} h_\mathbf{P} S_\mathbf{P}} t\right)\right. \\ & + \exp\left(-2\frac{P_\mathbf{B}}{h_\mathbf{B} h_\mathbf{P} S_\mathbf{P}} t\right) \\ & \left. + \left(\frac{1}{\sqrt{2}} - 1\right)\exp\left(\left(-\sqrt{2} - 2\right)\frac{P_\mathbf{B}}{h_\mathbf{B} h_\mathbf{P} S_\mathbf{P}} t\right)\right) \end{aligned} \tag{14}$$

The steady-state WVTR values are equal to the asymptotic values of Eqs. 13 and 14 for large values of t, as shown in Eq. 15

$$j_{\text{steady}} = \frac{P_\mathbf{B} p}{N_\mathbf{B} h_\mathbf{B}}, \tag{15}$$

where $N_\mathbf{B}$ is the number of **B** layers.

The lag time ϑ of the multilayer structures, which is used to characterize the manner in which $j(t)$ approaches a steady-state value, is defined by the amount $n(t)$ of water vapor that has permeated through a film sample of unit area within a sufficiently long time period as given by

$$n(t) \approx j_{\text{steady}} \times (t - \vartheta). \tag{16}$$

It can be calculated as shown in Eq. 17 for **BPB** type structures:

$$\vartheta = \frac{h_\mathbf{B} h_\mathbf{P} S_\mathbf{P}}{2P_\mathbf{B}} \tag{17}$$

and as shown in Eq. 18 for **BPBPBPB** type structures:

$$\vartheta = \frac{5h_{\mathbf{B}}h_{\mathbf{P}}S_{\mathbf{P}}}{2P_{\mathbf{B}}}, \tag{18}$$

in each case based on Eqs. 13 and 14, as previously reported [45].

In this study, $P_{\mathbf{B}}$ and $S_{\mathbf{P}}$ are defined as the effective coefficients of the inorganic (**B**) and polymeric (**P**) layers, respectively, in a multilayer structure. They can differ from the corresponding coefficients for a separate layer, depending on the underlying substrate material and potential synergistic effects between adjacent layers in multilayer structures, especially for SiO_x in combination with ORM layers [46, 51–53]. The QSS approximation uses one characteristic value for all of the SiO_x layers in these multilayer structures.

As theoretical considerations have previously shown [45,46], the remaining outer PET substrate layer, which is not enclosed between two **B** layers, does not significantly contribute to the barrier performance of the multilayer film and was therefore disregarded for all QSS calculations. Accordingly, the measurement of $P_{\mathbf{B}}$, $S_{\mathbf{P}}$, $h_{\mathbf{B}}$ and $h_{\mathbf{P}}$ was sufficient to predict the time-dependent permeation of water vapor through multilayer barrier films with **BPB** or **BPBPBPB** structures.

3. Results and discussion

3.1. Temperature-dependent quasi-steady-state approximation

As discussed above, Arrhenius's laws can be used to describe the temperature dependency of water vapor sorption in, and permeation through, multilayer films. To predict the temperature-dependent permeation through **BPB** and **BPBPBPB** structures, we substituted $P_{\mathbf{B}}$ and $S_{\mathbf{P}}$ in Eq. 13 and 14 with Eq. 4 and 6, resulting in Eq. 19 for **BPB** structures:

$$j(t,T) = \frac{P_{0_{\mathbf{B}}}p}{2h_{\mathbf{B}}}\exp\left(\frac{-E_{P_{\mathbf{B}}}}{RT}\right)\left(1-\exp\left(-\frac{2P_{0_{\mathbf{B}}}}{h_{\mathbf{B}}h_{\mathbf{P}}S_{0_{\mathbf{P}}}}\exp\left(\frac{\Delta H_{S_{\mathbf{P}}}-E_{P_{\mathbf{B}}}}{RT}\right)t\right)\right) \tag{19}$$

and Eq. 20 for **BPBPBPB** structures:

$$\begin{aligned} j(t,T) \quad &= \frac{P_{0_{\mathbf{B}}}p}{4h_{\mathbf{B}}}\exp\left(\frac{-E_{P_{\mathbf{B}}}}{RT}\right) \\ &\cdot\left(1-\left(\frac{1}{\sqrt{2}}+1\right)\exp\left((\sqrt{2}-2)\frac{P_{0_{\mathbf{B}}}}{h_{\mathbf{B}}h_{\mathbf{P}}S_{0_{\mathbf{P}}}}\exp\left(\frac{\Delta H_{S_{\mathbf{P}}}-E_{P_{\mathbf{B}}}}{RT}\right)t\right)\right. \\ &+\exp\left(-2\frac{P_{0_{\mathbf{B}}}}{h_{\mathbf{B}}h_{\mathbf{P}}S_{0_{\mathbf{P}}}}\exp\left(\frac{\Delta H_{S_{\mathbf{P}}}-E_{P_{\mathbf{B}}}}{RT}\right)t\right) \\ &\left.+\left(\frac{1}{\sqrt{2}}-1\right)\exp\left((-\sqrt{2}-2)\frac{P_{0_{\mathbf{B}}}}{h_{\mathbf{B}}h_{\mathbf{P}}S_{0_{\mathbf{P}}}}\exp\left(\frac{\Delta H_{S_{\mathbf{P}}}-E_{P_{\mathbf{B}}}}{RT}\right)t\right)\right). \end{aligned} \tag{20}$$

Like Eq. 15, the steady-state WVTR values are the asymptotic values of Eq. 19 and 20 for large values of t, as shown in Eq. 21:

$$j_{\text{steady}}(T) = \frac{P_{0_{\mathbf{B}}}p}{N_{\mathbf{B}}h_{\mathbf{B}}}\exp\left(\frac{-E_{P_{\mathbf{B}}}}{RT}\right). \tag{21}$$

The temperature-dependent lag times are calculated as shown in Eq. 22 for **BPB** structures:

$$\vartheta(T) = \frac{h_{\mathbf{B}}h_{\mathbf{P}}S_{0_{\mathbf{P}}}}{2P_{0_{\mathbf{B}}}}\exp\left(\frac{E_{P_{\mathbf{B}}}-\Delta H_{S_{\mathbf{P}}}}{RT}\right) \tag{22}$$

and as shown in Eq. 23 for **BPBPBPB** structures with more than one **BPB** triplet:

$$\vartheta(T) = \frac{5h_{\mathbf{B}}h_{\mathbf{P}}S_{0_{\mathbf{P}}}}{2P_{0_{\mathbf{B}}}}\exp\left(\frac{E_{P_{\mathbf{B}}}-\Delta H_{S_{\mathbf{P}}}}{RT}\right), \tag{23}$$

derived from Eq. 19 and 20.

According to these equations, the temperature dependency of the steady-state WVTR is only determined by the **B** layers Eq. 21) and the temperature dependency of the lag time is influenced by the E_P of the **B** layers and the ΔH_S of the **P** layers (Eq. 22 and (23) for both types of multilayered structures.

In order to predict the temperature-dependent permeation through **BPB** and **BPBPBPB** structures using Eq. 19 and 20, the parameters $E_{P_{\mathbf{B}}}$, $\Delta H_{S_{\mathbf{P}}}$, $P_{0_{\mathbf{B}}}$, $S_{0_{\mathbf{P}}}$, $h_{\mathbf{B}}$ and $h_{\mathbf{P}}$ must be determined. The measurement results for the ORM and SiO_x layers are discussed below.

The laminate structure (**BPBPBPB**) included different types of **P** layers. In order to apply the approximate QSS solution (Eq. 20) to the laminate structure, mean values for each **P** layer were assigned as shown in Eq. 24 and 25:

$$S_{0_{\mathbf{P}}} = \frac{\sum_{i=1}^{n} h_i S_i}{h_{\mathbf{P}}N_{\mathbf{P}}}, \tag{24}$$

$$\Delta H_{S_{\mathbf{P}}} = \frac{\sum_{i=1}^{n} h_i \Delta H_i}{h_{\mathbf{P}}N_{\mathbf{P}}}. \tag{25}$$

3.2. Solubility coefficient S and heat of sorption ΔH_S, diffusion coefficient D and activation energy of diffusion E_D

The measured sorption isotherms of the PET and ORM layers are shown in Figs. 1 and 2. PET showed a linear relationship between the absorbed water concentration and water vapor partial pressure, and the S value was calculated according to Eq. 10. ORM showed a non-linear relationship, with a decreasing slope at high partial pressures. One possible explanation for this is sorption of water at certain sites in the hybrid polymer or, at high pressures, in cavities of glassy polymers. When these sorption sites are almost all occupied, the slope decreases and a smaller amount of permeate dissolves in the polymer. This case occurs when certain gases and vapors are adsorbed in heterogeneous media consisting of a polymer and an inorganic phase [26]. As shown in Fig. 2, the Langmuir isotherm is in agreement with our measurement data, which is an indication that this solution model may apply to the ORM. Nevertheless, at low partial pressures up to 28 %RH a linear relationship could be approximated and S was therefore calculated using Eq. 10 for this material, too. The D were calculated according to Eq. 11 based on the time-dependent sorption of water in the polymer materials, assuming linear sorption behavior. The resulting values are shown in Table 2. The S and D values for PET and ORM are in agreement with earlier publications [54–56].

The experimentally determined D values increased as a function of temperature for both PET and ORM, the activation energy (E_D) being

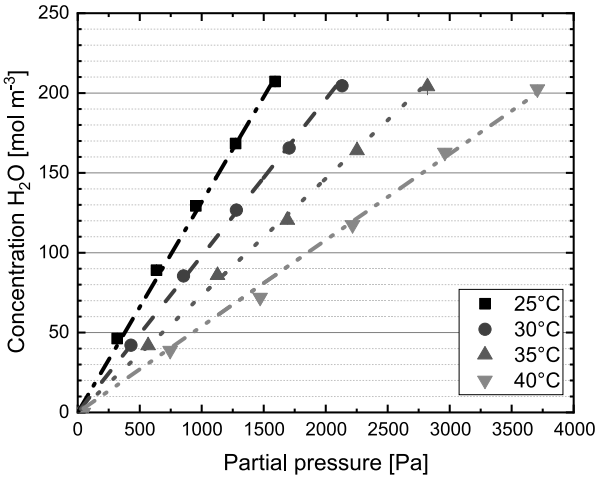

Fig. 1. Sorption isotherms and Henry fits of the PET layer measured at four different temperatures.

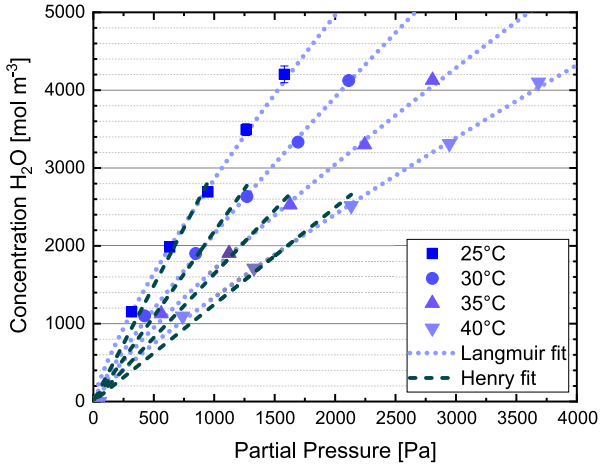

Fig. 2. Sorption isotherm of the ORM layer measured at four different temperatures.

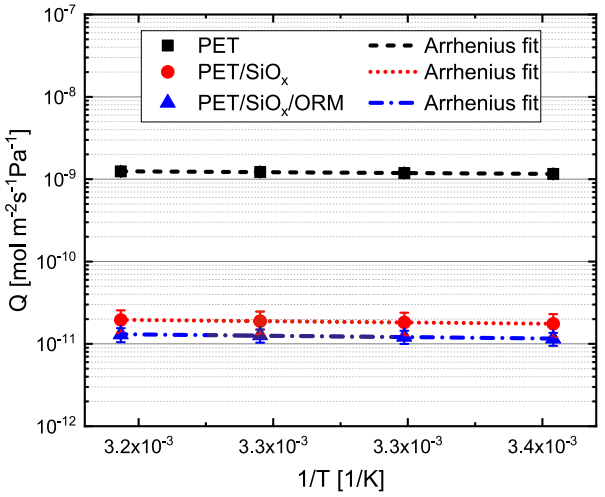

Fig. 3. Permeability Q of PET, two-layer (PET/SiO_x) and three-layer (PET/SiO_x/ORM) films as a function of the inverse temperature. All values are given as mean values of five samples with confidence intervals (confidence level of 95 %).

higher for ORM than PET. This shows the greater temperature sensitivity of PET compared to ORM. The higher mobility of the polymeric chains of PET compared to ORM leads to higher D values, which are more easily affected by temperature variations in comparison to ORM [26,44].

In contrast, the experimentally determined S values decreased with increasing temperature. The S value for ORM was ~20-fold higher than that of PET, reflecting the higher hydrohilicity of ORM [26,57]. The ORM structure has silanol groups that bind water molecules via hydrogen bonds [51,58]. The dependency of S on temperature change was similar for both materials, as represented by ΔH_{S_P}, with values of –46.4 and –45.7 kJmol^{-1} for PET and ORM, respectively.

3.3. Permeability coefficients and E_P

The effect of temperature on the permeability Q of PET, PET/SiO_x and PET/SiO_x/ORM films is compared in Fig. 3. The E_P of PET was found to be 2.8 ± 0.2 kJmol^{-1}. Calculating this value with Eq. 7 using the values given in Table 2 leads to an E_P of 2.5 ± 0.2 kJmol^{-1}. This slight deviation is due to uncertainties in the determination of D, which is why the value of 2.8 ± 0.2 kJmol^{-1}, determined directly from the WVTR measurements, is more reliable.

The apparent activation energy of permeation increased from 2.8 ± 0.2 to 5.7 ± 1.3 kJmol^{-1} for the two-layer structure PET/SiO_x. The permeation through the nanoscale defects in the SiO_x layer is suggested as being the dominant mechanism leading to this increase, which is also attributed to the chemical interactions between the water vapor and SiO_x by several authors [29,34,39]. An ORM layer on top of SiO_x slightly reduced the permeation, probably by limiting the number and size of the nanoscale defects in the SiO_x layer, but its effect on the activation energy, which was 6.7 ± 1.1 kJmol^{-1} for the 3-layer structure, is considered as negligible.

Table 2
Solubility S and diffusion D coefficients of the P materials PET and ORM and corresponding values for heat of sorption ΔH_S (calculated using Eq. 6) and the activation energy of diffusion E_D (calculated using Eq. 5). All values are given as mean values of three samples with confidence intervals (confidence level of 95 %).

Layer	T [°C]	S [mol m^{-3}Pa^{-1}]	ΔH_{S_P} [kJmol^{-1}]	D [m^{2}s^{-1}]	E_D [kJmol^{-1}]
PET	25	$(1.3 \pm 0.1) \times 10^{-1}$	-46.4 ± 0.2	$(4.5 \pm 0.1) \times 10^{-13}$	48.9 ± 0.1
	30	$(9.7 \pm 0.1) \times 10^{-2}$		$(6.2 \pm 0.1) \times 10^{-13}$	
	35	$(7.2 \pm 0.1) \times 10^{-2}$		$(8.5 \pm 0.1) \times 10^{-13}$	
	40	$(5.4 \pm 0.1) \times 10^{-2}$		$(1.2 \pm 0.1) \times 10^{-12}$	
ORM	25	2.8 ± 0.1	-45.7 ± 0.7	$(8.8 \pm 0.1) \times 10^{-14}$	55.1 ± 2.3
	30	2.0 ± 0.1		$(1.2 \pm 0.1) \times 10^{-13}$	
	35	1.5 ± 0.1		$(1.8 \pm 0.1) \times 10^{-13}$	
	40	1.1 ± 0.1		$(2.7 \pm 0.1) \times 10^{-12}$	

3.4. Prediction of time-dependent WVTR in the *BPB* and *BPBPBPB* structures

Using Eq. 19 and our sorption and WVTR measurement results for single-layer (PET and ORM) and three-layer materials at 25, 30, 35 and 40 °C, we predicted the time-dependent WVTR of a **BPB** structure at 38 °C. The parameters used for the calculations are shown in Table 3. As previously reported [46], the ORM layer has a smoother surface than PET leading to a reduction of defects in the SiO_x coating. Accordingly, the permeability coefficient P_B of a SiO_x layer coated on a PET substrate is larger than that of a SiO_x layer coated on an ORM layer [59]. As already shown, P_{0_B} depends on the density of nanoscale defects, which we assumed to be lower in comparison to the two-layer structure, for both SiO_x layers of the **BPB** structure due to the presence of the ORM layer [24,60,61]. E_P depends on the nature of interaction between the layer material and the permeate, which we assume to be the same for both SiO_x layers. Accordingly, we assumed that the P_{0_B} values of both SiO_x layers in the **BPB** structure differed from those in the two-layer film, while E_{P_B} was kept similar for both of the SiO_x layers. Therefore, Eq. 19 uses the same average value of P_{0_B} for both SiO_x layer types, which cannot be measured for the isolated layers. To predict the time-dependent WVTR of a PET/SiO_x/ORM/SiO_x structure at an arbitrary temperature, the steady-state WVTR of this structure must be measured at least at one temperature. At 38 °C and 36 %RH the **BPB** structure had a measured WVTR of 11.8 ± 0.3 m^{-2}d^{-1} (as shown in Fig. 4). Using this value as a starting point, the P_{0_B} in Eq. 19 can be varied until the steady-state WVTR obtained by simulation coincides with the measured value. The results of the calculation using the parameters provided in Table 3 are shown in Fig. 4. For comparison, the experimental WVTR results for this structure are also plotted in the graph as a function of time.

The shape of the calculated curve is in agreement with the experi-

Table 3
Parameters for the calculation of time-dependent WVTRs in **BPB** and **BPBPBPB** structures.

Symbol	Layer	Unit	Measured values for ORM and two-layer structure	Effective values for **BPB** structure	Effective values for **BPBPBPB** structure
S_{0_P}	ORM or	[molm^{-3}Pa^{-1}]	$(2.7 \pm 0.7) \times 10^{-8}$	2.7×10^{-8}	
	Average of individual polymeric layers (Eq. 24)				3.4×10^{-8}
ΔH_{S_P}	ORM or	[kJmol^{-1}]	–45.7 ± 0.7	-45.7	
	Average of individual polymeric layers (Eq. 25)				-44.6
h_P	ORM or	[m]	$(1.8 \pm 0.6) \times 10^{-6}$	1.8×10^{-6}	
	Average of individual polymeric layers				2.9×10^{-6}
P_{0_B}	SiO_x	[molm^{-1}s^{-1}Pa^{-1}]	$(1.8 \pm 0.8) \times 10^{-17}$	6.2×10^{-18}	2.1×10^{-18}
E_{P_B}	SiO_x	[kJmol^{-1}]	5.7 ± 1.3	5.7	5.7
h_B	SiO_x	[m]	$(1.0 \pm 0.1) \times 10^{-7}$	1.0×10^{-7}	1.0×10^{-7}

mental data, indicating that changing the value of P_{0_B} from $(1.8 \pm 0.8) \times 10^{-17}$ molm^{-1}s^{-1}Pa^{-1}, which was measured for the two-layer film structure, to $(6.2 \times 10^{-18}$ molm^{-1}s^{-1}Pa^{-1}, being a fit-value representing the two SiO_x layers of a **BPB** structure, leads to correct results. A possible explanation for this difference between the two P_{0_B} values can be the reduction of nanoscale defects due to the ORM coating on top and below the first and second SiO_x layers of the **BPB**, respectively. However, there is no change in E_{P_B} because the nature of the interaction between water vapor and SiO_x is the same for both SiO_x layers.

The time-dependent WVTR of a **BPBPBPB** structure at 38 °C was predicted in the same manner using Eq. 20 and the parameters provided in Table 3. The calculations included the layer thickness h_P and the solubility coefficient S_{0_P} from the sorption measurements. A mean value was calculated for these parameters using Eqs. 24 and 25 for the polymer layers in the **BPBPBPB** laminate structure, consisting of ORM or ORM/Adh/ORM. The calculated QSS curve is compared to the experimental results in Fig. 5. By adjusting the P_{0_B} value 6.2×10^{-18}molm^{-1}s^{-1}Pa^{-1} (the fit-value of the **BPB** structure) to 2.1×10^{-18} molm^{-1}s^{-1}Pa^{-1}, the calculated curve agreed with the experimental result. The ORM coating on top of the second SiO_x layer again leads to a reduction in P_{0_B} of the **BPBPBPB** structure.

Based on these data, we calculated the time-dependent WVTR of **BPB** and **BPBPBPB** structures within the temperature range 25 to 40 °C at constant boundary partial pressure p of 1138 Pa (Figs. 6 and 7). A second calculation was carried out for a constant RH of 36 % (Fig. 8 and 9) within the same temperature range. Accordingly, the partial pressure increased from 1138 to 2652 Pa in line with this temperature change.

The effect of temperature on the steady-state WVTR was small (asymptotic values for large values of t in Figs. 6 and 7) compared to the linear dependency on p, according to Eq. 21 (Figs. 8 and 9). In contrast to a single polymeric layer, where the lag time ϑ only depends on D and h [44,62], the effect of temperature on lag time in the **BPB** structure was mainly influenced by the enthalpy of dissolution ΔH_{S_P} in the polymer layer (Eq. 22), because ΔH_{S_P} was about 8-fold higher than E_{P_B}. The lag time decreased with increasing temperature due to the negative value of ΔH_{S_P}. The partial pressure change due to the temperature increase at a constant RH had a greater effect on the WVTR values than the direct influence of temperature at a constant partial pressure difference. At a constant RH of 36%, the partial pressure changed from 1138 to 2652 Pa within the temperature range 25to40°C, leading to an increase in WVTR for the **BPB** structure from 3.3×10^{-9} to 8.5×10^{-9} molm^{-2}s^{-1}. In contrast, at a constant partial pressure of 1138 Pa, the WVTR only changed from 3.3×10^{-9} to 3.6×10^{-9}molm^{-2}s^{-1} within the same temperature range. A similar behavior was observed for the **BPBPBPB**

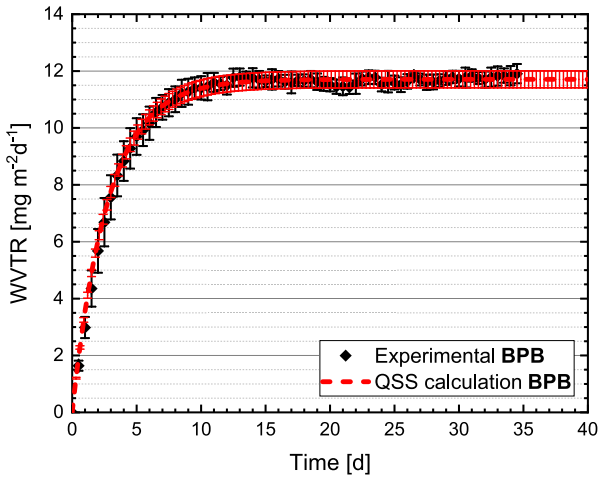

Fig. 4. Time-dependent WVTR of a **BPB** structure at 38 °C and 36 %RH (QSS calculation using Eq. 19).

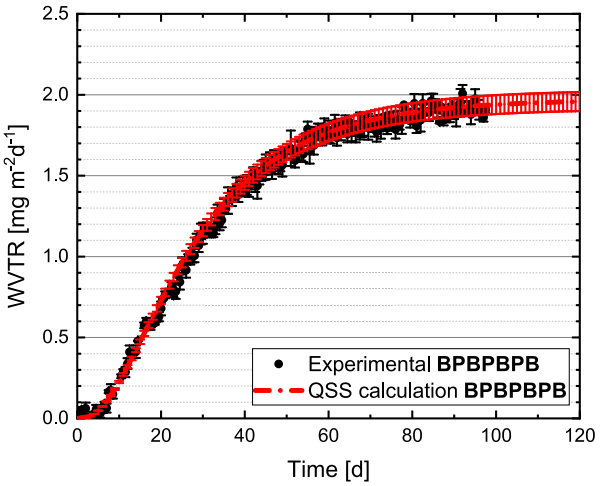

Fig. 5. Time-dependent WVTR of a **BPBPBPB** structure at 38°C and 36%RH (QSS calculation using Eq. 20).

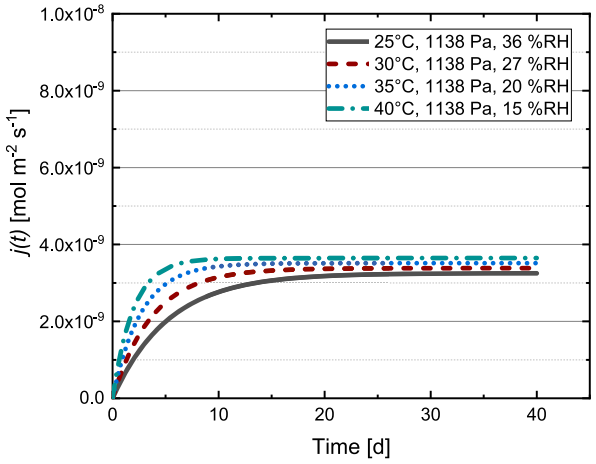

Fig. 6. Calculated time-dependent water vapor flux density of a **BPB** structure at a constant partial pressure of 1138Pa and four different temperatures.

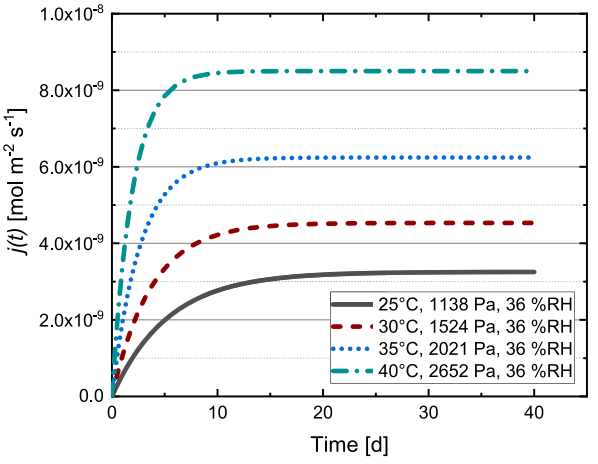

Fig. 8. Calculated time-dependent water vapor flux density of a **BPB** structure at a constant 36%RH and four different temperatures.

structure. The WVTR here increased from 4.7×10^{-10} to 1.4×10^{-9}molm^{-2}s^{-1} at a constant RH of 36 % and from 4.7×10^{-10} to 6.2×10^{-10} mol m^{-2} s^{-1} at a constant partial pressure of 1138 Pa.

4. Conclusion

Temperature dependent quasi-stationary approximations were derived and used to determine the water vapor permeation mechanisms in inorganic and polymeric multilayers. Thereby, the temperature dependency of a multilayered structure differs from that of the substrate film, if permeation through nanoscale defects (<1 nm) of the inorganic layer dominates and capillary condensation, Fick's diffusion and interfacial diffusion are the predominant mechanisms for water vapor transport through the layers [23,25,46].

We found that water vapor permeation in PET/SiO_x films has an activation energy E_{P_B} of 5.7 kJmol^{-1}, which is about twice as high as the value for the PET substrate. Accordingly, the interactions between water and SiO_x have an influence on the permeation mechanism of the two-layer structure.

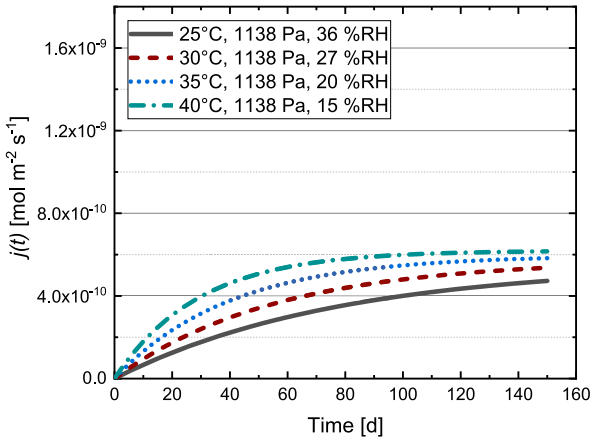

Fig. 7. Calculated time-dependent water vapor flux density of a **BPBPBPB** structure at a constant partial pressure of 1138Pa and four different temperatures.

The equations derived by combining the QSS approach and Arrhenius law revealed the temperature and pressure dependencies of steady-state WVTR and lag time in multilayer structures comprising **BPB** triplets, and the results agreed closely with the experimentally determined values.

It has been found that the temperature dependency of steady-state permeation is determined by the E_P of SiO_x, whereas an ORM layer applied in a three-layer system has only a minor effect on the total measured E_P of 6.7 ± 1.1 kJmol^{-1}, in comparison to the two-layer structure. Therefore, the activation energy in our calculations for the first and second SiO_x layers of the **BPB** structure could be kept constant. However, the ORM layer led to a reduction of the WVTR. We assume that this is due to a filling of the nanoscale defects in the first SiO_x layer and by providing a smooth surface for the second SiO_x layer in **BPB** and **BPBPBPB** structures, with the second SiO_x layer containing fewer nanodefects. This led to a decreased pre-exponential factor P_{0_B} of the permeability in the **BPB** structure in comparison to the two-layer structure, indicating that the density of nanoscale defects may have been reduced, as also previously reported [46,60,61]. Furthermore, an ORM coating on top of the SiO_x layers in both of the multilayer structures (**BPB** and **BPBPBPB**) reduced the value of P_{0_B} even further.

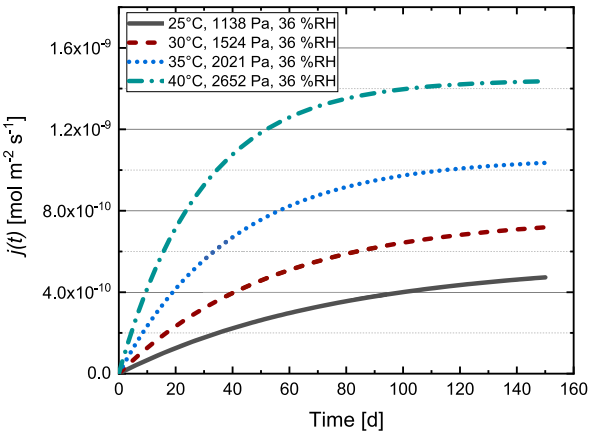

Fig. 9. Calculated time-dependent water vapor flux density of a **BPBPBPB** structure at a constant 36%RH and four different temperatures.

Experimentally determined material-specific parameters help to predict the influence of temperature and relative humidity on the barrier performance of multilayered barrier structures. According to the derived equations, the WVTR increase with temperature is dominated by the increase in the partial pressure, whereas the lag time is mainly influenced by the heat of sorption of the polymeric layer. This allows us to design multilayer barrier films according to the lifetime requirements of sensitive devices. We can, therefore, estimate with greater accuracy the effect of environmental conditions on barrier performance and therefore on the lifetime of such devices.

CRediT authorship contribution statement

Sandra Kiese: Conceptualization, Data curation, Formal analysis, Investigation, Methodology, Validation, Visualization, Writing - original draft. **Esra Kücükpinar:** Conceptualization, Funding acquisition, Supervision, Writing - review & editing. **Oliver Miesbauer:** Methodology, Supervision, Validation, Writing - review & editing. **Horst-Christian Langowski:** Supervision, Writing - review & editing.

Declaration of Competing Interest

The authors declare that they have no known competing financial interests or personal relationships that could have appeared to influence the work reported in this paper.

Acknowledgements

The authors thank DuPont Teijin Films, Amcor Flexibles Kreuzlingen AG, and Fraunhofer ISC for supplying the barrier materials and films used in this study. We also thank the laboratory assistants and technicians of the Materials Development Department at Fraunhofer IVV for their support in the production and analysis of the barrier films. This work was financially supported in part by the European Union 7th Framework Program under grant agreements 287,594 (SUNFLOWER project) and 314,068 (TREASORES project).

Supplementary material

Supplementary material associated with this article can be found, in the online version, at 10.1016/j.tsf.2020.138476

References

[1] S. Nagai, A numerical study for the integrative definition of moisture-barrier performance regarding multilayered barrier-stack for an encapsulated system, Surf. Coat. Technol. 267 (2015) 59–64, https://doi.org/10.1016/j.surfcoat.2014.12.035.
[2] R. Dunkel, R. Bujas, A. Klein, V. Horndt, Method of measuring ultralow water vapor permeation for OLED displays, Proc. IEEE 93 (8) (2005) 1478–1482.
[3] K. Choi, S. Nam, Y. Lee, M. Lee, J. Jang, S.J. Kim, Y.J. Jeong, H. Kim, S. Bae, J.-B. Yoo, S.M. Cho, J.-B. Choi, H.K. Chung, J.-H. Ahn, C.E. Park, B.H. Hong, Reduced water vapor transmission rate of graphene gas barrier films for flexible organic field-Effect transistors, ACS Nano 9 (6) (2015) 5818–5824.
[4] Y. Kim, H. Cho, J.H. Heo, T. Kim, N. Myoung, C. Lee, S.H. Im, T. Lee, Multicolored organic/inorganic hybrid perovskite light-emitting diodes, Adv. Mater. 27 (7) (2015) 1248–1254.
[5] H.C. Langowski, Permeation of Gases and Condensable Substances Through Monolayer and Multilayer Structures, Wiley-VCH, pp. 297–347.
[6] J.S. Lewis, M.S. Weaver, Thin-film permeation-barrier technology for flexible organic light-emitting devices, IEEE J. Sel. Top. Quantum Electron. 10 (1) (2004) 45–57.
[7] U. Soo Lee, J. Sik Choi, B. Seob Yang, S. Oh, Y. Jang Kim, M. Sook Oh, J. Heo, H. Joon Kim, Formation of a Bilayer of ALD-SiO_2 and Sputtered Al_2O_3/ZrO_2Films on Polyethylene Terephthalate Substrates as a Moisture Barrier, ECS Solid State Letters 2 (6) (2013) R13–R15.
[8] P.E. Burrows, G.L. Graff, M.E. Gross, P.M. Martin, M.K. Shi, M. Hall, E. Mast, C. Bonham, W. Bennett, M.B. Sullivan, Ultra barrier flexible substrates for flat panel displays, Displays 22 (2) (2001) 65–69.
[9] G. Nisato, M. Kuilder, P. Bouten, L. Moro, O. Philips, N. Rutherford, Thin Film Encapsulation for OLEDs: Evaluation of Multi-layer Barriers using the Ca Test. SID Symposium Digest of Technical Papers 34, Wiley Online Library, 2003, pp. 550–553.
[10] D.A. Spee, J.K. Rath, R.E.I. Schropp, Using hot wire and initiated chemical vapor deposition for gas barrier thin film encapsulation, Thin Solid Films 575 (2015) 67–71.
[11] A.R. Cho, E.H. Kim, S.Y. Park, L.S. Park, Flexible OLED encapsulated with gas barrier film and adhesive gasket, Synth Met 193 (2014) 77–80.
[12] P.E. Burrows, G.L. Graff, M.E. Gross, P.M. Martin, M. Hall, E. Mast, C.C. Bonham, W.D. Bennett, L.A. Michalski, M.S. Weaver, J.J. Brown, D. Fogarty, L.S. Sapochak, Gas permeation and lifetime tests on polymer-based barrier coatings. Organic Light-Emitting Materials and Devices IV 4105, International Society for Optics and Photonics, 2001, pp. 75–83, https://doi.org/10.1117/12.416878.
[13] M. Park, S. Oh, H. Kim, D. Jung, D. Choi, J.-S. Park, Gas diffusion barrier characteristics of Al_2O_3/alucone films formed using trimethylaluminum, water and ethylene glycol for organic light emitting diode encapsulation, Thin Solid Films 546 (2013) 153–156.
[14] Y.C. Han, E. Kim, W. Kim, H.-G. Im, B.-S. Bae, K.C. Choi, A flexible moisture barrier comprised of a SiO_2-embedded organic inorganic hybrid nanocomposite and Al_2O_3 for thin-film encapsulation of OLEDs, Org Electron 14 (6) (2013) 1435–1440.
[15] J. Wu, F. Fei, C. Wei, X. Chen, S. Nie, D. Zhang, W. Su, Z. Cui, Efficient multi-barrier thin film encapsulation of OLED using alternating Al_2O_3 and polymer layers, RSC Adv 8 (11) (2018) 5721–5727, https://doi.org/10.1039/C8RA00023A.
[16] J. Wang, X. Xu, J. Zhang, M. Chen, S. Dong, J. Han, M. Wei, Moisture-Permeable, humidity-Enhanced gas barrier films based on organic/inorganic multilayers, ACS Applied Materials & Interfaces 10 (33) (2018) 28130–28138, https://doi.org/10.1021/acsami.8b09740.
[17] M. Sun, S. Zhu, C. Zhang, A. Olah, E. Baer, D.A. Schiraldi, HDPE/EVOH Multilayered, high barrier films for flexible organic photovoltaic device packaging, ACS Applied Polymer Materials 1 (2) (2019) 259–266, https://doi.org/10.1021/acsapm.8b00181.
[18] G. Garnier, S. Marouani, B. Yrieix, C. Pompeo, M. Chauvois, L. Flandin, Y. Brechet, Interest and durability of multilayers: from model films to complex films, Polym Adv Technol 22 (6) (2011) 847–856.
[19] J. Affinito, D. Hilliard, A new class of ultra-barrier materials. 47th Annual Technical Conference Proceedings, Society of Vacuum Coaters, 2004, pp. 563–593.
[20] G.L. Graff, R.E. Williford, P.E. Burrows, Mechanisms of vapor permeation through multilayer barrier films: lag time versus equilibrium permeation, J Appl Phys 96 (4) (2004) 1840–1849.
[21] W. Decker, B. Henry, Basic Principles of Thin Film Barrier Coatings. 45th Annual Technical Conference Proceedings, Society of Vacuum Coaters, 2002, pp. 492–502.
[22] B.M. Henry, A.G. Erlat, C.R.M. Grovenor, G.A.D. Briggs, T. Miyamoto, Y. Tsukahara, Gas permeation studies of metal oxide/polymer composite films. 45th Annual Technical Conference Proceedings, Society of Vacuum Coaters, 2002, pp. 514–518.
[23] B.M. Henry, A.G. Erlat, C.R.M. Grovenor, C.S. Deng, G.A.D. Briggs, T. Miyamoto, N. Noguchi, T. Niijima, Y. Tsukahara, The permeation of water vapor through gas barrier films. 44th Annual Technical Conference Proceedings, Society of Vacuum Coaters, 2001, pp. 469–475.
[24] F. Fei, Z. Wang, Q. Chen, Z. Liu, L. Sang, Study of functional barrier layer on PVC by PECVD for migrations resistant, Surf. Coat. Technol. 228 (2013) S61–S66, https://doi.org/10.1016/j.surfcoat.2012.08.040.
[25] A.P. Roberts, B.M. Henry, A.P. Sutton, C.R.M. Grovenor, G.A.D. Briggs, T. Miyamoto, M. Kano, Y. Tsukahara, M. Yanaka, Gas permeation in silicon-oxide/polymer (SiO_x/pet) barrier films: role of the oxide lattice, nano-defects and macro-defects, J Memb Sci 208 (1) (2002) 75–88.
[26] C.E. Rogers, Permeation of Gases and Vapours in Polymers, Chapman & Hall, pp. 11–73.
[27] J.G. Wijmans, R.W. Baker, The solution-diffusion model: a review, J Memb Sci 107 (1) (1995) 1–21.
[28] B.M. Henry, F. Dinelli, K.Y. Zhao, C.R.M. Grovenor, O.V. Kolosov, G.A.D. Briggs, A. P. Roberts, R.S. Kumar, R.P. Howson, A microstructural study of transparent metal oxide gas barrier films, Thin Solid Films 355 (1999) 500–505.
[29] B.M. Henry, A.G. Erlat, A. McGuigan, C.R.M. Grovenor, G.A.D. Briggs, Y. Tsukahara, T. Miyamoto, N. Noguchi, T. Niijima, Characterization of transparent aluminium oxide and indium tin oxide layers on polymer substrates, Thin Solid Films 382 (1–2) (2001) 194–201.
[30] D.G. Howells, B.M. Henry, J. Madocks, H.E. Assender, High quality plasma enhanced chemical vapour deposited silicon oxide gas barrier coatings on polyester films, Thin Solid Films 516 (10) (2008) 3081–3088.
[31] A.G. Erlat, R.J. Spontak, R.P. Clarke, T.C. Robinson, P.D. Haaland, Y. Tropsha, N. G. Harvey, E.A. Vogler, SiO_xgas barrier coatings on polymer substrates: morphology and gas transport considerations, The Journal of Physical Chemistry B 103 (29) (1999) 6047–6055.
[32] S. Arrhenius, ber die Reaktionsgeschwindigkeit bei der inversion von Rohrzucker durch Suren, Zeitschrift für physikalische Chemie 4.1 (1889) 226–248.
[33] P.W. Atkins, J. de Paula, Physikalische Chemie, Wiley-VCH, 2013.
[34] J. Fahlteich, M. Fahland, W. Schoenberger, N. Schiller, Permeation barrier properties of thin oxide films on flexible polymer substrates, Thin Solid Films 517 (10) (2009) 3075–3080.
[35] Polymer Handbook, in: J. Brandup, E. Immergut, E. Grulke (Eds.), Wiley, 1999.
[36] A.S. da Silva Sobrinho, G. Czeremuszkin, M. Latreche, M.R. Wertheimer, Defect-permeation correlation for ultrathin transparent barrier coatings on polymers, Journal of Vacuum Science & Technology A 18 (1) (2000) 149–157.
[37] M.S. Hedenqvist, K.S. Johansson, Barrier properties of SiO_x-coated polymers: multi-layer modelling and effects of mechanical folding, Surf. Coat. Technol. 172 (1) (2003) 7–12, https://doi.org/10.1016/S0257-8972(03)00312-8.

[38] K. Kessler. O_2- und H_2O-Permeation durch SiO_x-beschichtete PET-Folien, ETH Zürich, 1994.
[39] Y.G. Tropsha, N.G. Harvey, Activated rate theory treatment of oxygen and water transport through silicon oxide poly(ethylene terephthalate) composite barrier structures, J. Phys. Chem. B 101 (13) (1997) 2259–2266, https://doi.org/10.1021/jp9629856.
[40] S. Amberg-Schwab, K. Noller, U. Weber, O. Miesbauer, Hochbarrierenverbunde und Verfahren zu ihrer Herstellung, NormEP2272928 A1 (2011).
[41] L. Vaskova. On line control of transparent inorganic layers deposited on polymeric substrate by phase modulated spectroscopic ellipsometry, Technische Universität München, 2006.
[42] Deutsches Institut für Normung e.V, DIN53122-1 - Prüfung von Kunststoff-Folien, Elastomerfolien, Papier, Pappe und anderen Flchengebilden - Bestimmung der Wasserdampfdurchlssigkeit - Teil 1: Gravimetrisches Verfahren, 2001.
[43] S. Kiese, E. Kücükpinar, M. Reinelt, O. Miesbauer, J. Ewender, H.-C. Langowski, A systematic approach for the accurate and rapid measurement of water vapor transmission through ultra-high barrier films, Rev. Sci. Instrum. 88 (2) (2017) 025108.
[44] J. Crank, The Mathematics of Diffusion, Oxford university press, 1975.
[45] O. Miesbauer. Analytische und numerische Berechnungen zur Barrierewirkung von Mehrschichtstrukturen, Technische Universität München, 2017.
[46] S. Kiese, E. Kücükpinar, O. Miesbauer, H.-C. Langowski, Time-dependent water vapor permeation through multilayer barrier films: empirical versus theoretical results, Thin Solid Films 672 (2019) 199–205, https://doi.org/10.1016/j.tsf.2019.01.001.
[47] K. Königsberger, Analysis 2, Springer-Verlag, 2013.
[48] P.O. Scherer, Computational Physics Simulation of Classical and Quantum Systems 2nd ed., 2013.
[49] B.D. Vogt, H.-J. Lee, V.M. Prabhu, D.M. DeLongchamp, E.K. Lin, W.-l. Wu, S. K. Satija, X-ray and neutron reflectivity measurements of moisture transport through model multilayered barrier films for flexible displays, J Appl Phys 97 (11) (2005), 114509–1–114509–7.
[50] S.-W. Seo, E. Jung, C. Lim, H. Chae, S.M. Cho, Water permeation through organic-inorganic multilayer thin films, Thin Solid Films 520 (21) (2012) 6690–6694.
[51] S. Amberg-Schwab, M. Hoffmann, H. Bader, M. Gessler, Inorganic-organic polymers with barrier properties for water vapor, oxygen and flavors, J Solgel Sci Technol 13 (1–3) (1998) 141–146.
[52] K.H. Haas, S. Amberg-Schwab, K. Rose, G. Schottner, Functionalized coatings based on inorganic organic polymers (ORMOCER) and their combination with vapor deposited inorganic thin films, Surf. Coat. Technol. 111 (1) (1999) 72–79.
[53] J. Fahlteich, C. Steiner, N. Schiller, O. Miesbauer, K. Noller, K.-J. Deichmann, M. Mirza, S. Amberg-Schwab, Roll-to-roll thin film coating on fluoropolymer webs: status, challenges and applications, Surf. Coat. Technol. 314 (Supplement C) (2017) 160–168.
[54] T. Shigetomi, H. Tsuzumi, K. Toi, T. Ito, Sorption and diffusion of water vapor in poly(ethylene terephthalate) film, J Appl Polym Sci 76 (1) (2000) 67–74.
[55] E. Pons, B. Yrieix, L. Heymans, F. Dubelley, E. Planes, Permeation of water vapor through high performance laminates for VIPs and physical characterization of sorption and diffusion phenomena, Energy Build 85 (2014) 604–616.
[56] M.M. Schmidt. High barrier materials for flexible and transparent encapsulation of organic electronics, Technische Universität München, 2013.
[57] D.W. Van Krevelen, K. Te Nijenhuis, Chapter 18 - Properties Determining Mass Transfer In Polymeric Systems, Elsevier, Amsterdam, pp. 655–702. 10.1016/B978-0-08-054819-7.00018-2.
[58] S. Amberg-Schwab, Inorganic–organic polymers with barrier properties against water vapor, oxygen and migrating monomers, Handbook of Sol-Gel Science and Technology Processing Characterization and Applications 3 (2004) 455–478.
[59] M. Benmalek, H.M. Dunlop, Inorganic coatings on polymers, Surf. Coat. Technol. 76–77 (1995) 821–826, https://doi.org/10.1016/0257-8972(95)02601-0.
[60] V.R. Tobin, H. Suttle, H.E. Assender, Nanodefect-controlled permeation in AlO_x/polymer gas barrier films, Thin Solid Films 642 (2017) 142–150, https://doi.org/10.1016/j.tsf.2017.09.019.
[61] A. Bieder, A. Gruniger, R. von Rohr, Deposition of SiO_x diffusion barriers on flexible packaging materials by PECVD, Surf. Coat. Technol. 200 (1) (2005) 928–931, https://doi.org/10.1016/j.surfcoat.2005.02.004.
[62] R.M. Barrer, Diffusion in and through solids, in: The Cambridge Series of Physical Chemistry, Cambridge University Press, Cambridge, England, 1941.

5 Discussion, conclusion and outlook

Recent developments in encapsulation materials require appropriate methodologies and optimized measurement technology to be able to predict the lifetime of encapsulated products and to detect low permeabilities within acceptable periods of time. The aim of this thesis was to develop an approach using a combination of optimized measurement technology and a theoretical model enabling a simplified method for the calculation of the time-dependent behaviour of the water vapour permeation through multilayer structures at different climate conditions. Therefore, the comparability of measurement results from different measurement methods and under different measurement conditions should be assured. By increasing the measurement temperature together with modelling and prediction of steady-state permeation values, the measurement time should be reduced. Additionally, after the experimental validation of the theoretical approximation equations derived by Miesbauer [32] and a combination of these equations with Arrhenius' laws, the permeation values as a function of time should be predicted for different climate conditions. By this way, the permeation mechanisms and temperature dependencies of water vapor transport through multilayer barrier structures should be investigated, with particular attention to the roles of the coefficients of diffusion D, solubility S and permeation P of each layer.

Measurement of barrier properties

The water vapor permeation rate results of the ultra-permeation accumulation (UPA) device described herein were validated using polychlorotrifluoroethylene (PCTFE) films under different conditions and two specific multilayer high-barrier films. The latter consisted of alternating inorganic silicon oxide (SiO_x) and hybrid-polymeric ORMOCER® (ORM) layers on the top of a polyethylene terephthalate (PET) substrate. Two of these structures were laminated face-to-face against each other using an adhesive (Adh). All measured values agreed well with values measured using the MOCON® Aquatran® devices. The advantage over

conventional measurement instruments is the large measurement area of about 188 cm^2, so that the results provide a realistic average value over the sample area. In addition, 30 different samples can be measured in parallel and the measurement temperatures and relative humidities (RH) can be variably adjusted over a wide range of 23 °C to 80 °C and 15 % to 90 % RH, respectively. The sensitivity of the measurement device is $2 \times 10^{-5}\,g\,m^{-2}\,d^{-1}$.

The measurements of the high-barrier films were accompanied by numerical simulations, which made it possible to predict the steady-state values of permeation and thus significantly reduce the measurement times from several months to a few weeks. For the simulations D and S values of each layer were required. For PET, values from the literature were used. It was found that the diffusion coefficients of the polymeric layers had no influence on the shape of the flux curve, as long as they are more than two orders of magnitude higher than D of the inorganic layers. In addition, D and S of the SiO_x layer could be varied without changing the result as long as their product, i.e. P, remained the same.

Confirmation and evaluation of existing theories

These observations are also reflected in the equations derived by Miesbauer [32] for structures including at least one **BPB** triplet of alternating barrier **B** and polymer **P** layers, which shows that it is feasible to use the ideal laminate model for the permeation of water vapor through these structures. Under the condition that the ratios of permeability coefficients of the **P** and **B** layers $P_{\mathbf{P}}/P_{\mathbf{B}}$ and ratios of solubility coefficients of the **P** and **B** layers $S_{\mathbf{P}}/S_{\mathbf{B}}$ are sufficiently high, **P** layers do not necessarily have to be polymers and **B** layers do not necessarily have to be inorganic materials to apply the quasi-stead-state (QSS) approximation equations.

The equations state that the stationary value of the permeation rate is only determined by the permeability coefficient $P_{\mathbf{B}}$ and the thickness of the **B** layers. The lag time, on the other hand, is determined by $P_{\mathbf{B}}$ and the solubility coefficient of the **P** layer $S_{\mathbf{P}}$, which is divided or multiplied by the thickness of the corresponding layer, respectively. It is remarkable that the calculations for the two SiO_x layers used average values of their $P_{\mathbf{B}}$. Nevertheless, the calculated time-dependent and steady-state permeation values, as well as the lag times, were in agreement with the experimental data. Thus, it does not matter whether inorganic layers of different quality or layers with the same permeation properties are applied, as long as their permeability coefficients are still several orders of magnitude lower than that of the intermediate layers. In the multilayer they act

together and their average $P_{\mathbf{B}}$ can be used. The same applies to the polymer layers, where the average values from $h_{\mathbf{P}}S_{\mathbf{P}}$ from ORM and/or Adh were used in the calculations. Due to the orders of magnitude of $S_{\mathbf{P}}$ and $P_{\mathbf{B}}$ of our materials, the solubility of the water vapor in the polymer layers dominates the lag time. These results are in agreement with literature. Graff et al. [64] demonstrated theoretically that the permeation can be significantly delayed by using multilayer structures with alternating layers with different solubility coefficients [64, 69–73]. However, the equations derived by Graff et al. [64] still require the prior determination of D and S of each layer. This can be difficult, especially for the inorganic layers, as they cannot be measured as a free-standing layer and the permeation properties change depending on the substrate or layer that is coated on top. The QSS approximations show, for certain kind of structures, which include **BPB** triplets that the $D_{\mathbf{B}}$ and $S_{\mathbf{B}}$ values of the inorganic layers have no influence on the permeation result and the lag time, only their product $P_{\mathbf{B}}$. Accordingly, D and S do not have to be measured separately. In addition, only the solubility coefficients of the polymer layers have to be determined, since $D_{\mathbf{P}}$ also has no influence on steady-state permeation and lag time. The S values of the polymers and the inorganic layers used in this work differed by at least factor 100, allowing the application of the QSS approximations. This strategy allows the prediction of the performance and lag time of multilayer structures consisting of at least one **BPB** triplet, helping to reduce the experimental timeframe required for permeation measurements without additional numerical simulations.

The results of the experimental determination of the water vapor permeation rates of a PET substrate and multilayer films with up to 11 layers were in agreement with the theoretical findings as well. Based on the empirical data and the calculations performed using the ideal laminate theory, the permeability $Q_{\mathbf{B}}$ of the SiO_x layer was up to five orders of magnitude lower than that of the polymer layers and had the greatest impact on the steady-state water vapor permeation rates. Long lag times can be reached by multilayers incorporating **BPB** triplets. The laminate structures, which contain a thick polymer layer ($> 3\,\mu m$) with a high solubility coefficient $S_{\mathbf{P}}$ embedded between barrier layers, showed the longest lag times of above 30 days. This so-called internal desiccant effect leading to an significant increase of the lag time due to the assembly of alternating dyads was also reported for other polymer/barrier combinations, such as organic self-assembled monolayers and inorganic TiO_2, and was also attributed to an accumulation of water in the polymer layer [70, 71].

The permeability coefficients for water vapor of the measured polymer matrices can be ranked highest to lowest as follows: $P_{\mathrm{Adh}} > P_{\mathrm{ORM}} > P_{\mathrm{PET}}$. The diffusion

coefficients can similarly be ranked as $D_{\mathrm{Adh}} > D_{\mathrm{PET}} > D_{\mathrm{ORM}}$, and the solubility coefficients as $S_{\mathrm{ORM}} > S_{\mathrm{Adh}} > S_{\mathrm{PET}}$. Accordingly, the ORM layer has the highest S among the three polymers, which leads to a significant increase in lag time when it is placed between two **B** layers.

The $Q_{\mathbf{B}}$ values for the first and second SiO_x layers of the multilayered structures were calculated using the ideal laminate theory as well. This showed that the first SiO_x layer (directly coated on the PET substrate) had a permeability of $1.9 \times 10^{-11}\,\mathrm{mol\,m^{-2}\,s^{-1}\,Pa^{-1}}$, which is about a factor of five higher than the value of the second SiO_x layer ($3.9 \times 10^{-12}\,\mathrm{mol\,m^{-2}\,s^{-1}\,Pa^{-1}}$) applied on top of ORM. It is assumed that the planarization effect of ORM, providing a smoother surface for inorganic barrier layer deposition, reduces the permeability of SiO_x, when deposited on an ORM layer, as previously reported for fluoropolymer substrates [146].

Permeation mechanisms

In order to further investigate the water vapor permeation mechanisms in inorganic and organic multilayer structures, the temperature dependency of multilayered structures was measured using the UPA device. If permeation through macroscale defects (>1 nm) of inorganic layers is negligible and capillary condensation, Fick's diffusion and interfacial diffusion are the predominant mechanisms for water vapor transport through the layers, the activation energy of permeation E_P of the multilayer structure should differ from that of the substrate film [47, 128, 147]. This was the case for the PET/SiO_x films measured in this work. The E_P of these films is $\sim$5.7 kJ mol^{-1}, which is about twice as high as the value for the PET substrate. Accordingly, the interactions between water and SiO_x have an influence on the permeation mechanism of the two-layer structure as determined by the values of E_P. An ORM layer on top of the SiO_x had no additional effect on the water vapor permeation mechanisms, as also indicated by the measured E_P for PET/SiO_x/ORM being similar to that of PET/SiO_x.

The combination of QSS approximation equations and Arrhenius' laws revealed the temperature and partial pressure dependencies of the steady-state flux as a function of time $j(t,T)$ and the lag time in multilayer structures comprising **BPB** triplets and are the central equations of this thesis. Therefore they are repeated here once again:

$$j(t,T) = \frac{P_{0_{\mathbf{B}}} p}{2\,h_{\mathbf{B}}} \exp\Big(\frac{-E_{P_{\mathbf{B}}}}{RT}\Big)\left(1 - \exp\left(-\frac{2\,P_{0_{\mathbf{B}}}}{h_{\mathbf{B}} h_{\mathbf{P}} S_{0_{\mathbf{P}}}} \exp\Big(\frac{\Delta H_{S_{\mathbf{P}}} - E_{P_{\mathbf{B}}}}{RT}\Big) t\right)\right) \tag{5.1}$$

for **BPB** structures and

$$
\begin{aligned}
j\left(t,T\right) = \frac{P_{0_{\mathbf{B}}} p}{4\, h_{\mathbf{B}}} \exp\left(\frac{-E_{P_{\mathbf{B}}}}{RT}\right) \\
\cdot \Bigg(1 - \left(\frac{1}{\sqrt{2}} + 1\right) \exp\left(\left(\sqrt{2} - 2\right) \frac{P_{0_{\mathbf{B}}}}{h_{\mathbf{B}} h_{\mathbf{P}} S_{0_{\mathbf{P}}}} \exp\left(\frac{\Delta H_{S_{\mathbf{P}}} - E_{P_{\mathbf{B}}}}{RT}\right) t\right) \\
+ \exp\left(-2 \frac{P_{0_{\mathbf{B}}}}{h_{\mathbf{B}} h_{\mathbf{P}} S_{0_{\mathbf{P}}}} \exp\left(\frac{\Delta H_{S_{\mathbf{P}}} - E_{P_{\mathbf{B}}}}{RT}\right) t\right) \\
+ \left(\frac{1}{\sqrt{2}} - 1\right) \exp\left(\left(-\sqrt{2} - 2\right) \frac{P_{0_{\mathbf{B}}}}{h_{\mathbf{B}} h_{\mathbf{P}} S_{0_{\mathbf{P}}}} \exp\left(\frac{\Delta H_{S_{\mathbf{P}}} - E_{P_{\mathbf{B}}}}{RT}\right) t\right)\Bigg)
\end{aligned}
\tag{5.2}
$$

for **BPBPBPB** structures.

Accordingly, the water vapor permeation rate increase with temperature is mainly determined by the increase in water vapor partial pressure. If this is kept constant during the temperature increase by reducing the relative humidity accordingly, the increase in water vapor permeation rate is determined by the activation energy of permeation through the barrier layer $E_{P_{\mathbf{B}}}$. Since this value is only about $5.7\,\mathrm{kJ\,mol^{-1}}$ for the SiO_x layer used, this effect on the increase in water vapor permeation rate was negligible. The temperature dependency of the lag time, on the other hand, is determined by the difference between the heat of sorption of the polymeric layer $\Delta H_{S_{\mathbf{P}}}$ and $E_{P_{\mathbf{B}}}$. Since the amount of $\Delta H_{S_{\mathbf{P}}}$ being $-45\,\mathrm{kJ\,mol^{-1}}$ is about 7.5 times as high as $E_{P_{\mathbf{B}}}$, the sorption behavior of the polymer layer again dominates the lag time of the multilayer film. These results are also in agreement with literature, where it has been shown that alternating structures of polymers and inorganic layers with low defect density result in a large increase of the lag time and have only little influence on the steady-state permeation rate [64].

Although an ORM layer, based on calculations using the ideal laminate model, should have no effect on the water vapor permeation rate of the films, it slightly reduces the permeability of both, the first and the second SiO_x layer. Probably the reason for this is a filling of the nanoscale defects in the first SiO_x layer and providing a smooth substrate surface for the second SiO_x layer deposition in **BPB** and **BPBPBPB** structures. Accordingly, the pre-exponential factor $P_{0_{\mathbf{B}}}$ of the permeability in the **BPB** structure also decreased in comparison to the two-layer structure. This factor depends on the number of nanoscale defects, which can be reduced due to the decline in surface roughness, as also previously reported [17, 148, 149]. Furthermore, an ORM coating on top of the SiO_x layers in both of the multilayer structures (**BPB** and **BPBPBPB**) reduced the value

of $P_{0_{\mathbf{B}}}$ even further, which again gives an indication of the possible filling of the nanoscale defects.

Experimentally determined material-specific parameters helped to predict the influence of temperature and RH on the estimated barrier performance of multilayer barrier structures. This allows to design multilayer barrier films according to the lifetime requirements of sensitive devices and to estimate the effect of environmental conditions on barrier performance and therefore on the lifetime of such devices with greater accuracy. These equations can be applied to all multilayer structures with at least one **BPB** triplet where $P_{\mathbf{P}}/P_{\mathbf{B}}$ and $S_{\mathbf{P}}/S_{\mathbf{B}}$ are higher than 100. As long as this condition is fulfilled, **P** layers do not necessarily have to be polymers and **B** layers do not necessarily have to be inorganic materials. Only the layer thicknesses, $P_{0_{\mathbf{B}}}$, $S_{0_{\mathbf{P}}}$ and the activation energies $E_{P_{\mathbf{B}}}$ and $\Delta H_{S_{\mathbf{P}}}$ of each layer need to be measured, as well as the stationary water vapor permeation rate at one temperature. Then the transient water vapor permeation rates and lag times at a wide range of partial pressure and temperature conditions can be calculated.

6 Summary

Technical products, such as flexible organic electronic devices, are encapsulated with films to protect them from environmental influences. As the required low water vapor and oxygen permeabilities cannot be achieved with polymer films or barrier films developed for sensitive food packaging, the barrier properties are commonly increased by deposition of alternating dyads of inorganic barrier and polymeric intermediate layers deposited on polymeric substrate films. However, due to the continuous improvement of encapsulation materials, the need for improved measurement technology to determine permeabilities in acceptable periods of time also increased.

Within the scope of this thesis, the ultra-permeation accumulation (UPA) measurement device was adapted to detect as small amounts of permeate as possible. On the other hand a theoretical model based on a quasi-stationary approximation for barrier/polymer/barrier (**BPB**)-type structures was experimentally validated. By combining these two approaches it is possible to reduce measurement times significantly and to predict permeation values and lag times for different climate conditions. The main results of the thesis are summarized in the following.

Comparability of measurement results from different measurement methods and under different measurement conditions

The UPA device was modified within this thesis to allow adjustment of measurement conditions (temperature and relative humidity (RH)) within a wide range of 23 °C to 80 °C and 15 % to 90 % RH, respectively. By measuring large sample sizes as a function of time, results are obtained that show a realistic average value over the sample area and ensure that the measurement time was sufficient to reach the steady state. In addition, the measurement conditions can be adapted to other measurement devices to compare the results more accurately. By this way the results were in agreement with those obtained by using commercially available Aquatran® devices.

Experimental validation of the theoretical approximation equations and reduction of measurement time by modelling and prediction of steady-state values

The quasi-steady-state (QSS) approximation equations were developed for multilayer structures with at least one **BPB** triplet under the assumption that the ideal laminate model applies. For the structures investigated in this thesis, the calculated curves agreed closely with the measured data. By adapting the QSS approximation to the experimental data, the long-time results can be predicted relatively early during the measurement process with high accuracy, thus shortening the experimental measurement time. This is especially beneficial in the case of multilayer structures, where reaching stationary permeation may require several months, sometimes even years. It is of particular interest that in the calculations for the two silicon oxide (SiO_x) layers average values of their permeability coefficients $P_{\mathbf{B}}$ were used. This had no influence on the stationary permeation value or the lag time, which both agreed with the experimental data. As long as all $P_{\mathbf{B}}$ were several orders of magnitude lower than the permeability coefficients of the polymer layers $P_{\mathbf{P}}$, it does not seem to matter whether inorganic layers of different quality or layers with the same permeation properties are used. In the multilayer structure, their average $P_{\mathbf{B}}$ can be used. The same applies to the polymer layers, which consisted of ORMOCER® (ORM) and/or adhesive (Adh). In each case, the mean values from their thicknesses times solubility coefficients ($h_{\mathbf{P}} S_{\mathbf{P}}$) were used in the calculations and all results were consistent with the experiments, as well.

Reduction of the measurement time by increasing the temperature and conversion to other climate conditions

According to the QSS equations, the lag time in multilayer structures with at least one **BPB** triplet depends on the quotient of $S_{\mathbf{P}}/P_{\mathbf{B}}$. For the ORM interlayers used, the heat of sorption $\Delta H_{S_{\mathbf{P}}}$ was $-45.7 \pm 0.7\,\mathrm{kJ\,mol^{-1}}$ and the activation energy of permeation $E_{P_{\mathbf{B}}}$ of the SiO_x layers was $5.7 \pm 1.3\,\mathrm{kJ\,mol^{-1}}$. Therefore, an increase in temperature leads to a decrease of $S_{\mathbf{P}}$ and an increase of $P_{\mathbf{B}}$, which in the quotient leads to an overall reduction of the lag time and thus to a reduced measurement time. Using the derived combined equations of QSS approximations and Arrhenius' laws, the stationary permeation values and lag times can be calculated for any other measurement condition, thus ensuring comparability with other measurement instruments.

Permeation mechanisms of water vapor through multilayer barrier structures and influence of solubility and diffusion coefficients of inorganic and polymeric layers on permeability, lag time and temperature behaviour of permeation in multilayer barrier structures

By determining the permeability, solubility and diffusion coefficients at different temperatures, the corresponding activation energies were calculated. These allow a statement about the permeation mechanisms in the individual layers. Accordingly, the contribution of nanodefects in the inorganic layers is the dominant effect in stationary water vapor permeation. This confirms the hypothesis that water vapor permeates continuously through the layers and the use of the ideal laminate model for the permeation of water vapor, in contrast to oxygen permeation, is correct. In addition, the temperature dependencies of steady-state permeation and lag time can be derived from the combined equations of Arrhenius' laws and QSS equations. According to these, the activation energy of permeation through the barrier layers $E_{P_{\mathbf{B}}}$ determines the steady-state final value, whereas the difference between the heat of sorption of the polymer layer and the activation energy of the barrier layer ($\Delta H_{S_{\mathbf{P}}} - E_{P_{\mathbf{B}}}$) determines the lag time. Since the absolute value of $\Delta H_{S_{\mathbf{P}}}$ in the investigated polymer materials was significantly larger than $E_{P_{\mathbf{B}}}$, the solubility of the polymer layer has the dominant influence on the lag time.

In summary, the results of this thesis have provided insights into the permeation mechanisms of water vapor through multilayer structures, as well as the contributions of polymeric and inorganic layers and their defects. The prediction of steady-state values and lag times for multilayer structures consisting of alternating **B** and **P** layers under different climatic conditions is possible with the developed approximate equations. This allows not only a significant reduction of experimental measurement times but also the theoretical design of structural sequences based on the requirements of sensitive devices.

7 Zusammenfassung

Technische Produkte, wie z. B. flexible organische elektronische Geräte, werden mit Folien verkapselt, um sie vor Umwelteinflüssen zu schützen. Da die geforderten niedrigen Wasserdampf- und Sauerstoffdurchlässigkeiten mit Polymerfolien oder Barrierefolien, die für empfindliche Lebensmittelverpackungen entwickelt wurden, nicht erreicht werden können, werden die Barriereeigenschaften üblicherweise durch die Abscheidung von alternierenden Dyaden aus anorganischen Barriere- und polymeren Zwischenschichten auf polymeren Substratfolien erhöht. Durch die kontinuierliche Verbesserung der Verkapselungsmaterialien stieg jedoch auch der Bedarf an verbesserter Messtechnik zur Bestimmung der Permeabilität in akzeptablen Zeiträumen.

Im Rahmen dieser Arbeit wurde das am Fraunhofer IVV entwickelte Ultra-Permeations-Akkumulations (UPA) Messgerät so angepasst, dass möglichst geringe Mengen an Permeat erfasst werden können. Zum anderen wurde ein theoretisches Modell basierend auf einer quasistationären Näherung für alternierende Barriere/Polymer/Barriere (**BPB**) Strukturen experimentell validiert. Durch die Kombination dieser beiden Ansätze ist es möglich, die Messzeiten deutlich zu reduzieren und Permeationswerte und Verzögerungszeiten für verschiedene Klimabedingungen vorherzusagen. Die wichtigsten Ergebnisse der Arbeit werden im Folgenden zusammengefasst.

Vergleichbarkeit der Messergebnisse von verschiedenen Messmethoden und unter verschiedenen Messbedingungen

Das UPA-Gerät wurde im Rahmen dieser Arbeit so modifiziert, dass die Messbedingungen (Temperatur und relative Feuchte (RH)) in einem weiten Bereich von 23 °C to 80 °C und 15 % to 90 % RH eingestellt werden können. Durch die Messung großer Probenflächen als Funktion der Zeit erhält man Ergebnisse, die einen realistischen Durchschnittswert über die Proben zeigen und sicherstellen, dass die Messzeit ausreichend ist, um den stationären Zustand zu erreichen. Darüber hinaus können die Messbedingungen an andere Messgeräte angepasst werden, um die Ergebnisse besser vergleichen zu können. Auf diese Weise stimmten die

Ergebnisse mit denen handelsüblicher Aquatran®-Geräte überein.

Experimentelle Validierung von theoretischen Näherungsgleichungen und Verkürzung der Messzeit durch Modellierung und Vorhersage von stationären Werten

Die quasistationären (QSS) Näherungsgleichungen wurden für Mehrschichtstrukturen mit mindestens einem **BPB**-Triplett unter der Annahme entwickelt, dass das ideale Laminatmodell gilt. Für die in dieser Arbeit untersuchten Strukturen stimmten die berechneten Kurven gut mit den Messdaten überein. Durch die Anpassung der QSS-Approximation an die experimentellen Daten konnten die stationären Ergebnisse schon relativ früh während des Messprozesses mit hoher Genauigkeit vorhergesagt werden, wodurch die experimentelle Messzeit verkürzt werden konnte. Dies ist besonders vorteilhaft bei mehrschichtigen Strukturen, bei denen das Erreichen der stationären Permeation mehrere Monate, manchmal sogar Jahre dauern kann. Besonders interessant ist, dass bei den Berechnungen für die beiden Siliciumoxid- (SiO_x) Schichten Durchschnittswerte ihrer Permeationskoeffizienten $P_{\mathbf{B}}$ verwendet wurden. Dies hatte keinen Einfluss auf den stationären Permeationswert oder die Verzögerungszeit, die beide mit den experimentellen Daten übereinstimmten. Wenn alle $P_{\mathbf{B}}$ mehrere Größenordnungen niedriger waren als die Permeationskoeffizienten der Polymerschichten $P_{\mathbf{P}}$, scheint es keine Rolle zu spielen, ob anorganische Schichten unterschiedlicher Qualität oder Schichten mit den gleichen Permeationseigenschaften verwendet werden. Im Mehrschichtaufbau kann deren Mittelwert $P_{\mathbf{B}}$ verwendet werden. Gleiches gilt für die Polymerschichten, die zum Teil aus ORMOCER® (ORM) und/oder Klebstoff bestanden. In jedem Fall wurden die Mittelwerte aus Schichtdicken multipliziert mit Löslichkeitskoeffizienten ($h_{\mathbf{P}}S_{\mathbf{P}}$) für die Berechnungen verwendet und alle Ergebnisse stimmten auch mit den experimentellen Daten überein.

Verkürzung der Messzeit durch Erhöhung der Temperatur und Umstellung auf andere Klimabedingungen

Nach den QSS-Gleichungen hängt die Verzögerungszeit in Mehrschichtstrukturen mit mindestens einem **BPB**-Triplett vom Quotienten aus $S_{\mathbf{P}}/P_{\mathbf{B}}$ ab. Für die verwendeten ORM-Zwischenschichten war die Lösungsenthalpie $\Delta H_{S_{\mathbf{P}}}$ $-45.7\pm0.7\,\mathrm{kJ\,mol^{-1}}$ und die Aktivierungsenergie der Permeation $E_{P_{\mathbf{B}}}$ der SiO_x Schichten lag bei $5.7\pm1.3\,\mathrm{kJ\,mol^{-1}}$. Daher führte eine Temperaturerhöhung zu einer Verringerung von $S_{\mathbf{P}}$ und einer Erhöhung von $P_{\mathbf{B}}$, was im Quotienten zu einer Gesamtverringerung der Verzögerungszeit und damit zu einer re-

duzierten Messzeit führte. Mit den abgeleiteten kombinierten Gleichungen aus QSS-Näherungen und Arrhenius-Gesetzen können die stationären Permeationswerte und Verzögerungszeiten für jede andere Messbedingung berechnet werden, sodass die Vergleichbarkeit mit anderen Messgeräten gewährleistet werden kann.

Permeationsmechanismen von Wasserdampf durch mehrschichtige Barrierestrukturen und Einfluss der Löslichkeit und Diffusionskoeffizienten von anorganischen und polymeren Schichten auf Permeabilität, Verzögerungszeit und Temperaturverhalten der Permeation in mehrschichtigen Barrierestrukturen

Durch die Bestimmung der Permeabilitäts-, Löslichkeits- und Diffusionskoeffizienten bei verschiedenen Temperaturen wurden die entsprechenden Aktivierungsenergien berechnet. Diese erlauben eine Aussage über die Permeationsmechanismen in den einzelnen Schichten. Demnach ist der Beitrag von Nanodefekten in den anorganischen Schichten der dominierende Effekt bei der stationären Wasserdampfpermeation. Dies bestätigt die Hypothese, dass Wasserdampf kontinuierlich durch die Schichten permeiert und die Verwendung des idealen Laminatmodells für die Permeation von Wasserdampf, im Gegensatz zur Sauerstoffpermeation, korrekt ist. Darüber hinaus lassen sich die Temperaturabhängigkeiten der stationären Permeation und der Verzögerungszeit aus den kombinierten Gleichungen der Arrhenius-Gesetze und der QSS-Näherungen ableiten. Demnach bestimmt die Aktivierungsenergie der Permeation durch die Barriereschichten ($E_{P_\mathbf{B}}$) den stationären Endwert, während die Differenz zwischen der Lösungsenthalpie der Polymerschicht und der Aktivierungsenergie der Barriereschicht ($\Delta H_{S_\mathbf{P}} - E_{P_\mathbf{B}}$) die Verzögerungszeit bestimmt. Da der Betrag von $\Delta H_{S_\mathbf{P}}$ in den untersuchten Polymermaterialien deutlich größer war als $E_{P_\mathbf{B}}$, hat die Löslichkeit der Polymerschicht den dominierenden Einfluss auf die Verzögerungszeit.

Zusammenfassend haben die Ergebnisse dieser Arbeit Einblicke in die Permeationsmechanismen von Wasserdampf durch mehrschichtige Strukturen, sowie die Beiträge von polymeren und anorganischen Schichten und deren Defekten geliefert. Die Vorhersage von stationären Werten und Verzögerungszeiten für Mehrschichtstrukturen, die aus alternierenden **B** und **P** Schichten bestehen, unter verschiedenen klimatischen Bedingungen, ist mit den entwickelten Näherungsgleichungen möglich. Dies erlaubt nicht nur eine deutliche Reduzierung der experimentellen Messzeiten, sondern auch die theoretische Planung von Schichtreihenfolgen basierend auf den Anforderungen empfindlicher elektronischer Bauteile.

Bibliography

1. Robertson, G. L. *Food Packaging: Principles and Practice* 2nd ed. (CRC Press, Boca Raton, 2006).
2. Langowski, H.-C. in *Plastic Packaging - Interactions with Food and Pharmaceuticals* (eds Piringer, O. G. & Baner, A. L.) 2nd edition, 297–347 (Wiley-VCH, Weinheim, 2008).
3. Baner, A. & Piringer, O. in *Plastic Packaging - Interactions with Food and Pharmaceuticals* (eds Piringer, O. G. & Baner, A. L.) 2nd ed., 89–121 (Wiley-VCH, Weinheim, 2008).
4. Dunkel, R., Bujas, R., Klein, A. & Horndt, V. Method of measuring ultralow water vapor permeation for OLED displays. *Proceedings of the IEEE* **93,** 1478–1482 (2005).
5. Grossiord, N., Kroon, J. M., Andriessen, R. & Blom, P. W. M. Degradation mechanisms in organic photovoltaic devices. *Organic Electronics* **13,** 432–456 (2012).
6. Forrest, S. R. Ultrathin Organic Films Grown by Organic Molecular Beam Deposition and Related Techniques. *Chemical Reviews* **97,** 1793–1896 (1997).
7. Forrest, S. R. & Thompson, M. E. Introduction: organic electronics and optoelectronics. *Chemical Reviews* **107,** 923–925 (2007).
8. Tang, C. W. & VanSlyke, S. A. Organic electroluminescent diodes. *Applied physics letters* **51,** 913–915 (1987).
9. Lewis, J. Material challenge for flexible organic devices. *Materials today* **9,** 38–45 (2006).
10. Logothetidis, S. Flexible organic electronic devices: Materials, process and applications. *Materials Science and Engineering: B* **152,** 96–104 (2008).
11. Schaer, M., Nüesch, F., Berner, D., Leo, W. & Zuppiroli, L. Water vapor and oxygen degradation mechanisms in organic light emitting diodes. *Advanced Functional Materials* **11,** 116–121 (2001).

12. Yang, H. *et al.* Aging susceptibility of terrace-like pentacene films. *The Journal of Physical Chemistry C* **112,** 16161–16165 (2008).

13. Choi, K. *et al.* Reduced Water Vapor Transmission Rate of Graphene Gas Barrier Films for Flexible Organic Field-Effect Transistors. *ACS Nano* **9.** PMID: 25988910, 5818–5824 (2015).

14. Kim, Y.-H. *et al.* Multicolored Organic/Inorganic Hybrid Perovskite Light-Emitting Diodes. *Advanced Materials* **27,** 1248–1254 (2015).

15. Wong, W. S. & Salleo, A. *Flexible electronics: materials and applications* (Springer Science & Business Media, 2009).

16. Ciesinski, M. *Flexible Electronics: Why the Interest? Where are the Markets? What's Next?* in *Flextech Alliance for Displays & Flexible, Printed Elextronics* **14** (2010).

17. Lewis, J. S. & Weaver, M. S. Thin-film permeation-barrier technology for flexible organic light-emitting devices. *IEEE Journal of Selected Topics in Quantum Electronics* **10,** 45–57. ISSN: 1077-260X (2004).

18. Moro, L. & Visser, R. J. in *Organic photovoltaics: materials, device physics, and manufacturing technologies* (eds Brabec, C., Scherf, U. & Dyakonov, V.) (WILEY-VCH Verlag GmbH & Co. KGaA, Weinheim, 2008). ISBN: 78-3-527-31675-5.

19. Burrows, P. E. *et al. Gas Permeation and Lifetime Tests on Polymer-Based Barrier Coatings* in *Proceedings of SPIE, Organic Light-Emitting Materials and Devices IV* **4105** (International Society for Optics and Photonics, 2001), 75–83.

20. Weaver, M. S. *et al.* Organic light-emitting devices with extended operating lifetimes on plastic substrates. *Applied Physics Letters* **81,** 2929–2931 (2002).

21. Dennler, G., Lungenschmied, C., Neugebauer, H., Sariciftci, N. & Labouret, A. Flexible, conjugated polymer-fullerene-based bulk-heterojunction solar cells: Basics, encapsulation, and integration. *Journal of Materials Research* **20,** 3224–3233 (2005).

22. Chatham, H. Oxygen diffusion barrier properties of transparent oxide coatings on polymeric substrates. *Surface and Coatings Technology* **78,** 1 –9. ISSN: 0257-8972 (1996).

23. Shaw, D. & Langlois, M. *Some performance characteristics of evaporated acrylate coatings* in *Proc. 7th Int. Conf. Vacuum Web Coating* (1993), 268–276.

24. Soo Lee, U. *et al.* Formation of a Bilayer of ALD-SiO_2 and Sputtered Al_2O_3/ZrO_2 Films on Polyethylene Terephthalate Substrates as a Moisture Barrier. *ECS Solid State Letters* **2,** R13–R15 (2013).

25. Burrows, P. E. *et al.* Ultra barrier flexible substrates for flat panel displays. *Displays* **22,** 65–69 (May 2001).

26. Nisato, G. *et al. Thin Film Encapsulation for OLEDs: Evaluation of Multilayer Barriers using the Ca Test* in *SID Symposium Digest of Technical Papers* **34** (2003), 550–553.

27. Spee, D. A., Rath, J. K. & Schropp, R. E. I. Using hot wire and initiated chemical vapor deposition for gas barrier thin film encapsulation. *Thin Solid Films* **575,** 67–71. ISSN: 0040-6090 (2015).

28. Cho, A. R., Kim, E. H., Park, S. Y. & Park, L. S. Flexible OLED encapsulated with gas barrier film and adhesive gasket. *Synthetic Metals* **193,** 77 –80. ISSN: 0379-6779 (2014).

29. Park, M. *et al.* Gas diffusion barrier characteristics of Al_2O_3/alucone films formed using trimethylaluminum, water and ethylene glycol for organic light emitting diode encapsulation. *Thin Solid Films* **546,** 153–156 (2013).

30. Han, Y. C. *et al.* A flexible moisture barrier comprised of a SiO_2-embedded organic–inorganic hybrid nanocomposite and Al_2O_3 for thin-film encapsulation of OLEDs. *Organic Electronics* **14,** 1435 –1440. ISSN: 1566-1199 (2013).

31. Ash, R., Barrer, R. M. & Palmer, D. G. Diffusion in multiple laminates. *British Journal of Applied Physics* **16,** 873–884 (1965).

32. Miesbauer, O. *Analytische und numerische Berechnungen zur Barrierewirkung von Mehrschichtstrukturen* PhD thesis (Technische Universität München, 2017).

33. Nicolaus, M. & Schäpers, M. in Bach, F.-W., Möhwald, K., Laarmann, A. & Wenz, T. *Moderne Beschichtungsverfahren* (John Wiley & Sons, 2006).

34. Demtröder, W. *Experimentalphysik 3: Atome, Moleküle und Festkörper* Dritte Auflage (Springer, Berlin, 2005).

35. Bishop, C. A. *Vacuum Deposition onto Webs, Films and Foils* Zweite Auflage (Elsevier, Amsterdam, 2011).

36. Martin, P. M. in *Handbook of Deposition Technologies for Films and Coatings (Third Edition)* (ed Martin, P. M.) 3rd Edition, 1–31 (William Andrew Publishing, Kidlington, Oxford, 2010). ISBN: 978-0-8155-2031-3.

37. Fahlteich, J. *Transparente Hochbarriereschichten auf flexiblen Substraten* PhD Thesis (Technische Universität Chemnitz, 2010).

38. Fahlteich, J., Glawe, A. & Vacca, P. in *Organic and Printed Electronics: Fundamentals and Applications* (eds Nisato, G., Lupo, D. & Ganz, S.) 293–354 (CRC Press, Boca Raton, 2016).

39. Schade, K., Stahr, F., Steinke, O. & Stephan, U. Plasmachemische Gasphasenabscheidung – eine Technologie zur Deposition organischer und anorganischer Schichten. *Vakuum in Forschung und Praxis* **17,** 148–154 (2005).

40. Leskelä, M. & Ritala, M. Atomic layer deposition (ALD): from precursors to thin film structures. *Thin Solid Films* **409.** Proceedings of the 2nd Asian Conference on Chemical Vapour Depostion, 138 –146. ISSN: 0040-6090 (2002).

41. Dameron, A. A. *et al.* Gas diffusion barriers on polymers using multilayers fabricated by Al_2O_3 and rapid SiO_2 atomic layer deposition. *The Journal of Physical Chemistry C* **112,** 4573–4580 (2008).

42. Mattox, D. M. *Handbook of physical vapor deposition (PVD) processing* (William Andrew, Kidlington, Oxford, 2010).

43. Guenther, K. H. Microstructure of vapor-deposited optical coatings. *Applied Optics* **23,** 3806–3816 (1984).

44. Tench, R., Chow, R & Kozlowski, M. *What those defects in optical coatings really look like* in *avs* (1994), 2–13.

45. Kessler, K. *O_2- und H_2O-Permeation durch SiO_x-beschichtete PET-Folien* PhD thesis (ETH Zürich, 1994).

46. Thyen, R, Weber, A & Klages, C.-P. Plasma-enhanced chemical-vapour-deposition of thin films by corona discharge at atmospheric pressure. *Surface and Coatings Technology* **97,** 426–434 (1997).

47. Roberts, A. P. *et al.* Gas permeation in silicon-oxide/polymer (SiO_x/PET) barrier films: role of the oxide lattice, nano-defects and macro-defects. *Journal of Membrane Science* **208,** 75–88. ISSN: 0376-7388 (2002).

48. Garcia-Ayuso, G, Vazquez, L & Martinez-Duart, J. Atomic force microscopy (AFM) morphological surface characterization of transparent gas barrier coatings on plastic films. *Surface and coatings technology* **80,** 203–206 (1996).

49. Barker, C., Kochem, K.-H., Revell, K., Kelly, R. & Badyal, J. Atomic force microscopy and permeability study of stretching-induced gas barrier loss of AlOx layers. *Thin Solid Films* **259,** 46–52 (1995).

50. Mallik, R., Henriksen, P., Butler Jr, T, Kulnis Jr, W. & Confer, T. Characterization of ultrathin sputtered SiO films on alumina by inelastic electron tunneling spectroscopy and atomic force microscopy. *Journal of Vacuum Science & Technology A: Vacuum, Surfaces, and Films* **10,** 2412–2418 (1992).

51. Erlat, A. G. *et al.* SiO_x gas barrier coatings on polymer substrates: morphology and gas transport considerations. *The Journal of Physical Chemistry B* **103,** 6047–6055 (1999).

52. Benmalek, M & Dunlop, H. Inorganic coatings on polymers. *Surface and Coatings Technology* **76,** 821–826 (1995).

53. Fahlteich, J., Fahland, M., Straach, S., Günther, S. & Schiller, N. Transparente Barriereschichten auf flexiblen Polymersubstraten. *Vakuum in Forschung und Praxis* **23,** 29–37 (2011).

54. Struller, C., Kelly, P. & Copeland, N. Aluminum oxide barrier coatings on polymer films for food packaging applications. *Surface and Coatings Technology* **241.** Selected Papers from the Society of Vacuum Coaters 56th Annual Technical Conference - SVC TechCon 2013, 130–137. ISSN: 0257-8972 (2014).

55. Sarkar, J. in *Sputtering Materials for VLSI and Thin Film Devices* (ed Sarkar, J.) 93–170 (William Andrew Publishing, Boston, 2014). ISBN: 978-0-8155-1593-7.

56. Fillon, B. in *Micromanufacturing Engineering and Technology (Second Edition)* (ed Qin, Y.) 2nd Edition, 393–424 (William Andrew Publishing, Boston, 2015). ISBN: 978-0-323-31149-6.

57. Pfau, A., Aydin, O., Dragon, A. & Willenbacher, N. *Beschichtung bei hohen Geschwindigkeiten – Optimierung von Auftrags – und Klebstoff – Systemen* in *Tagungsband 28. Münchener Klebstoff- und Veredelungssymposium* (2003).

58. Maenosono, S., Okubo, T. & Yamaguchi, Y. Overview of nanoparticle array formation by wet coating. *Journal of Nanoparticle Research* **5,** 5–15 (2003).

59. Vaško, K. *Schichtsysteme für Verpackungsfolien mit hohen Barriereeigenschaften* PhD thesis (Technische Universität München, 2006).

60. Cheng, I.-C. & Wagner, S. in *Flexible Electronics: Materials and Applications* (eds Wong, W. S. & Salleo, A.) 1–28 (Springer, New York, 2009).

61. Choi, B. I., Nham, H. S., Woo, S. B. & Kim, J. C. Ultralow Water Vapor Permeation Measurement Using Tritium for OLED Displays. *Journal of the Korean Physical Society* **53,** 2179–2184 (2008).

62. Amberg-Schwab, S. in *Handbook of Sol-Gel Science and Technology - Volume III: Applications of Sol-Gel Technology* (ed Sakka, S.) 455–478 (Kluwer, Dordrecht, 2005).

63. Affinito, J. & Hilliard, D. *A New Class of Ultra-Barrier Materials* in *47th Annual Technical Conference Proceedings* (Society of Vacuum Coaters, 2004), 563–593.

64. Graff, G. L., Williford, R. E. & Burrows, P. E. Mechanisms of vapor permeation through multilayer barrier films: Lag time versus equilibrium permeation. *Journal of Applied Physics* **96,** 1840–1849 (2004).

65. Amberg-Schwab, S., Hoffmann, M., Bader, H. & Gessler, M. Inorganic-organic polymers with barrier properties for water vapor, oxygen and flavors. *Journal of Sol-gel Science and Technology* **13,** 141–146 (1998).

66. Haas, K.-H., Amberg-Schwab, S., Rose, K. & Schottner, G. Functionalized coatings based on inorganic–organic polymers (ORMOCER®s) and their combination with vapor deposited inorganic thin films. *Surface and Coatings Technology* **111,** 72–79. ISSN: 0257-8972 (1999).

67. Hanika, M., Langowski, H.-C. & Peukert, W. *Simulation and Verification of Defect-Dominated Permeation Mechanisms in Multiple Structures of Inorganic and Polymeric Barrier Layers* in *46th Annual Technical Conference Proceedings* (Society of Vacuum Coaters, 2003), 592–599.

68. Schmidt, M. M. *High barrier materials for flexible and transparent encapsulation of organic electronics* PhD thesis (Technische Universität München, 2013).

69. Nentwig, J. *Kunststoff-Folien: Herstellung - Eigenschaften - Anwendung* ISBN: 3446403906 (Carl Hanser Verlag GmbH & Co. KG, München, 2006).

70. Vogt, B. D. *et al.* X-ray and neutron reflectivity measurements of moisture transport through model multilayered barrier films for flexible displays. *Journal of Applied Physics* **97,** 114509–1–114509–7 (2005).

71. Seo, S.-W., Jung, E., Lim, C., Chae, H. & Cho, S. M. Water permeation through organic-inorganic multilayer thin films. English. *Thin Solid Films* **520,** 6690–6694 (2012).

72. Paetzold, R. *et al. High-sensitivity permeation measurements on flexible OLED substrates* in *Organic Light-Emitting Materials and Devices VII* **5214** (2004), 73–82.

73. Nisato, G. *et al.* Experimental comparison of high-performance water vapor permeation measurement methods. *Organic Electronics* **15,** 3746–3755 (2014).

74. Meyer, J. *et al.* Al2O3/ZrO2 Nanolaminates as Ultrahigh Gas-Diffusion Barriers—A Strategy for Reliable Encapsulation of Organic Electronics. *Advanced materials* **21,** 1845–1849 (2009).

75. Kim, N. *Fabrication and characterization of thin-film encapsulation for organic electronics* PhD thesis (Georgia Institute of Technology, 2009).

76. Park, M.-H. *et al.* Flexible organic light-emitting diodes for solid-state lighting. *Journal of Photonics for Energy* **5,** 1 –21 (2015).

77. Duggal, A. R. *Plastic substrates with improved barrier properties for devices sensitive to water and/or oxygen, such as organic electroluminescent devices* US Patent 6,465,953. 2002.

78. Ramadas, S. K. & Shwe, Z. M. *Inorganic graded barrier film and methods for their manufacture* US Patent App. 12/990,485. 2011.

79. Amberg-Schwab, S, Noller, K., Weber, U & Miesbauer, O. *Hochbarrieren-verbunde und Verfahren zu ihrer Herstellung* Patent WO2010069958-A1. 2010.

80. Comyn, J. in *Polymer permeability* (ed Comyn, J.) 1–10 (Chapman & Hall, 1985). ISBN: 978-94-010-8650-9.

81. Koros, W. J. in *Barrier Polymers and Structures* (ed Koros, W. J.) *ACS Symposium Series* 423, 1–21 (American Chemical Society, Washington, 1990).

82. Graham, T. On the Absorption and Dialytic Separation of Gases by Colloid Septa. *The London, Edinburgh, and Dublin Philosophical Magazine and Journal of Science* **32,** 401–420 (1866).

83. Stannett, V. The transport of gases in synthetic polymeric membranes – an historic perspective. *Journal of Membrane Science* **3,** 97 –115. ISSN: 0376-7388 (1978).

84. Menges, G., Haberstroh, E., Michaeli, W. & Schmachtenberg, E. *Menges Werkstoffkunde Kunststoffe* 6. Aufl., XVI, 455 S. ISBN: 978-3-446-42762-4 (Carl Hanser Verlag GmbH Co KG, München, 2011).

85. Atkins, P. W. & de Paula, J. *Physikalische Chemie* 5th ed. (Wiley-VCH, Weinheim, 2013).

86. Vieth, W. R. Diffusion in and through polymers: Principles and applications. *American Scientist; (United States)* **81** (1991).

87. Demtröder, W. *Experimentalphysik 1: Mechanik und Wärme* Dritte Auflage (Springer, Berlin, 2004).

88. Fließbach, T. *Statistische Physik: Lehrbuch zur Theoretischen Physik IV* Vierte Auflage (Elsevier Spektrum Akademischer Verlag, München, 2007).

89. Crank, J. *The Mathematics of Diffusion* (Oxford University Press, London, 1975).

90. Rogers, C. in *Polymer permeability* (ed Comyn, J.) 11–73 (Chapman & Hall, 1985). ISBN: 978-94-010-8650-9.

91. Brauer, H. & Mewes, D. *Stoffaustausch einschliesslich chemischer Reaktionen* (Sauerländer, Aarau and Frankfurt a.M., Aarau and Frankfurt a.M., 1971).

92. Stern, S. A. & Trohalaki, S. in *Barrier Polymers and Structures* (ed Koros, W. J.) *ACS Symposium Series* 423, 22–59 (American Chemical Society, Washington, 1990).

93. Langowski, H.-C. Stofftransport durch polymere und anorganische Schichten. *Vakuum in Forschung und Praxis* **17,** 6–13 (2005).

94. Mortimer, C. E., Müller, U. & Beck, J. *Chemie: Das Basiswissen der Chemie* 11th ed. (Thieme, Stuttgart, 2014).

95. Hanika, M. *Zur Permeation durch aluminiumbedampfte Polypropylen- und Polyethylenterephtalatfolien* PhD thesis (Technische Universität München, 2004).

96. Mercea, P. in *Plastic Packaging - Interactions with Food and Pharmaceuticals* (eds Piringer, O. G. & Baner, A. L.) 2nd edition, 123–162 (Wiley-VCH, Weinheim, 2008).

97. Prins, W & Hermans, J. J. Theory of permeation through metal coated polymer films. *The journal of physical chemistry* **63,** 716–720 (1959).

98. Beu, T. & Mercea, P.-V. Gas transport through metallized polymer membranes. *Materials chemistry and physics* **26,** 309–322 (1990).

99. Decker, W. & Henry, B. *Basic Principles of Thin Film Barrier Coatings* in *45th Annual Technical Conference Proceedings* (Society of Vacuum Coaters, 2002), 492–502.

100. Tropsha, Y. G. & Harvey, N. G. Activated Rate Theory Treatment of Oxygen and Water Transport through Silicon Oxide/Poly(ethylene terephthalate) Composite Barrier Structures. *The Journal of Physical Chemistry B* **101,** 2259–2266 (1997).

101. Henry, B. M. *et al. The Permeation of Water Vapor Through Gas Barrier Films* in *44th Annual Technical Conference Proceedings* (Society of Vacuum Coaters, 2001), 469–475.

102. Henry, B. M. *et al. Gas Permeation Studies of Metal Oxide/Polymer Composite Films* in *45th Annual Technical Conference Proceedings* (Society of Vacuum Coaters, 2002), 514–518.

103. Garnier, G. *et al.* Interest and durability of multilayers: from model films to complex films. *Polymers for Advanced Technologies* **22,** 847–856 (2011).

104. Miesbauer, O., Schmidt, M. & Langowski, H.-C. Stofftransport durch Schichtsysteme aus Polymeren und dünnen anorganischen Schichten. *Vakuum in Forschung und Praxis* **20,** 32–40 (2008).

105. Utz, H. *Barriereeigenschaften aluminiumbedampfter Kunststoffolien* PhD thesis (Technische Universität München, 1995).

106. Jamieson, E. & Windle, A. Structure and oxygen-barrier properties of metallized polymer film. *Journal of Materials Science* **18,** 64–80 (1983).

107. Erlat, A. *et al.* Characterisation of aluminium oxynitride gas barrier films. *Thin Solid Films* **388,** 78 –86. ISSN: 0040-6090 (2001).

108. Singh, B *et al.* Ultra-thin hybrid organic/inorganic gas barrier coatings on polymers. *Surface and Coatings Technology* **201,** 7107–7114 (2007).

109. Perrotta, A. *et al.* The impact of the nano-pore filling on the performance of organosilicon-based moisture barriers. *Thin Solid Films* **595,** 251–257 (2015).

110. Czeremuszkin, G., Latreche, M. & Wertheimer, M. R. *Transparent support for organic light emitting device* US Patent 7,298,072. 2007.

111. Van Amerongen, G. Influence of structure of elastomers on their permeability to gases. *Journal of polymer science* **5,** 307–332 (1950).

112. Arrhenius, S. Über die Reaktionsgeschwindigkeit bei der Inversion von Rohrzucker durch Säuren. *Zeitschrift für physikalische Chemie* **4.1,** 226–248 (1889).

113. Dushman, S. & Langmuir, I. The diffusion coefficient in solids and its temperature coefficient. *Phys. Rev.* **20** (1922).

114. Pauly, S. in *Polymer handbook* (eds Brandrup, J., Immergut, E. H., Grulke, E. A., Abe, A. & Bloch, D. R.) 4th ed., VI/543–VI/569 (Wiley New York, 1999).

115. Barrer, R. M. *Diffusion in and through solids* ISBN: 5883795331 (Cambridge University Press, Cambridge, England, 1941).

116. Henry, B. M. *et al.* A microstructural study of transparent metal oxide gas barrier films. *Thin Solid Films* **355,** 500–505 (1999).

117. Howells, D. G., Henry, B. M., Madocks, J. & Assender, H. E. High quality plasma enhanced chemical vapour deposited silicon oxide gas barrier coatings on polyester films. *Thin Solid Films* **516,** 3081–3088 (2008).

118. Henry, B. *et al. Permeation studies of transparent barrier coatings.* in *Society of Vacuum Coaters 46th Annual Technical Conference* (2003), 600–605.

119. Carslaw, H. S. & Jaeger, J. C. *Conduction of Heat in Solids* Zweite Auflage (Oxford University Press, London, 1959).

120. Hickson, R. I., Barry, S. I. & Mercer, G. N. Critical times in multilayer diffusion. Part 1: Exact solutions. English. *International Journal of Heat and Mass Transfer* **52,** 5776–5783 (2009).

121. Ogata, Y., Sakka, T. & Iwasaki, M. Diffusion through a multilayered phase in electrochemical systems: an approach by numerical inversion of the Laplace transform. *Journal of Applied Electrochemistry* **25,** 41–47 (1995).

122. Hickson, R. *Critical times of heat and mass transport through multiple layers* PhD thesis (University of New South Wales, 2010).

123. Vodička, V. Eindimensionale Wärmeleitung in geschichteten Körpern. *Mathematische Nachrichten* **14,** 47–55 (1955).

124. Wirth, P. E. & Rodin, E. Y. A Unified Theory of Linear Diffusion in Laminated Media. *Advances in Heat Transfer* **15,** 283–330 (1982).

125. Zajec, B. Hydrogen permeation barrier - Recognition of defective barrier film from transient permeation rate. *International Journal of Hydrogen Energy* **36,** 7353–7361 (2011).

126. De Monte, F. Transient heat conduction in one-dimensional composite slab. A 'natural' analytic approach. *International Journal of Heat and Mass Transfer* **43,** 3607–3619 (2000).

127. De Monte, F. An analytic approach to the unsteady heat conduction processes in one-dimensional composite media. *International Journal of Heat and Mass Transfer* **45,** 1333–1343 (2002).

128. Kiese, S., Kücükpinar, E., Miesbauer, O. & Langowski, H.-C. Time-dependent water vapor permeation through multilayer barrier films: Empirical versus theoretical results. *Thin Solid Films* **672,** 199–205 (2019).

129. ASTM F3299-18. *Standard Test Method for Water Vapor Transmission Rate Through Plastic Film and Sheeting Using an Electrolytic Detection Sensor (Coulometric P2O5 Sensor)* ASTM International, West Conshohocken, PA, 2018.

130. MOCON, Inc. *AQUATRAN 3 WVTR Analyzer* 2020. `https://www.ametekmocon.com/products/permeationanalyzers/wvtr-permeation-analyzers/aquatran-3`.

131. Roos, A. *Water Vapour Permeation Testing of Ultra-Barriers: Limitations of Current Methods and Advancements Resulting in Increased Sensitivity* 2013. `http://www.vacuum-uk.org/pdfs/vs4/wvtr.pdf`.

132. Kumar, R. S., Auch, M., Ou, E., Ewald, G. & Jin, C. S. Low moisture permeation measurement through polymer substrates for organic light emitting devices. *Thin Solid Films* **417,** 120–126. ISSN: 0040-6090 (2002).

133. Paetzold, R., Winnacker, A., Henseler, D., Cesari, V. & Heuser, K. Permeation rate measurements by electrical analysis of calcium corrosion. *Review of Scientific Instruments* **74,** 5147. ISSN: 00346748 (2003).

134. Reese, M. O., Dameron, A. A. & Kempe, M. D. Quantitative calcium resistivity based method for accurate and scalable water vapor transmission rate measurement. *Review of Scientific Instruments* **82,** 085101 (2011).

135. Beese, H., Grählert, W. & Kaskel, S. *pat.* DE102012010269B3 (2013).

136. Fraunhofer IWS. *HiBarSens: Ultrabarriereeigenschaften sind endlich messbar: Infoblatt* 2018. `http://www.hibarsens.com/wa_files/2402_20Datenblatt_20HiBarSens_20280218.pdf`.

137. Choi, B. I., Woo, S. B., Kim, J. C., Kim, S. H. & Seo, S. J. Determining Ultra-low Moisture Permeation Measurement for Sealants on OLED Encapsulation. *Journal of the Korean Physical Society* **61,** 2032–2035 (2012).

138. Bujas, R. S. & Dunkel, R. *pat.* US 2004/0083796 A1 (2004).

139. Bujas, R. S. & Dunkel, R. *pat.* US 7,178,384 B2 (20.02.2007).

140. Brewer, P. J., Goody, B. A., Woods, P. T. & Milton, M. J. T. A dynamic gravimetric standard for trace water. *Review of Scientific Instruments* **82,** 105102. ISSN: 00346748 (2011).

141. Brewer, P. J., Goody, B. A., Kumar, Y. & Milton, M. J. T. Accurate measurements of water vapor transmission through high-performance barrier layers. *Review of Scientific Instruments* **83.** ISSN: 00346748 (2012).

142. Nakano, Y., Yanase, T., Nagahama, T., Yoshida, H. & Shimada, T. Accurate and stable equal-pressure measurements of water vapor transmission rate reaching the 10- 6 gm- 2 day- 1 range. *Scientific reports* **6,** 35408 (2016).

143. Simmler, H. *et al. Vacuum Insulation Panels - Study on VIP-components and panels for service life prediction of VIP in building applications (Subtask A)* tech. rep. (HiPTI-High Performance Thermal Insulation, IEA/ECBCS Annex 39, 2005).

144. Franz, R. Permeation of volatile organic compounds across polymer films—Part I: Development of a sensitive test method suitable for high-barrier packaging films at very low permeant vapour pressures. *Packaging Technology and Science* **6,** 91–102. ISSN: 08943214 (1993).

145. Kiese, S. *et al.* A systematic approach for the accurate and rapid measurement of water vapor transmission through ultra-high barrier films. *Review of Scientific Instruments* **88,** 025108 (2017).

146. Fahlteich, J. *et al.* Roll-to-roll thin film coating on fluoropolymer webs: Status, challenges and applications. *Surface and Coatings Technology* **314.** Selected papers from the Society of Vacuum Coaters 59th Annual Technical Conference, 160–168. ISSN: 0257-8972 (2017).

147. Henry, B. M. *et al. The Permeation of Water Vapor Through Gas Barrier Films* in *44th Annual Technical Conference Proceedings* (Society of Vacuum Coaters, 2001), 469–475.

148. Tobin, V. R., Suttle, H. & Assender, H. E. Nanodefect-controlled permeation in AlO_x/polymer gas barrier films. *Thin Solid Films* **642,** 142–150. ISSN: 0040-6090 (2017).

149. Bieder, A., Gruniger, A. & von Rohr, R. Deposition of SiO_x diffusion barriers on flexible packaging materials by PECVD. *Surface and Coatings Technology* **200,** 928–931. ISSN: 0257-8972 (2005).